INVESTIGATIONS OF THE PREFERRED MODES OF NORTH PACIFIC JET VARIABILITY, THEIR DOWNSTREAM IMPACTS, AND TROPICAL AND EXTRATROPICAL PRECURSORS

By

Kyle S. Griffin

A dissertation submitted in partial fulfillment of

the requirements for the degree of

Doctor of Philosophy

(Atmospheric and Oceanic Sciences)

at the

UNIVERSITY OF WISCONSIN-MADISON

2016

Date of final oral examination: 5/9/2016

The dissertation is approved by the following members of the Final Oral Committee:
Jonathan E. Martin, Professor, Atmospheric and Oceanic Sciences
Matthew H. Hitchman, Professor, Atmospheric and Oceanic Sciences
Michael C. Morgan, Professor, Atmospheric and Oceanic Sciences
Daniel J. Vimont, Associate Professor, Atmospheric and Oceanic Sciences
Samuel N. Stechmann, Associate Professor, Mathematics

Acknowledgments

After many years as a graduate student, I can't readily begin to sufficiently acknowledge the full collection of people who have helped me accomplish this goal. I've been fortunate to have the opportunities to pursue many of my curiosities since I was a young child. I've been privileged to experience a number of the instructors I had in high school, who fostered my curiosity throughout what was, in retrospect, an important time in my intellectual development. Whether it was building rockets or participating in science competitions, there are many friends and instructors who provided a foundation both inside the classroom and beyond it. I'd like to especially thank John Dietrich, who was one of my first sources of cynicism – scientific and otherwise.

During high school, and into my undergraduate years, I was given an incredible opportunity to work with and eventually in the NWS's Hydrometeorological Prediction Center (HPC; now WPC), where I gained significant experience with the day-to-day considerations of operational meteorology. This was only possible because of the connections of another of my high school teachers, Jill Culver, who was able to introduce me to Mike Eckert, and, subsequently, Todd Kimberlain and David Roth. These meteorologists were able to begin satiating my meteorological curiosities before I ever stepped through the doors of a university. There are few true substitutions for getting knee-deep in analyses and forecasts consistently for several summers and winters, and the knowledge and perspective I have gained continue to prove invaluable. I sincerely thank everyone at HPC who allowed me to not only work among them, but also earn their respect and become a member of their team as well as one of their friends.

My five years at the University at Albany provided numerous opportunities for me to grow within the meteorology community. While the coursework and resources provided to students were borderline spoiling me, the support of the faculty was memorable throughout both my undergraduate and Masters degrees. Nearly every faculty or staff member was always willing to have a casual conversation with me, whether relevant to work or completely off the wall. I especially appreciate the conversations I had with Ryan Torn, who pushed me toward a more analytical perspective of the science, Paul Roundy, who helped initiate and continues to motivate much of my interest in intraseasonal variability, amongst other things, as well as Dan Keyser, whose meticulous insight ensured my work did not jump the tracks while also improving how I approached scientific writing. I would also be amiss without thanking Kevin Tyle, who was instrumental in allowing me the computational free reigns to play, experiment, and create so many of the projects I enjoyed (and continue to enjoy) the most.

The students at Albany also provided immeasurable camaraderie, especially during my graduate studies, with numerous outings and events that ensured I did not fully disappear into my research. While I could certainly write another dissertation about some of the fondest memories, I'd just like to especially thank Derek Mallia, Alan Brammer, Diana Thomas, Mike Ventrice, Carl Schreck, Alicia Bentley, and Philippe Papin for what they've afforded me both scientifically and personally. Numerous other graduate students also made this time valuable, especially other students who worked with me under Lance, and I thank you all.

I must also express my deep appreciation for Lance Bosart. Lance guided me throughout both of my degrees, providing a cornucopia of fascinating research ideas and helped shape my ability to fashion a story out of seemingly disparate events. Despite the fact that I only took “notes” using crayons in his senior-level synoptic course, Lance appreciated and helped grow much of my synoptic intuition throughout the three years or so that I worked with him. Our “pun”ishment of each other and those around us also helped me develop a wit that is likely too quick for my own good when it comes to a sense of humour, but has certainly helped me think on my feet. Lastly, Lance provided innumerable opportunities to travel to conferences both near and afar, where the goal was always to interact with others in the field and gain that familiarity. In fact, on one of the earliest trips Lance sent me on, I was able to meet my wife, Sarah, for whom I am incredibly thankful for as well. More broadly because of these opportunities, I can say that I have been able to connect with far more colleagues than I ever would have expected, opening numerous doors for even further opportunities along the way.

In fact, one such opportunity at the Cyclone Workshop made my graduate career at Wisconsin possible, as I was able to connect with Jonathan Martin. Jon was willing to take on the scraggly-haired kid who simply walked up and asked him if there was any chance he had funding for a new graduate student to start over a year after that point. Jon was also understanding when he discovered that there was a lady furthering my interest in joining his Madison research group. Seventeen months later, Jon welcomed me in his office as I completed my move to Madison, where he was gracious enough to let me spend much of my first semester finishing my Masters thesis from Albany while spinning up in his group. Since then, Jon has provided me wonderful opportunities to pursue our ideas (even if some end up a bit crazy) during my nearly four years with him. I have been able to try my hand at teaching, at coding, and certainly at writing, where Jon has unquestionably provided me with the best coaching I could have ever wanted. He has helped ensure that I remain focused when necessary and that I afford curiosity when useful, and instilled confidence in myself and confidence in what I do. It is these refinements that have put some striking finishing touches on the scientist I feel I have become, and for that, I have a dearth of words.

Of course, I must also state my appreciation for the other faculty in the AOS department – the breadth of the atmospheric sciences that is covered by this faculty is to be commended, as it has broadened my horizons to parts of the field I likely would not have known or appreciated otherwise. I must first thank Michael Morgan for his constant onslaught of theoretical mind games, culinary inquisitions, and chalkboard art, and I believe something can be worked out to allow for visits with the bobbleheads. Michael also provided a key voice in many scientific discussions throughout the two years we have overlapped, complimenting his familiar synoptic intuition with a perspective that also emphasized rigorous numerical analysis – a perspective I have slowly begun to develop myself and for which I am grateful. Dan Vimont also provided me with a firm footing in the quicksand of applied statistics, one that has helped me get my own feet underneath me. I'd also like to thank Matt Hitchman, who always appreciated my synoptic sense, for enlightening conversations, and Sam Stechmann, for providing insight into a marriage of mathematics and tropical meteorology that I hope to be able to pursue further in the future.

The graduate students of AOS have been a phenomenal group to be around throughout these past four years. I undoubtedly appreciate each and every person who helped motivate us to attend all the Pizza Hut buffets and trips to the Big Ten. I must particularly emphasize the incredible students and friends that have rotated through the Martin group during this time. Specifically, Andrew Winters, Croix Christenson, Zak Handlos, and Melissa Breeden have provided me with close friendship since the first day I met them, with countless evenings of debauchery around Madison. I've also thoroughly grown through the science we discuss and I can't wait to see how each of careers plays out. I feel that I'm grasping at so few words to say so many things, and I obviously cannot thank you all enough.

I must also recognize a number of friends from around Madison (and, by now, even beyond Madison) who have helped me maintain a life away from work as well, throughout evenings at Concert on the Square, ultimate games, trivia, and plenty of beer brewing related things. You have all helped me maintain what little semblance of sanity I may have left and allowed me to express my creative side in ways we have all thoroughly enjoyed.

The family that I have has always been an incredibly close one. Despite my role as the child who leaves home too young to go to school and seems to keep moving farther away with time, you have done an incredible job of showing your love, encouragement, and support throughout these last nine years away from home. I know I could never visit enough for your liking, but technology helps the gap grow smaller. So, to my Mom, Dad, sister Sarah, and Grandma, I want to ensure you know that your support has been immeasurably important throughout this process. And yes Dad, the daily emails are always appreciated no matter what.

I must last attempt to do the impossible, which is to express my gratitude to my wife, Sarah. Even after we have known each other for nearly six years, our relationship continues to grow by the day – although perhaps a little less during my long nights of dissertation writing. Her all-but-physically kicking me out the door is certainly one of the most significant reasons I am finishing this document in May and not…well, much later. Her understanding of me is far deeper than I can fathom and for that I can only be thankful. As long as you are around, I am glad I will have a friend who shares so many of the same interests and desires, whether it be the traveling or the soccer, or often enough both. The love of all of these things is so much more than I could have asked for, and your continued support of me continues to leave me without words. I hope we spend many more years moving forward with our ever-growing life together.

Table of Contents

ACKNOWLEDGMENTS II
TABLE OF CONTENTS VIII
LIST OF FIGURE CAPTIONS X
ABSTRACT XVII

1. INTRODUCTION 1

1.1 THE JET STREAM 1
1.2 TROPICAL CONVECTION 4
1.3 TROPICAL-EXTRATROPICAL INTERACTION 6

2. DATA AND METHODOLOGY 13

2.1 EOF TECHNIQUES 13
2.2 COMPOSITE ANALYSES 17

3. SYNOPTIC FEATURES ASSOCIATED WITH TEMPORALLY COHERENT MODES OF VARIABILITY OF THE NORTH PACIFIC JET STREAM 20

3.1. OVERVIEW 20
3.2. PREFERRED MODES OF VARIABILITY 21
3.3. COMPOSITE ANALYSIS 22
3.3.1. EXTENSION (POSITIVE TE-EOF 1) 23
3.3.2. RETRACTION (NEGATIVE TE-EOF 1) 25
3.3.3. POLEWARD SHIFT (POSITIVE TE-EOF 2) 27
3.3.4. EQUATORWARD SHIFT (NEGATIVE TE-EOF 2) 29
3.4. TROPICAL CONVECTION COMPOSITES 31
3.5. DISCUSSION 33

4. ISENTROPIC PRESSURE DEPTH AS A TOOL FOR ANALYZING TROPICAL-EXTRATROPICAL INTERACTIONS 48

4.1. OVERVIEW 48
4.2. METHODOLOGY 49
4.3. APPLICATIONS OF ISENTROPIC PRESSURE DEPTH 53
4.4. CLIMATOLOGICAL ASPECTS OF ISENTROPIC PRESSURE DEPTHS 55
4.5. CASE STUDY - MARCH 2012 58
4.5.1. INTERACTION BETWEEN TROPICAL CONVECTION AND THE EAST ASIAN JET STREAM 59
4.5.2. TRANSITION FROM TROPICALLY-DRIVEN TO EXTRATROPICALLY-DRIVEN EVOLUTION 61
4.5.3. DEVELOPMENT OF A PRESSURE DEPTH ANOMALY FROM FRONTAL CONVECTION 62
4.6. SUMMARY AND DISCUSSION 65

5. ISENTROPIC PRESSURE DEPTH PRECURSORS TO PREFERRED MODES OF VARIABILITY OF THE NORTH PACIFIC JET STREAM 86

5.1. COMPOSITE ANALYSES OF EXTENDED JET CASES 87

5.2 COMPOSITE ANALYSES OF RETRACTED JET CASES **90**
5.3 COMPOSITE ANALYSES OF POLEWARD SHIFTED JET CASES **93**
5.4 COMPOSITE ANALYSES OF EQUATORWARD SHIFTED JETS **96**
5.5. SUMMARY AND DISCUSSION **98**

6. SUMMARY, DISCUSSION, AND FUTURE WORK **113**

6.1 SUMMARY **114**
6.2. CORRELATIONS BETWEEN TE-EOFS AND THE PNA **117**
6.3. DISCUSSION OF ISENTROPIC PRESSURE DEPTHS **118**
6.3.1. THE TRANSITION FROM TROPICALLY- TO EXTRATROPICALLY-DRIVEN FLOW 118
6.3.2. SOURCES OF POSITIVE PRESSURE DEPTH ANOMALIES OVER THE MID-LATITUDES OF ASIA 120
6.4. POTENTIAL FORECAST APPLICATIONS OF DOWNSTREAM IMPACTS OF TE-EOF MODES **121**

7. REFERENCES **124**

List of figure captions

Chapter 1

Figure 1.1. Composite anomaly map of the 700 mb height anomalies over five cold eastern United States winters, specifically 1960-61, 1962-63, 1967-68, 1969-70, and 1976-77. From Wallace and Gutzler (1981; their Fig. 5a).

Chapter 2

Figure 2.1. Comparison of a traditional PC, a traditional PC with a 10-day smoother, and a TE-PC for the NDJFM 2009-2010 season for the leading mode (top) and second leading mode (bottom) of variability. PCs correspond to EOFs of 250 hPa zonal wind speed over the North Pacific.

Chapter 3

Figure 3.1. TE-EOF 1 (extension/retraction) of the 250 hPa zonal wind over the North Pacific. EOF regressed back onto anomaly data is shaded (m s^{-1}; per color bar). Climatological zonal wind is contoured in black starting at 20 m s^{-1}. Top panel (D-5d) represents the TE-EOF pattern at the beginning of the 10-day TE window; middle panel (D0) represents the pattern halfway through the TE window; bottom panel (D+5d) represents the pattern at the end of the TE window.

Figure 3.2. As in Fig. 3.1 but for TE-EOF 2 (meridional shift) of the 250 hPa zonal wind over the North Pacific.

Figure 3.3. Composite of cases where PC of TE-EOF 1 was positive and was greater than 1.5 standard deviations, representing jet extension cases. D0 is defined as the midpoint of the 10-day window, where D-5d (D+5d) is the beginning (end) point. Left plots (a-e) show anomalies of 250 hPa zonal wind (shaded per color bar; only where statistically significant

at 95% level) and heights (dashed every 50 m). Right plots (f-j) include anomalies of 850 hPa temperature (shaded per color bar; only where statistically significant at 95% level) and heights (dashed every 20 m). Height anomalies in all plots are only significant within regional identified by stippling. All plots show the climatological zonal wind in black contours starting at 30 m s^{-1}. Composite sample size = 40.

Figure 3.4. As in Fig. 3.3 for cases where the PC of TE-EOF 1 was less than -1.5 standard deviations, representing jet retraction cases. Composite sample size = 40.

Figure 3.5. As in Fig. 3.3 for cases where the PC of TE-EOF 2 was greater than 1.5 standard deviations, representing poleward shift cases. Composite sample size = 36.

Figure 3.6. As in Fig. 3.3 for cases where the PC of TE-EOF 2 was less than -1.5 standard deviations, representing equatorward shift cases. Composite sample size = 45. Unlike the previous composites, D+10d did not contain anomalies that were both physically meaningful and statistically significant.

Figure 3.7. Composites of OLR (shaded, per color bar) calculated as in Fig. 3.3 and Fig. 3.4 for jet extension (a, c, e) and jet retraction cases (b, d, f), respectively, from TE-EOF 1. Numbers of cases are consistent with the respective previous composites.

Figure 3.8. As in Fig. 3.7 for poleward shift (from Fig. 3.5; a, c, e) and equatorward shift (Fig. 3.6; b, d, f) jet cases from TE-EOF 2. Numbers of cases are consistent with the respective previous composites.

Chapter 4

Figure 4.1. Vertical schematics of isentropic pressure depth. Black lines represent isentropes and orange shading represents isotachs. Red line in (a) indicates the pressure

depth *p* of an isentropic layer. That layer is inflated by the upward mass flux by deep convection in (b), increasing the isentropic pressure depth to *p+Δp*.

Figure 4.2. Pressure depth (a) and reciprocal of potential vorticity (RPV; b) in the 340-355 K isentropic layer, shaded and contoured per the color bar, for 0000 UTC 22 October 2013. Red "T" indicates the location of an upper level trough, while the blue "TC" indicates the position of TC Raymond.

Figure 4.3. Schematic demonstration of the calculation of a negative standard departure value. (a) Distribution of isentropic pressure depth anomalies for a single grid point at a single time across all 32 years of CFSR data. (b) Select only the negative anomaly values from that distribution. (c) Taking the negative of the values remaining in the distribution and include in a new distribution. The negative standard departure is then the standard deviation of this newly constructed symmetric distribution.

Figure 4.4. Horizontal schematics of isentropic pressure depth. Green lines represent isopleths of isentropic pressure depth within a given isentropic layer and orange shading represents isotachs. An increase in isentropic pressure depth from ~2p' (a) to ~3p' (b) can tighten the isentropic pressure depth gradient (light blue arrows) and locally increase the vertical geostrophic wind shear (dark blue arrows) and mean wind speed in that isentropic layer.

Figure 4.5. Mean 1000 hPa equivalent potential temperature for (a) January and (c) July. Bottom isentropic layer of the thickest 5 K isentropic layer in the climatology of pressure depths for (b) January and (d) July, such that a value of 340 K signifies that the 340-345 K isentropic layer is thicker than any other isentropic layer in that monthly mean.

Figure 4.6. Mean January isentropic pressure depths for (a) 315-330 K and (b) 340-355 K layers. Mean January (c) positive and (d) negative standard departures of isentropic pressure depths in the 315-330 K layer. The purple line in (a) and (b) represent the mean 120 hPa isentropic pressure depth isopleth. The 120 hPa isopleth from (a) is reproduced for reference in (c) and (d). Shading per the respective color bars.

Figure 4.7. Mean January positive (a) and negative (b) standard departures of isentropic pressure depth (shading) in the 315-330 K isentropic layer. Purple line represents the mean January 120 hPa pressure depth isopleth in the 315-330 K layer. Composite zonal wind (black contours) associated with events where isentropic pressure depth exceeds (a) +1.5 standard departures at 42.5°N, 167.5°W (blue H) and (b) -1.0 standard departure at 37.5°N and 137.5°W (red L). Thick black contours are representative isentropic pressure depth anomalies, with the (a) blue and (b) red arrows indicating the direction of the vertical geostrophic wind shear associated with each representative anomaly. The dashed purple line indicates where the solid purple line (120 hPa isopleths) might shift in response to the imposition of the representative anomalies.

Figure 4.8. OLR anomalies (shaded, W m-2) and OLR filtered for MJO in wavenumber-frequency space (per Kiladis 2009) in contours (dashed where negative, signifying active MJO convection; every 5 W m-2, excluding the zero contour).

Figure 4.9. 340-355 K layer mean wind speed (contoured every 10 m s^{-1} starting at 30 m s^{-1}) and pressure depth anomalies (shaded per color bar; every 15 hPa) for (a) 0000 UTC 3 March 2012, (b) 1200 UTC 5 March, (c) 0000 UTC 8 March, and (d) 1200 UTC 10 March.

Figure 4.10. Backward trajectories initialized at 1200 UTC 10 March and run backward 7 days (dots at 0000 UTC each day) from NOAA HYSPLIT. Black circles encompass nearly all

trajectory locations at the labeled times. Orange box indicates the approximate envelope of the MJO event between 3 March and 8 March, consistent with data in Fig. 4.8. Time series of altitude and potential temperature are also plotted along path of trajectories in inset.

Figure 4.11. As in Fig. 4.9 for 0000 UTC 12 March in (a) 315-330 K (pressure depth anomalies contoured every 30 hPa) and (b) 340-355 K. Mean sea level pressure (black contours, every 4 hPa) plotted in each panel.

Figure 4.12. As in Fig. 4.9 in the 315-330 K layer at (a) 0000 UTC 16 March, (b) 1200 UTC 16 March, and (c) 1200 UTC 17 March. Infrared imagery at each time is underlain where brightness temperatures are colder than 270 K. Black line A-A' on (b) indicates location of cross section presented in Fig. 4.13.

Figure 4.13. Cross section along line as indicated in Fig. 4.12b. Plotted are potential vorticity (shaded), isotachs of wind speed perpendicular to the cross section (thick black contours; every 10 m s-1 starting at 30 m s-1), potential temperature (thin black lines as labeled, every 5 K) and equivalent potential temperature (red lines, every 5 K). Upward vertical motion is plotted every .25 hPa s-1.

Figure 4.14. 850 hPa heights (contours; m) and temperature anomalies (shading; ˚C) at (a) 0000 UTC 16 March 2012, (b) 0600 UTC 19 March, and (c) 1200 UTC 20 March.

Figure 4.15. 1000–300 hPa thickness (shading; m) and 500 hPa height (black contours, every 60 m) at (a) 0000 UTC 16 March, (b) 0600 UTC 19 March, and (c) 1200 UTC 20 March.

Figure 4.16. As in Fig. 4.9 for the 315-330 K layer at (a) 0600 UTC 19 March and (b) 1200 UTC 20 March.

Figure 4.17. Schematic of March 2012 case study. Events in the 340-355 K layer are colored in red while events in the 315-330 K layer are colored in blue. Numbers correspond with events as referenced in Section 4.6.

Chapter 5

Figure 5.1. Time lagged composite analyses based upon maxima above 1.5 standard deviations in the TE-PC time series associated with TE-EOF 1 from GM16 (for jet extension events). Composite zonal wind anomalies (shaded; m s-1) and isentropic pressure depth anomalies in the 315-330 K layer (contoured; red where positive, blue where negative; every 12 hPa, zero contour excluded) computed at 5 day steps from (a) 15 days prior to the TE-PC maximum through (f) 10 days after.

Figure 5.2. As in Fig. 5.1 (for jet extension events), but with isentropic pressure depth anomalies in the 340-355 K layer (contoured every 6 hPa, zero contour excluded).

Figure 5.3. As in Fig. 5.1, but with composites constructed around local minimum below -1.5 standard deviations in the TE-PC 1 time series (for jet retraction events).

Figure 5.4. As in Fig. 5.2, but with composites constructed around local minimum below -1.5 standard deviations in the TE-PC 1 time series (for jet retraction events).

Figure 5.5. As in Fig. 5.1, but with composites constructed around local maximum above 1.5 standard deviations in the TE-PC 2 time series (for poleward shifted jet exit region events).

Figure 5.6. As in Fig. 5.2, but with composites constructed around local maximum above 1.5 standard deviations in the TE-PC 2 time series (for poleward shifted jet exit region events).

Figure 5.7. As in Fig. 5.1, but with composites constructed around local minimum below -1.5 standard deviations in the TE-PC 2 time series (for equatorward shifted jet exit region events).

Figure 5.8. As in Fig. 5.2, but with composites constructed around local minimum below -1.5 standard deviations in the TE-PC 2 time series (for equatorward shifted jet exit region events).

Figure 5.9. Conceptual model of pressure depth anomalies (red and blue contours; in isentropic layers as labeled), the climatological jet stream (thick black arrow), and zonal wind anomalies (thick purple arrow) for (a) jet extension events and (b) jet retraction events.

Figure 5.10. Conceptual model of the poleward shifted jet events, with annotations as described for Fig. 5.9. Pressure depth anomalies are in the 315-330 K layer in panels (a) and (b), and in the 340-355 K layer in panels (c) and (d). Panels (a) and (c) represent the position of features at 5 days prior to peak poleward shift (D-5d), while panels (b) and (d) represent the time of maximum poleward shift (D0).

Chapter 6

Figure 6.1. Daily time-lagged correlation between the PNA and (a) TE-PC 1, PC 1, and a 10-day smoothed PC 1. (b) As in (a) for the second leading modes of each EOF analysis. The bold middle line represents the mean of the correlation calculated for each season 1980-2010. Thinner lines above and below the bold line represent the ±1 standard deviation of the seasonal correlations. Lines colored per the legend.

Abstract

Time extended EOF (TE-EOF) analysis is employed to examine the synoptic-scale evolution of the two leading modes of north Pacific jet stream variability, namely its zonal extension/retraction (TE-EOF 1) and the north/south shift of its exit region (TE-EOF 2). Composite analyses are constructed preceding and following peaks in the principal component associated with each of the two TE-EOFs, providing insight into the preferred evolutions of the north Pacific jet. Jet extension events are associated with an anomalous Gulf of Alaska cyclone, while jet retractions are associated with an anomalous ridge over the Aleutians. Similar but shifted upper level patterns are noted with the corresponding poleward/equatorward shifted jet phases, with the poleward (equatorward) shift of the jet exit region associated with anomalous low-level warmth (cold) over western North America.

Such composites also suggest connections between certain phases of these leading modes of jet variability and deep convection in the tropics, a connection that has been challenging to physically diagnose in previous studies. The *isentropic pressure depth* measures the mass contained within an isentropic layer in a given grid column, enabling the tracking of mass exhausted by deep convection. The gradient of isentropic pressure depth is directly associated with the vertical geostrophic wind shear in that layer and thus provides a means to track the influence of convective mass flux on the evolution of the jet stream. A case study focused on the extreme North American warm episode of March 2012 demonstrates how positive pressure depth anomalies from a strong MJO event impact the jet stream over eastern Asia and drive a portion of the mid-latitude response that leads to the flow amplification and subsequent downstream warmth. This study demonstrates one way by which isentropic pressure depth can diagnose the impacts of tropical deep convection on the mid-latitude circulation.

Using TE-EOFs, composites of isentropic pressure depth are constructed, to examine the evolution of pressure depth anomalies preceding each phase of the two leading modes of jet variability. In jet extension events, a large negative pressure depth anomaly in the 315-330 K isentropic layer and a positive pressure depth anomaly in the 340-355 K isentropic layer align north and south of the climatological jet exit region, respectively. A similar but opposite configuration is found in jet retraction events. During poleward shifted jet events, the configuration of pressure depth anomalies is comparable to that observed in jet extension events, but shifted poleward. Positive pressure depth anomalies in each set of events predominantly originate from either the Maritime Continent or East Asia and track along the climatological jet before impacting the exit region of the jet stream. Negative pressure depth anomalies have similar upstream origins before moving through the jet in a similar manner. These composite evolutions provide insight into the synoptic-scale evolutions that precede the preferred modes of jet variability, highlighting the influence of both mid-latitude weather systems and mass flux from tropical deep convection on North Pacific jet variability.

1. Introduction

1.1 The jet stream

Among the most ubiquitous structural characteristics of the Earth's atmosphere are the narrow, rapidly flowing currents of air located near the tropopause, known as jet streams or jets. These features were largely unknown before and during World War II despite their original identification by Wasaburo Ooishi over Japan in 1924 (Lewis 2003). By the end of the war, however, the existence of jet streams was well established, quickly drawing substantial research attention that led to the discovery of separate subtropical (e.g. Namias and Clapp 1949, Loewe and Radok 1950, Yeh 1950, Koteswaram 1953) and polar (e.g. Namias and Clapp 1944, Palmén 1951, Newton 1954) jets.

Namias and Clapp (1949) were among the first to identify a separate subtropical jet stream, describing its latitudinal variability on a seasonal timescale. The first comprehensive descriptions of North Pacific jet stream structure were provided by Mohri (1953). He emphasized that the jet sat between contrasting air masses and that what often appeared to be a single jet entity was, in fact, a hybrid of the separate subtropical and polar jets. Considerable attention has been directed toward understanding the influence of external processes on the evolution of the jet. For instance, deep tropical convection, organized on the synoptic-scale, can impact the jet either directly via upper-level divergent outflow or remotely through the amplification of a ridge that leads to downstream development (e.g. Kiladis and Weickmann 1992, Madden and Julian 1994, Higgins et al. 2000, Archambault et al. 2013).

The work of Dickson and Namias (1976) included analysis showing connections between the synoptic-scale flow patterns over the North Pacific, North America, and North

Atlantic. Subsequently, these findings led to the first identifications of the Pacific North American (PNA) pattern and other teleconnections by Wallace and Gutzler (1981), who defined these teleconnections patterns based on December, January, and February (DJF) data over 15 winter seasons. The PNA is defined by identifying regions where 500 hPa height anomalies have a correlation coefficient exceeding ±0.6. The primary regions of correlation are located along and just east of 180˚ longitude, over western Canada near 120˚W, and over the southeastern United States near 90˚W, and alternate in sign, as seen in Fig. 1.1. The alternating nature of these anomalies suggests that a broad wave-like pattern in the mid-latitudes may support these anomaly centers. An additional region of positive correlation near 20˚N (the southernmost limit of the analysis) east of 180˚ further suggests that the PNA is correlated with 500 hPa heights over the tropical central Pacific Ocean. Finding this and similar artifacts of tropical activity throughout their analysis, Wallace and Gutzler conclude by asking “Do the extratropical Northern Hemisphere patterns described in the paper extend into the tropics or even into the Southern Hemisphere extratropics?” This question may not yet be fully answered, but several studies have provided insight.

To date, the variability of the North Pacific jet and its resultant impacts on the regional and hemispheric flow have been less thoroughly investigated. Schubert and Park (1991) conducted one of the first examinations of the intraseasonal variability of the North Pacific jet by performing an empirical orthogonal function (EOF) analysis on zonal wind filtered for a 20-70 day period. The leading mode of variability associated with this EOF analysis described a modulation of the zonal wind intensity in the core of the North Pacific jet, while the second leading mode of variability described a modulation of the zonal extent of the jet. Eichelberger and Hartmann (2007) further highlighted the important role that the modulation of the jet's zonal extent plays in explaining jet variability on weekly time scales over the North Pacific. They attributed one of their analyzed modes of variability to a combination of a north-south shift, pulsing intensity, and extension/retraction of the jet stream over the North Pacific, portraying the variability of the jet on the synoptic scale to be significantly more complicated than that revealed in the analysis of Schubert and Park (1991).

Among the earliest study to note the regional impacts of interannual variability of the North Pacific jet was that of Chu et al. (1993). They showed that differences in the zonal extent of the jet had an enormous impact on rainfall in Hawaii as a zonally retracted (extended) jet in 1982-83 (1981-82) was associated with an extremely wet (dry) winter. Otkin and Martin (2004) constructed a synoptic climatology of Kona Low frequency near Hawaii using 10 years of ECMWF Tropical Ocean Global Atmosphere (TOGA) surface and upper-air data. They found that a retracted jet was associated with increased Kona low frequency in the central Pacific, suggesting that with the jet exit region retracted west of its climatological position near the dateline, the waveguide was absent north of the Hawaiian Islands, consequently allowing unimpeded equatorward propagation of extratropical disturbances to the subtropics in that longitude sector.

More recently, studies undertaken by Athanasiadis et al. (2010) and Jaffe et al. (2011) identified two leading modes of variability of the North Pacific jet. Both studies employed EOF analyses of unfiltered zonal wind data and found the leading mode consisted of a longitudinal shift of the North Pacific jet exit region such that in the extended phase (EOF 1+) the jet reached as far eastward as the western coast of North America, while in the retracted phase (EOF 1-) the jet extended only as far as 160°E. The second mode highlighted a 10-15° meridional shift in the jet exit region (EOF 2+, a northward shift; EOF 2-, an equatorward shift). Jaffe et al. (2011) also investigated the synoptic evolution of sudden jet retractions and found the characteristic timescale for such events was ~10 days.

Thus, of the four characteristic North Pacific jet configurations associated with the leading two modes of variability (EOF 1+, EOF 1-, EOF 2+, and EOF 2-), only the synoptic-evolution of jet retractions (EOF 1-) has been investigated. That investigation (by Jaffe et al. 2011) was undertaken by compositing on a single time of maximum jet retraction. Employment of such a method limits the ability of the composite to 1) testify to conditions spatially or temporally removed from the central region of interest and 2) capture the temporal evolution of associated large- and synoptic-scale structures.

In order to extend the perspective gained from compositing techniques and ensure signal retention at longer time lags, a more robust method of identifying and describing the synoptic-scale evolution of the jet stream structure is required. An adaptation of the extended EOF methodology (e.g. Weare and Nasstrom 1982, Wilks 2011) is presented in Chapter 2, with a discussion of results that emphasize its utility in examining the synoptic evolution of temporally coherent structures characterizing the leading modes of North Pacific jet variability presented in Chapter 3.

1.2 Tropical convection

While there is no preference for organized deep convection in the tropics, patterns in tropical deep convection (beyond tropical cyclones) were quantified by Matsuno (1966). He presented a number of analytical wave solutions that were later shown to exist in observations of the troposphere (Wunsch and Gill 1976). Organized waves consistent with the theory of Matsuno (1966) were also noted in satellite observations, suggesting the waves may serve to modulate convective activity near the equator (e.g. Chang 1970, Yanai and Murakami 1970a,b). Madden and Julian (1971, 1972) also identified a 40-50 day peak in the variability of tropical convection as identified by radiosonde data, later confirmed by Gruber (1974) using satellite data. While not consistent with any of the analytical solutions of Matsuno (1966), this oscillation, termed the Madden-Julian Oscillation (MJO), has been shown to be the dominant mode of convective variability in the tropics (e.g. Zhang 2005).

The MJO has generally has two phases, a convectively active phase and convectively suppressed phase, that occur with a zonal wavenumber 1 or 2 pattern and a period of 30-90 days (Zhang 2005). These phases tend to occur sequentially, such that strong convectively active and suppressed phases tend to be adjacent. Although the deep convection within the envelope of the active phase of the MJO has no preferential motion, the phase speed of the broad MJO phases can range from 5 to 15 m s^{-1}. As a result, the convectively active phase of the MJO may support enhanced convection at a single location for 1-3 weeks. As shown by Gill (1980), heating due to deep convection at any one location can force a response in the mid-latitude circulation, suggesting prolonged deep convection at any one location may be able to force a prolonged mid-latitude response. Although the MJO does serve to increase the likelihood of aggregate deep convection, it is not the only means by which tropical convection is modulated. Higher frequency convectively-coupled equatorial waves (e.g. Kiladis et al. 2009) move through the convectively active and suppressed envelopes of the MJO to further modulate convective activity. Lower frequency convective modes also occur, such as the convective modulation forced by warmer or colder sea surface temperatures during El Niño-Southern Oscillation events (e.g. Zhang

1993). While a large fraction of convective activity is modulated by these low- and high-frequency modes of variability, these phenomena do not account for all of the convective variability in the tropics. Convection that is aggregated, yet otherwise unorganized, may still elicit a mid-latitude response akin to that described by Gill (1980). Gill does not prescribe any particular organization in his simulations, suggesting that the organization of deep convection may not limit its ability to interact with the mid-latitude circulation. The impact of this convection, regardless of its organization, on the mid-latitudes has been firmly established in other studies discussed in the following section.

1.3 Tropical-extratropical interaction

Since shortly after the discovery of the jet stream as a narrow, sinuous ribbon of fast-moving air in the upper troposphere (e.g. University of Chicago 1947, Yeh 1950, Lewis 2003), interactions between the mid-latitude jet and the tropics have been a focus of study for research inquiry (e.g. Namias and Clapp 1949, Mohri 1953, 1959). Early studies focused on the role of tropical cyclones (TCs) and their impacts on the jet stream inasmuch as the interactions could be observed via land-based observations (e.g. Mohri 1953, 1959). Mohri (1959) in particular emphasized the importance of such interactions, stating that "the close relationship between the subtropical jet stream and the northward outbreak of tropical air in the upper troposphere is stressed to be a basic important process in the general circulation." He identified these northward outbreaks of tropical air by tracking their characteristically cold upper-tropospheric temperatures and low absolute vorticity, noting that as such air approached the jet stream the upper-level thermal gradient often intensified. In addition, Mohri (1959) described the relationship between 300-200-hPa lapse rate and 200 hPa temperature, noting that colder temperatures at 200 hPa were commonly associated with a larger lapse rates and therefore reduced static stability in that isobaric layer.

Krishnamurti (1961) depicted a continuous jet stream axis encircling the globe at subtropical latitudes. Within this narrow ribbon, local maxima in wind speeds were observed near the eastern coasts of North America and Asia as well as over northeast Africa and the Middle East. Figure 2 of Krishnamurti (1961; not shown) highlighted that local wind speed maxima in the subtropical jet generally occur where the jet reaches farthest north. Reiter and Whitney (1969) noted that the subtropical jet and polar jet interact when in close proximity to one another over North America, implying that interactions between the subtropics and the mid-latitudes may preferentially occur where the subtropical jet reaches farther north and the two jet streams are, on average, the closest to each other.

Near-equatorial heating was shown to impact the general circulation both locally and remotely by Gill (1980). Closely following Gill's work were studies by Hoskins and Karoly (1981) and Horel and Wallace (1981) quantifying the remote response of the mid-latitude circulation to equatorial convection and identifying Rossby waves as a component of this mid-latitude response. Deep convection associated with the MJO (Madden and Julian 1972, 1994; Zhang 2005) was also shown to have an impact on the mid-latitude circulation by Weickmann (1983). More generic studies of tropical convection (e.g. Reiter 1983, Liebmann and Hartman 1984) showed connections with standing wave patterns as observed by anomalous mid-latitude heights on both daily and monthly timescales. Kiladis and Weickmann (1992, 1997) demonstrated the consistently wave-like response of the mid-latitude flow to anomalous convection at various locations across the tropics. These studies commonly focus on the upper-level divergence above the convection, but there is little discussion of the physical connections that link this relatively local effect to events on the other side of an ocean basin several days later. Within these studies and others like them, little effort is directed toward developing a physical explanation of *how* convection in the tropics is responsible for such impacts.

One way tropical convection impacts the mid-latitudes is through the local effects of divergence. This has been shown in other studies of tropical-extratropical interaction that focus on the process of the extratropical transition of TCs, often referred to as ET. Jones et al. (2003) defined ET as an evolutionary process by which a TC loses tropical characteristics and becomes more extratropical in nature. During this process, the progression of the TC into mid-latitudes intensifies the interaction between the TC undergoing ET and the mid-latitude jet stream poleward of the TC. Studies of these interactions have emphasized the importance of the co-evolving growth of both positive and negative potential vorticity (PV) anomalies along the jet stream (e.g. Thorncroft and Jones 2000, Riemer et al. 2008). Some studies have placed particular emphasis on the amplification of a ridge downstream of the transitioning cyclone via both the poleward transport of tropical air and diabatic effects (e.g. Riemer and Jones 2010, Grams et al. 2011, 2013, Archambault et al. 2013, 2015). Archambault et al. (2013) identified the role of the upper-level advection of anomalous PV by the irrotational wind emerging from a TC in intensifying the north Pacific jet stream and exciting a Rossby wave train that then propagated downstream and led to high-impact weather over North America. Diagnosing and quantifying the local impact of the divergent wind from the convection associated with

TCs undergoing ET (or otherwise interacting with the mid-latitudes) provides a physical mechanism by which TCs can influence the mid-latitude circulation, but only through a direct interaction with a jet. It seems likely that additional interactions between the results of deep convection and the mid-latitude circulation occur via the remaining non-divergent component of the flow, especially if this flow is sustained over a period of up to several days. Such a response has not been widely examined in previous studies and merits additional investigation.

An alternate perspective presented by Jaffe et al. (2011) focuses primarily on the variability of the North Pacific jet stream, highlighting the convective signals associated with the first EOF of zonal wind over the North Pacific (jet retraction). In studying the jet retraction events, they found that the characteristic timescale of such retractions is on the order of 10 days and is characterized by the rapid development of a strongly anomalous ridge over the eastern Pacific and anomalous trough over western North America. This pattern, similar to the negative phase of the PNA (Wallace and Gutzler 1981), emphasizes the role the North Pacific jet plays as a precursor to potentially high-impact weather downstream. Jaffe et al. (2011) also examine the nature of tropical convection leading up to, during, and after the beginning of each jet retraction event via a time-lagged composite analysis. In these composites (their Fig. 12; not shown), negative anomalies of OLR appear over Indonesia as the retraction events begin and the anomalies continue to grow over the subsequent ten days while remaining quasi-stationary. While little explanation is provided as to a physical mechanism linking the anomalous convection to the jet retraction, the contemporaneous nature of the events motivates further exploration of any potential relationship between the two.

The nature of the relationship between tropical convection and jet retraction events identified by Jaffe et al. (2011) becomes increasingly tenuous at longer leads and lags. This attenuation may stem from the general problem of attempting to identify relationships across a range of spatial and temporal scales. The "temporal mismatch" problem is mentioned by Roundy (2015) and implied in a number of other studies that attempt to bring high-frequency mid-latitude patterns together with an assortment of temporally varying patterns in the tropics. The challenge of improving the overall understanding of tropical-extratropical interactions was the focus of a World Meteorological Organization workshop and subsequent report (Montcrieff et al. 2007) in which the importance of further research on tropical-extratropical interactions was highlighted as a potential key to improving operational forecasting into week two and beyond.

The remainder of this dissertation is presented as follows. A summary of the data sources and statistical analysis techniques utilized are presented in Chapter 2. A study of the leading modes of synoptic-scale variability of the North Pacific jet stream as determined by time-extended EOFs (TE-EOFs) is presented in Chapter 3. Emphasis is placed on the construction of composites based upon peaks of each mode of variability and examining the upstream synoptic-scale patterns that precede such events as well as the resultant downstream impacts over North America. Chapter 4 presents a novel diagnostic, isentropic pressure depth, that follows the upper tropospheric mass exhausted by deep convection in the tropics and mid-latitudes. A discussion of how gradients of isentropic pressure depth associated with vertical geostrophic wind shear can impact the mid-latitude circulation via the jet stream in a quantifiable manner is also included. Finally, Chapter 4 also presents a case study of the events preceding the March 2012 North

American warmth to demonstrate some of the utility of isentropic pressure depth. Chapter 5 revisits the composite analysis technique from Chapter 3, constructing additional composite analyses using isentropic pressure depth with a focus on improved diagnosis of upstream synoptic-scale features preceding each phase of the two leading modes of jet variability. Given the utility of isentropic pressure depth in tracking the impact of deep convection on the mid-latitude circulation, additional emphasis is placed on identifying where any connections exist between anomalous deep convection and North Pacific jet variability.

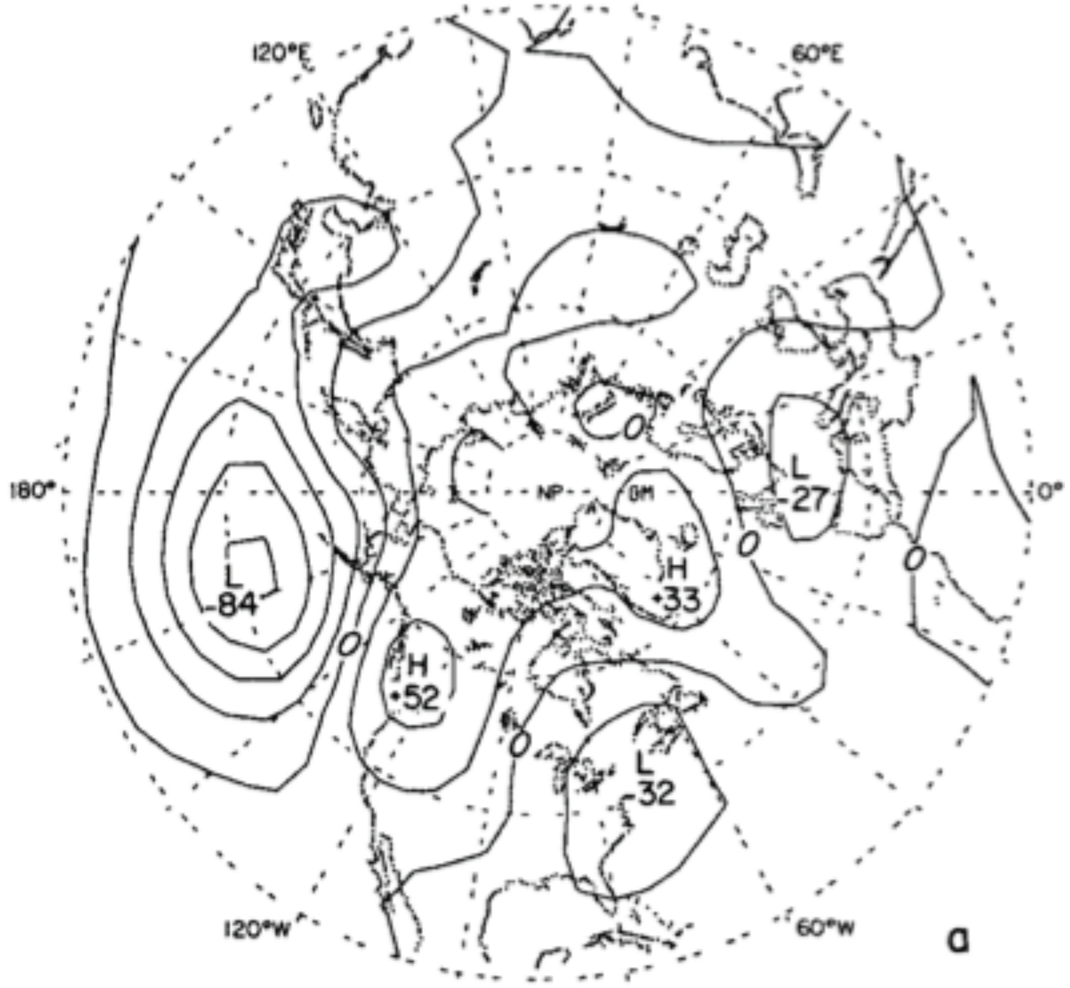

Figure 1.1. Composite anomaly map of the 700 mb height anomalies over five cold eastern United States winters, specifically 1960-61, 1962-63, 1967-68, 1969-70, and 1976-77. From Wallace and Gutzler (1981; their Fig. 5a).

2. Data and Methodology

The statistical tools utilized in Chapters 3 and 5 are presented here. While none of the tools and techniques described are novel, previous uses of time-extended EOFs in the analysis of synoptic-scale mid-latitude patterns appear intermittent at most, and additional discussion of the motivation behind its use is provided. It should be noted that the description of isentropic pressure depth, a novel diagnostic, is reserved for Chapter 4 to ensure a coherent presentation and discussion of the diagnostic and the corresponding analyses.

2.1 EOF techniques

EOF analysis is a statistical method by which the modes of variability that describe a multi-dimensional dataset are identified (e.g. Hannachi 2004, Wilks 2011). The patterns of greatest interest in an EOF analysis are those that explain the largest fraction of variability within that dataset. In the atmosphere, EOF analyses provide insight into the primary modes of variability associated with a particular atmospheric variable over a pre-defined spatial region and period of time. Use of EOF analyses has led to the identification and analysis of large-scale patterns in the atmosphere (e.g. the PNA, Wallace and Gutzler 1981; AO, Thompson and Wallace 1998), although not all EOFs have a meaningful physical interpretation. Each mode of variability identified by an EOF analysis is defined to be statistically independent of and orthogonal to all other modes, such that any one mode has no correlation with any other mode. In complex systems, such as the atmosphere, the asserted mathematical independence of each mode need not be mirrored in reality. However, when physical insight is combined with the statistical results of EOF analyses, the combined analysis can lead to understandings that neither the physics nor statistics might provide alone.

The traditional EOF analyzes a temporal sequence of spatial information to determine patterns of spatial co-variability without providing any sense of how such a pattern may evolve through time. By extending the input data to include a temporal dimension, EOF analysis can identify the time-dependent evolution of spatial patterns. This particular extended EOF (Weare and Nasstrom 1982, Wilks 2011) has been termed a time-extended EOF (TE-EOF; Roundy and Schreck 2009) and describes the leading modes of spatial-temporal evolution for the analyzed data. TE-EOF analysis incorporates temporal variability by considering a number of times either side of a central reference time. By doing so, temporal data is incorporated into the TE-EOF twice – once as a way to maintain the coherence of data related to the evolution of the pattern over a, for instance, 10-day window (the additional TE-EOF dimension, termed a "TE window") and once as the time series over which to calculate the eigenmodes and identify the patterns (or, for TE-EOFs, the temporal evolutions) associated with each mode of variability. Weare and Nasstrom (1982) introduced the concept of extended EOF analysis in the atmospheric sciences and emphasized the utility of extended EOFs that incorporate additional temporal data due to the "significant auto- and cross-correlations in time" associated with the broad similarities shared by any two consecutive atmospheric states. Extended EOFs have been utilized to produce multivariate extended EOF analyses (calculated with multiple variables instead of multiple times), such as those used by Wheeler and Hendon (2004) to monitor the MJO and the time-extended EOF analyses used to forecast organized modes of tropical convection by Roundy and Schreck (2009).

The TE-EOF analyses performed here and in Chapter 3 were constructed with data from the NCEP/NCAR Reanalysis (Kalnay et al. 1996) with data at 2.5° horizontal grid spacing and 6-hourly resolution. This data provides an EOF analysis of comparable quality to one constructed from an analysis with finer horizontal resolution such as the Climate Forecast System Reanalysis (CFSR; Saha et al. 2010). A coarser analysis has been used here due to the additional computational load that stems from the use of an analysis with a smaller horizontal grid spacing to provide an otherwise similar TE-EOF analysis. Zonal wind at the 250-hPa level was used at each analysis time throughout the winter months of November – March (NDJFM) to represent a level where the jet stream commonly resides. The chosen spatial domain of 100°E–120°W and 10°N–80°N allows sufficient space around the entrance and exit regions of the North Pacific jet stream in order to fully capture the variability directly associated with each. The TE-EOFs are performed using a TE-window of 40 6-hourly time periods (10 days) of zonal wind anomalies beginning at each 6-hourly time step during NDJFM. These times are buffered by 5 days at the beginning of November and end of March to include only TE windows that fall completely within the NDJFM period. For example, the first (second) TE window in this analysis extends from 0000 UTC 1 Nov to 1800 UTC 10 Nov (0600 UTC 1 Nov to 0000 UTC 11 Nov) and is represented by the central time of 0000 UTC 6 Nov (0600 UTC 6 Nov).

In constructing the TE-EOF analyses, tests were performed to examine the sensitivity of the resulting TE-EOF 1 and TE-EOF 2 patterns to the chosen temporal and spatial constraints on the domain. Given the broad similarity of DJF and NDJFM zonal wind EOFs (not shown), and in order to reduce calculation time, the TE-EOFs for the sensitivity tests were calculated only over the DJF period. To test temporal constraints, the TE window length was varied from 6 days to 16 days, showing only minor changes in the TE-EOF patterns. Numerous variations of the spatial domain were tested, both increasing and decreasing the extent in all directions. Expansions of the domain captured the large zonal wind variability associated with other climatological jet streams over central Asia and eastern North America, but did not significantly impact the pattern over the North Pacific. The spatial dimensions of the domain specified above were therefore chosen to focus on variability of the North Pacific jet while excluding other remote regions of high zonal wind variability.

The utility of the TE-EOF methodology is evident when comparing the resultant principal components (PCs) to the PCs of a traditional EOF analysis on the same data. PCs represent a measure of how well the data at a given time project back onto a given mode of variability. A time series of PCs provides a running measure of this projection and is standardized to aid interpretation. For the NDJFM months of 2009-2010, Fig. 2.1 compares the TE-PC (from a 10-day TE window) to the traditional PC (instantaneous; calculated every 6 h) and the 10-day centered running mean of the traditional PC. While the traditional PC captures more variability of the state of the North Pacific jet stream on short time scales, this PC constructed with data from an individual time has no inherent regard for maintaining temporal coherence and appears noisy at times. Smoothing the traditional PC time series over 40 points (10 days) provides values that appear similar to, but are generally of smaller magnitude than, the TE-PC values. As a result, the TE-PC better captures the full magnitude of highly anomalous events on the 10-day timescale while eliminating much of the noise from higher-frequency variability, facilitating a focus on events on the synoptic time scale. While Fig. 2.1 contains data only for the 2009-2010

NDJFM season, similar comparisons hold across all winters since 1980-1981 and suggest the TE methodology is well suited for identifying intraseasonal shifts in the structure of the North Pacific jet stream.

It is important to note that the TE modes are defined in a manner that does not require that peaks in a PC from a traditional EOF technique correspond to peaks in the TE-PC. The TE-PC captures the broader evolution of the pattern without accounting for higher-frequency signals that may project onto the traditional EOF patterns yet lack temporal longevity. It is likely these types of peaks in the PC are not captured by the TE-EOF and may account for some of the lower percent of variance explained with each TE mode when compared to the corresponding traditional EOF over the North Pacific region[1]. Such a reduction in explained variance by a given TE-EOF is also related to the larger number of data points employed in the construction of the TE-EOF, providing increased variability for which to potentially account (Weare and Nasstrom 1982).

2.2 Composite analyses

In order to supplement the TE-EOF analysis of the zonal wind field with physical analysis, composite analyses of high-amplitude events in the TE-PC time series were constructed for events between November and March for the years 1980–2010. These composites were constructed with anomalies calculated by subtracting a 21-day centered running mean from the individual time at the center of the 21 days. Means were calculated using the same NCEP/NCAR Reanalysis (Kalnay et al. 1996) used to calculate the TE-EOFs.

---

[1] The percent variance explained in Jaffe et al. (2011) for EOF 1 is 15.9%, compared to our 9.1%. Our TE-EOFs are calculated using approximately 40 times the number of data points than used in a traditional EOF analysis.

Such composites allow for an examination of the synoptic-scale patterns preceding and following high-amplitude peaks in given modes of jet stream variability. In addition, outgoing longwave radiation (OLR) anomalies from the NOAA Interpolated OLR dataset (Liebmann and Smith 1996) were utilized in constructing additional composite analyses in order to serve as a reasonable proxy for anomalous cloud cover and convection in the tropics and subtropics. These data facilitate a comparison of what, if any, tropical or subtropical convective patterns may occur in conjunction with the leading modes of zonal wind variability. In these composites, D0 will refer to date and time where a local maximum (or minimum) in the given TE-PC exceeded the prescribed threshold, while D-5d and D+5d will refer to the dates five days prior to and five days following D0, respectively.

In Chapter 5, composite analyses of isentropic pressure depths are constructed based upon local extremes in the PCs corresponding with the leading modes of North Pacific jet variability. The technique used to choose the dates upon which to center those composites is identical to that used in Chapter 3 for each of the phases associated with the two leading modes of variability. Composite analyses in Chapter 5 focus on anomalies of isentropic pressure depth in both the 315-330 K and 340-355 K isentropic layers. The composite analyses were computed for the positive and negative phases of both TE-EOFs 1 and 2 and the composites were lagged 15 days backward and 10 days forward from the center of the 10-day time extension (TE) window (referenced as D0) used by the TE-EOFs. While Chapter 3 provides significant discussion of the downstream impacts associated with each phase of the two leading modes of North Pacific jet variability, the pressure depth analyses in Chapter 5 have a greater focus upon diagnosing the events preceding and coincident with the TE window.

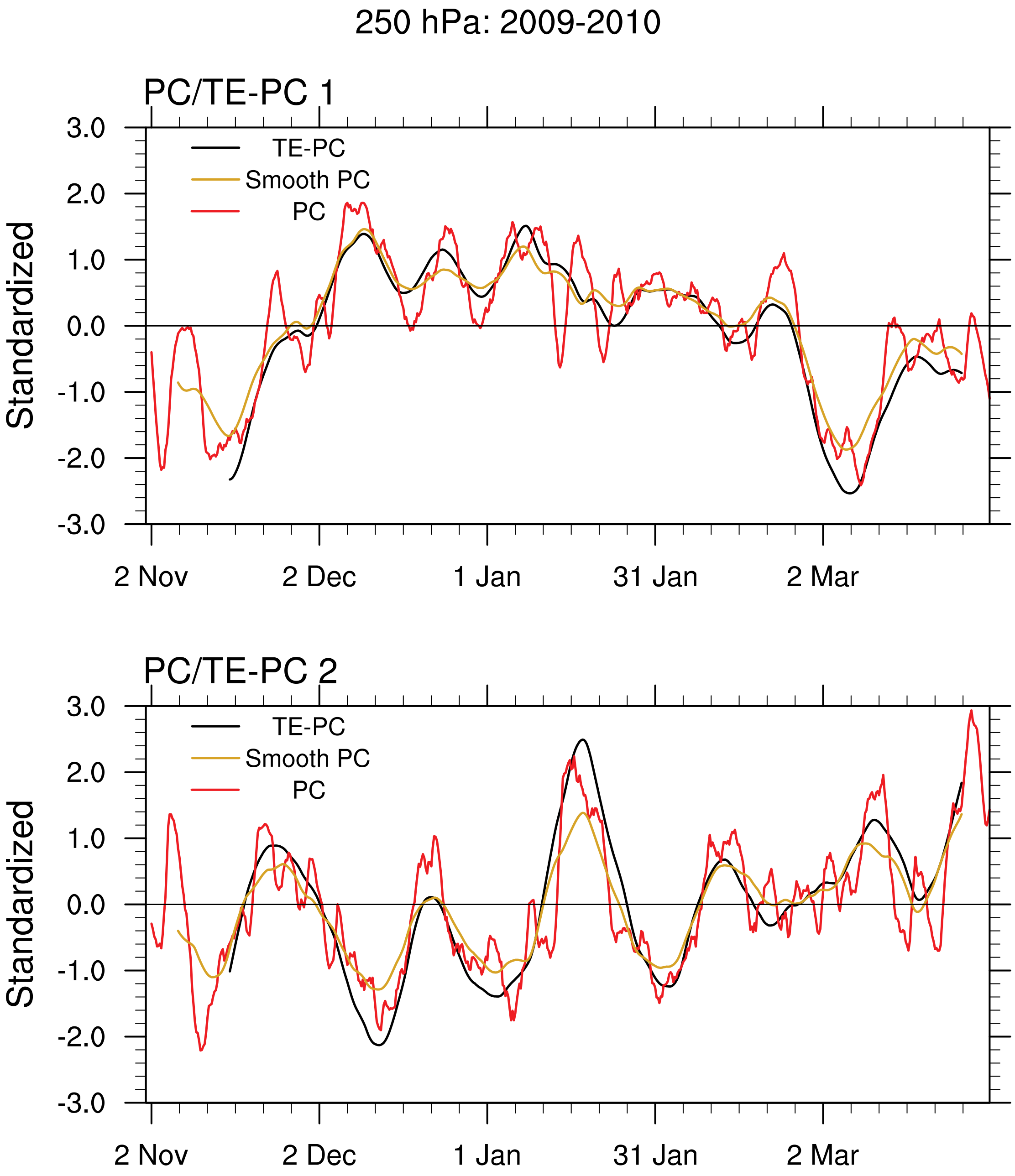

Figure 2.1. Comparison of a traditional PC, a traditional PC with a 10-day smoother, and a TE-PC for the NDJFM 2009-2010 season for the leading mode (top) and second leading mode (bottom) of variability. PCs correspond to EOFs of 250 hPa zonal wind speed over the North Pacific.

3. Synoptic features associated with temporally coherent modes of variability of the North Pacific jet stream

3.1. Overview

Previous studies identifying the leading modes of variability of the North Pacific jet stream (Athanasiadis et al. 2010, Jaffe et al. 2011) have identified both a jet extension/retraction mode (EOF 1) and a poleward/equatorward shift mode (EOF 2). In their study, Jaffe et al. also examine the characteristic time scale of a jet retraction event, finding the process of retraction typically occurs over ~10 days. They constructed composite analyses based on dates of jet retraction to identify synoptic-scale features that occur in the days prior to and following jet retraction events. However, the coherency of these composites appeared limited at larger time lags due to the use of a single time of maximum jet retraction without also considering the evolution of the jet stream prior to and following that time.

In order to enhance the degree of temporal coherency in the construction of composites and to improve signal retention at longer time lags, a more robust method of identifying and describing the evolution of the jet stream structure is required. Here, we adapt the extended EOF methodology (e.g. Weare and Nasstrom 1982, Wilks 2011) to examine the synoptic evolution of temporally coherent structures characterizing the leading modes of North Pacific jet variability. A description of the time-extended EOF (TE-EOF) method, along with details of its implementation in this study, has already been provided in Section 2.1. Section 3.2 describes the jet variability on synoptic timescales within the TE-EOF framework. Time-lagged composites, constructed as described in Section 2.2 and based on the TE-EOF analysis, highlighting synoptic features both over the North Pacific and associated with downstream impacts over North America are presented in Section 3.3. Additional time-lagged composites of anomalous deep convection are constructed via the same methodology and presented in Section 3.4. A summary and suggestions for future work are discussed in Section 3.5.

3.2. Preferred modes of variability

The TE-EOF analyses presented here remain consistent with the leading modes of jet stream variability identified by previous work while explicitly incorporating the temporal evolution of synoptic-timescale patterns in the North Pacific jet stream into the analyses. Previous work has shown the spatial patterns associated with the leading modes of variability of the zonal wind over the North Pacific (e.g. Fig. 4 of Athanasiadis et al. 2010, Fig. 4 of Jaffe et al. 2011) to be similar to the patterns associated with the two leading modes of variability found at the central day (D0) of the TE-EOF analysis as shown in Fig. 3.1 (TE-EOF 1) and Fig. 3.2 (TE-EOF 2). The two other panels of Figs. 3.1 and 3.2, labeled as D-5d and D+5d, represent the beginning and end of the TE window, respectively. It is important to recognize that the sign associated with any EOF analysis is arbitrary and the signs of the TE-EOFs presented here have been chosen in a manner consistent with previous literature.

TE-EOF 1 is comprised of zonal wind variability along the latitude of the climatological jet core (~35°N), with the mode's primary center of action located in the exit region of the climatological jet. Figure 3.1 presents the zonal wind anomalies from the NCEP/NCAR Reanalysis regressed back onto the TE-EOF pattern, resulting in a maximum anomaly in excess of 24 m s^{-1} at D0 (Fig. 3.1b). This anomaly represents the extension (when positive) and retraction (when negative) events of the North Pacific jet characterized by TE-EOF 1. A second set of anomalies of the opposite sign can be found both poleward and equatorward of the maximum anomaly in the jet exit region. In general, the large-scale TE-EOF anomalies maximize in intensity near the central time of the 10-day TE window (D0).

TE-EOF 2 represents a meridional shift in the exit region of the climatological jet stream, described by a pair of anomalies of opposing sign straddling the climatological latitude of the jet stream (Fig. 3.2). Such a pattern indicates a shift of the zonal wind to the flank of the climatological jet exit region. The northern (southern) anomaly center, when positive, represents a poleward (equatorward) shift in the jet exit region. These distinct shifts correspond, respectively, to the positive and negative phases of TE-EOF 2.

3.3. Composite analysis

In order to provide insight into the evolution of the synoptic-scale patterns associated with each phase of the two modes of variability, four separate composites were constructed. Each instance in which a given PC's value reached a local maxima or minima in excess of ±1.5 standard deviations was selected for the composite. Anomaly data from upper (250 hPa) and lower (850 hPa) levels at the selected times were averaged to produce each composite. The same NCEP/NCAR Reanalysis anomaly data described in Section 2.1, and used to originally construct the TE-EOFs, were also employed in the construction of the composites.

3.3.1. Extension (positive TE-EOF 1)

The composite analysis of TE-EOF 1 in its positive phase, created from 40 individual maxima in the PC of TE-EOF 1, is presented in Figure 3.3. When in its positive phase, TE-EOF 1 represents an extension of the climatological jet over the North Pacific, with the strongest zonal wind anomaly at D0 located near 35°N and 165°W (Fig. 3.3c), firmly embedded within the exit region of the climatological jet. At upper levels, a negative height anomaly in the central North Pacific at D-10d (Fig. 3.3a) supports a 10 m s^{-1} zonal wind anomaly on it southern flank in the exit region of the climatological jet. Strengthening to 15 m s^{-1} by D-5d (Fig. 3.3b), the zonal wind anomaly extends from 150°E to 140°W while remaining equatorward of an anomalous upper level trough and associated low-level anomalous cyclone (Fig. 3.3g) south of the Aleutian Islands. This low-level cyclone is supported at upper levels by its location in the poleward exit region of the extended jet, a region favorable for cyclone development.

Near the Asian coast at D-10d (Fig. 3.3a), an anomalous upper level trough supports an enhancement of the wind speeds on the anticyclonic shear side of the climatological jet. This enhancement strengthens and zonally elongates by D-5d (Fig. 3.3b), increasing upper-level flow out of the tropics near the Asian coast and zonally extending jet near 180° longitude. Over time, this trough merges with the broader trough in the central North Pacific (Fig. 3.3c, d). There, the anomalous height differential (over 300 m) between 20°N and 40°N is greatest at D0 and is tied to a zonal wind anomaly of ~30 m s^{-1}, effectively doubling the zonal wind in this jet exit region (Fig. 3.3c). The enhancement of the zonal wind in the jet exit region extends the climatological jet 20° farther east, approaching the west coast of North America. This jet naturally follows the southern edge of the anomalously low heights associated with the central Pacific trough. Beneath the upper trough, the 850-hPa cyclone continues to develop (-180 m minimum height anomaly) and maintains its position in the poleward exit region of the extended jet as both shift eastward (Fig. 3.3f-h). By D+5d, the upper trough remains sprawling and moves the jet even farther east (Fig. 3.3d) before weakening and returning to the central North Pacific by D+10d (Fig. 3.3e). Accordingly, the anomalous 850 hPa cyclone begins to shift onshore over western North America (Fig. 3.3i), indicating the low-level cyclone is increasingly impacting the sensible weather over North America.

It is interesting to note that the height and zonal wind anomalies over eastern Asia at D-5d, particularly those tied to the ridge over central Siberia and the trough over the Korean peninsula, weaken through D0 and are essentially absent by D+5d. Given that the intensity of each peaks early in the TE window, this evolution suggests that these two features identify precursors to jet extension events over the North Pacific. This upper-level trough and ridge are also represented in the 850 hPa temperature anomalies, with anomalous warmth over central Siberia and anomalous cold (in excess of -3˚C) over eastern China at D-5d (Fig. 3.3g).

Downstream over North America, height anomalies start to amplify by D0, with an anomalous 250 hPa ridge over western Canada (Fig. 3.3c) associated with 850 hPa temperature anomalies in excess of 2˚C (Fig. 3.3h; only statistically significant along the western coast of Canada). Farther downstream over the eastern portion of the United States and maritime Canada, an upper-level trough develops (Fig. 3.3c) in association with a small region of low-level cold anomalies in excess of -2˚C at D0 (Fig. 3.3h). This anomalous trough over eastern North America is consistent with an enhancement of the upper jet on its equatorward edge, resulting in a stronger subtropical jet over the southeast United States. While the upper trough and low-level cold anomalies slowly slide southwestward through D+5d, the warm anomalies over western Canada intensify and expand over much of the western half of North America, peaking in excess of 4˚C (Fig. 3.3i). This widespread warmth remains at D+10d (Fig. 3.3j), though only a handful of anomalies are statistically significant.

While the 850 hPa temperature anomalies frequently exceed magnitudes of 3˚C over western Canada, these values do not exceed the threshold required for statistical significance in composites with the sample size used here. Presumably, the large standard deviation (and therefore variance) of 850 hPa temperature during NDJFM in the region in the lee of the Rockies (the standard deviation exceeds 7˚C) accounts for the non-significance of a population of the 3-4˚C anomalies.

3.3.2. Retraction (negative TE-EOF 1)

Composites of the jet retraction cases associated with the negative phase of TE-EOF 1 were constructed from 40 times in which the PC peaked below the -1.5 standard deviation threshold (Fig. 3.4). While composites associated with the negative phase of TE-EOF 1 are not statistically required to be mirror opposites of the positive phase of TE-EOF 1 (due to the varying amplitudes of the cases used in the composite mean), the large-scale structures describing the two phases tend to exhibit this characteristic.

At upper levels at D-10d (Fig. 3.4a), small positive height anomalies are located in the central North Pacific just north of the exit region of the climatological jet, supporting a small ~10 m s^{-1} negative zonal wind anomaly in the exit region. By D-5d (Fig. 3.4b), the anomalous upper level ridge south of the Aleutians intensifies significantly and expands along the entire northern flank of the climatological North Pacific jet. The core of the negative zonal wind anomalies is located near 180°, resulting in a retraction of the jet to west of the date line. Negative zonal wind anomalies peak at D0 in excess of -30 m s^{-1} with these cases (Fig. 3.4c) in a region where the climatological wind is only ~45 m s^{-1}. Centers of enhanced zonal winds exist both poleward and equatorward of the climatological jet stream with the positive zonal wind anomaly stronger on the poleward side. A modest upper-level trough appears west of Hawaii at D-5d (around 20°N and 180° longitude; Fig. 3.4b) and exists throughout the 10-day TE window, expanding eastward with time. Anomalous cyclonic flow around this upper trough further supports the reduction in climatological westerlies in combination with the anomalous anticyclonic flow around a much more substantial high-latitude ridge (centered near 45°N), creating a pattern similar to a Rex block (or dipole-type block; Rex 1950) and suggesting a possible stagnation of the pattern over the eastern North Pacific and downstream.

East Asian precursors are comparable but roughly opposite of those of the jet extension mode (Fig. 3.3b, g and 3.4b, g). Most of Siberia is dominated by a sprawling upper-level trough (Fig. 3.4a, b) and low-level cold anomalies (below -4°C; Fig. 3.4f, g), while east-central China and the Sea of Japan are dominated by the western lobe of a ridge in the central Pacific that slowly contracts eastward with time in the 10-day TE window (Fig. 3.4b-d). The anomalously cold air, largely in Siberia initially (Fig. 3.4g), spreads eastward to encompass Alaska and western Canada where anomalous cold exceeds -5°C by D0 (Fig. 3.4h).

The downstream patterns are of similar amplitude and evolve comparably to those observed in jet extension composites, but are again of reversed sign (Fig. 3.3d, i and Fig. 3.4d, i). A broad region of anomalously low heights at 850 hPa can be seen sliding out of the Arctic Ocean around D0 (Fig. 3.4h) and into western Canada by D+5 (Fig. 3.4i), drawing cold air into Alaska for at least 10 days after peak retraction (Fig. 3.4h-j). While the low-level negative height anomalies over North America disappear by D+10d (Fig. 3.4j), the upper level height anomaly dipole remains significant over the central Pacific and the anomalous zonal wind magnitude remains above 15 m s^{-1} beyond D+10d (not shown).

3.3.3. Poleward shift (positive TE-EOF 2)

Two primary centers of action straddling the mean jet exit region dominate the 10-day composite analyses of 36 poleward shifted jet cases (cases exceeding +1.5 standard deviations of TE-EOF 2). A strip of positive zonal wind anomalies north of the climatological jet axis and negative anomalies south of the climatological jet axis serves to shift that climatological jet poleward, from as far west as western China at D-10d (Fig. 3.5a) to the northwest US beyond D0 (Fig. 3.5c, d). The strongest zonal wind anomalies are predominantly located poleward of the climatological jet exit region.

A poleward shift of the jet similarly shifts the synoptic-scale height anomaly centers 10-15° poleward of the climatological jet axis. A zonally elongated anomalous ridge centered near the latitude of the climatological jet core but in the jet exit region (Fig. 3.5a) contrasts with a broad anomalous upper-level trough over the western Gulf of Alaska and far eastern Russia by D-5d (Fig. 3.5b), helping to shift the pattern poleward and intensify the jet between the height anomalies at D-5d. The negative height anomaly and its associated anomalous low-level cyclone retrograde across the Aleutian Islands and intensify from D0 through D+10d (Fig. 3.5c-e). The intensification of this negative upper-level height anomaly suggests an amplification of the flow may contribute to the downstream intensification of the positive height anomalies over Hudson Bay by D+5d (Fig. 3.5d). While there are no significant temperature anomalies associated with the anomalous low-level cyclone near the Aleutians before D-5d (Fig 3.5f, g), the anomalous tropospheric deep cyclonic flow enhances the low-level cold (warm) temperature anomalies present over the Bering Sea (central Canada; Fig. 3.5h-j). While the cold temperature anomalies over far eastern Russia peak in excess of -4˚C at D+5d (Fig. 3.5i), the corresponding warm anomalies over central Canada appear to be enhanced by southwesterly winds downsloping off the Rocky Mountains on the southwest side of the anomalous Aleutian cyclone and peak in excess of +8˚C at D+5d. This anomalous warmth continues to impact northeastern North America at D+10d (Fig. 3.5j), although the statistically significant portion of these anomalies becomes limited.

Upstream of the North Pacific, a weak and nearly stationary anomalous ridge is present near the entrance region of the climatological jet at 110˚E (D-10d and D-5d, Fig. 3.5a,b). This anomalous ridge is maintained throughout the 20 day composite, suggesting its presence may be related to a persistent forcing such as deep convection. If so, its presence at D-10d and D-5d may prove to be a key precursor feature for poleward shifted jet events. An additional notable upstream precursor appears as an anomalous shortwave trough over Mongolia at D-10d (Fig. 3.5a) and near the Korean peninsula at D-5d (Fig. 3.5b).

3.3.4. Equatorward shift (negative TE-EOF 2)

The upper-level zonal wind pattern associated with the equatorward shift mode (negative phase of TE-EOF 2) is more challenging to interpret than the composites associated with the other phases. The primary zonal wind anomalies in the composite straddle the climatological jet exit region with enhanced westerlies located on the southern periphery with a stronger region of reduced westerlies to the north prior to and throughout the 10-day window (Fig. 3.6a-d). This structure is similar to but opposite that of the positive phase of TE-EOF 2 and is termed “equatorward shift.” While such a description allows for a convenient consistency in nomenclature, the anomalous enhancement of upper-level zonal winds over Alaska and eastern Russia is of equal or greater magnitude than the enhanced westerly flow in the subtropics and may instead represent an invigorated polar jet stream (Fig. 3.6b-d). Poleward shifted jet events are not characterized by negative zonal wind anomalies in a similar location (Fig. 3.5b-d), providing a notable asymmetry between the positive and negative phases of TE-EOF 2.

The equatorward shift mode is comprised of anomalous westerly zonal wind along 20°N latitude in the central Pacific throughout the composite, with the maximum westerly anomaly over the Hawaiian Islands (Fig. 3.6a-d). This anomalous jet extends eastward from its D-5d position (Fig. 3.6b) and connects with an anomalous wind speed maximum over central North America, creating a link between the enhanced equatorward-shifted subtropical Pacific jet and the climatological jet stream over Mexico and the United States by D0 and D+5d (Fig. 3.6c, d). A broad anomalous trough dominates the flow over the western United States and central Canada and acts in concert with a weak anomalous ridge in the southeast United States to enhance the upper winds between the anomaly centers.

The upper trough is associated with remarkable cold anomalies in excess of -8°C at 850 hPa over much of Canada (Fig. 3.6f-h). The magnitude of these anomalies increases dramatically as they become statistically significant between D-5d and D0 (Fig. 3.6f, g). Though the underlying physical mechanism driving these local temperature tendencies is not immediately clear, some of the local temperature decrease is likely associated with cold air advection in northwesterly low-level flow over Alaska and northwestern Canada stemming from the intensifying low-level anticyclone over the Aleutian Islands (Fig. 3.6f-h).

Over the central North Pacific, a strong anomalous upper-level ridge broadly dominates north of 40°N and enhances the jet stream on its poleward flank, north of 60°N (Fig. 3.6b-d). The cross-arctic flow associated with such a jet is also represented at the 850-hPa level and likely contributes to the anomalous low-level cold in North America at D0 and D+5d (Fig. 3.6g, h). South of this ridge, a broad region of anomalously low upper-level heights is present south of the climatological jet near its exit region and may represent broad upper troughs digging into the subtropics across a range of longitudes in a manner similar to that observed in jet retraction cases (e.g. Fig. 3.4a-e). The position suggests a connection to the Kona lows that occur in conjunction with retracted jet cases (e.g. Otkin and Martin 2004) and any such trough may slightly enhance the subtropical jet south of the trough in this region.

The upstream patterns over Asia are diffuse with no clear-cut synoptic-scale anomalies at D-5d or D0 at upper levels (Fig. 3.6b, c), suggesting that either the equatorward shift mode may be triggered by well-defined but opposing synoptic-scale setups that cancel out in a composite mean analysis or that there are not any clear cut Asian mid-latitude precursors to these equatorward-shifted jet cases.

3.4. Tropical convection composites

Although some results from the poleward shifted jet composite suggested a connection to tropical convection, specifically the building of low-latitude anomalous ridges, such inferences are unsupported without examining proxies of the convection itself. Jaffe et al. (2011) performed such composites for retracted jet cases, finding a quasi-stationary convective signal both before and after a jet retraction event. Figures 3.7 and 3.8 present OLR composites calculated as discussed in Section 3.3 for each phase of each TE-EOF. OLR is often utilized as a proxy for cold cloud tops associated with deep convection in the tropics and subtropics and is useful in the construction of composites due to its long, homogenous period of record. The OLR composites for the extension mode (Fig. 3.7a, c, e) and the equatorward shift mode (Fig. 3.8b, d, f) show little or no apparent large-scale organization of anomalous enhanced tropical convection.

Anomalous tropical convection appears in the retraction composite over the eastern Indian Ocean and Maritime Continent (Fig. 3.7b, d, f) and appears to move slowly eastward across the 10-day window of the composite. The eastward phase speed of this convection appears similar to or slightly slower than that of convection associated with the Madden-Julian Oscillation (MJO; Madden and Julian 1972, Zhang 2005), which contrasts with the stationary nature of convection found with the retraction mode in Jaffe et al. (2011). The role of this convection in fostering a retraction of the North Pacific jet is not immediately apparent. A separate region of convection in the central and eastern tropical North Pacific is consistent with the OLR composite from Jaffe et al. (2011; specifically their Day 10 composite [their Fig. 12e] and our D+5d; Fig. 3.7f) near the Hawaiian Islands, although twice as intense as that found by Jaffe et al. Convection in this location is consistent with the presence of the low-latitude trough that can be noted in the retraction composites (Fig. 3.4b-d).

Significant tropical convection anomalies are evident in the poleward shift composite (Fig. 3.8a, c, e) over Southeast Asia and the Maritime Continent and are of a larger magnitude than those observed in a similar location in association with the retraction mode. These negative OLR anomalies also appear to remain nearly stationary or move slowly eastward similar to convection associated with the MJO. It is interesting to note that these convective anomalies move eastward at approximately the same speed as the anomalies associated with the retracted jet events (Fig. 3.7b, d, f), roughly 2° per day. The quasi-stationary or slow-moving nature of these convective anomalies enables them to impose persistent forcing on the mid-latitude flow patterns which can impact both the North Pacific jet as well as locations downstream (e.g. Kiladis and Weickmann 1992, Higgins et al. 2000). The broad low-latitude upper-level anomalous ridge in the entrance region of the poleward shift composite (Fig. 3.5a-e) may be a manifestation of upper-level convective outflow in this location that appears to make systematic contributions to the poleward shift of the jet.

Finally, it is worth noting that the large region of anomalously high OLR in the eastern Pacific on the equatorward side of the extended jet's exit region (Fig. 3.7 a, c, e) is coincident with the subsiding branch of the thermally indirect circulation associated with the extended jet. This OLR anomaly intensifies throughout the 10-day composite (Fig. 3.7c, e). Farther north, the rising branch of the thermally indirect circulation likely enhances convection in the region of anomalously low OLR off the west coast of the United States at D0 (Fig. 3.7c).

3.5. Discussion

TE-EOF analysis reveals the details of the synoptic-scale evolutions associated with the leading modes of North Pacific jet stream variability. While the TE-EOF analysis presented here is consistent with the leading modes of variability previously presented by Schubert and Park (1991), Athanasiadis et al. (2010), and Jaffe et al. (2011), the TE-EOF analysis also provides an additional component of temporal coherence to analyses of the large-scale environments characteristic of extremes in the leading modes of variability, and thus points to both upstream precursors and downstream impacts.

The two primary modes of variability presented here consist of 1) the jet in either an extended or retracted state or 2) a poleward or equatorward shift of the jet exit region. While previous studies on North Pacific jet variability focused on the transition into a retracted state (Jaffe et al. 2011) and the instantaneous state of the jet in any given mode (Athanasiadis et al. 2010), the TE-EOF technique identifies the evolution of the two phases of each mode of variability centered on the peak intensity of each phase. By design, the extension/retraction and latitudinal shift modes reach their greatest extents at D0 and so employment of the TE window, which includes some of the growth of the zonal wind anomalies toward (and decay away from) such peaks, reveals new details regarding the corresponding flow evolutions.

Composites constructed based upon high-amplitude events in the TE-PC time series constitute an improvement in the temporal coherence of the associated mid-latitude signals compared to composites constructed with traditional EOFs (e.g. Jaffe et al. 2011). The development of the positive zonal wind anomalies throughout the TE window for the extended jet mode (Fig. 3.3) draws attention to the role of the anomalous trough that intensifies and moves eastward throughout the following 10 days (Figs. 3.3a-e). This trough appears to be central to the development and intensification of the zonal wind anomalies that constitute an extended jet stream, and expanding these composite analyses farther back in time may allow for better identification of such precursor features and their evolution over several days prior to the central time of the TE window. Similar extension of these composite analyses may provide additional insights into the nature of characteristic precursors of high-amplitude events for all four phases of jet variability. The utility of such composite signals is not yet established and merits further examination. However, armed with a physical understanding of the precursors that drive changes in the North Pacific jet, medium-range forecasters may be better able to combine an anticipation of jet variability with the additional knowledge of the associated downstream impacts to improve large-scale forecasts into week two over much of North America.

The composite analyses of extended jets (Fig. 3.3) are, at certain times, consistent with the low-level evolution of the surge phase of the East Asian Winter Monsoon (EAWM; Chang and Lau 1980). For instance, at D-5d of the extended jet composite (Fig. 3.3g), the large area of anomalous low-level cold air over eastern China and the northern South China Sea is in a location consistent with the composite cold surge described by Chang and Lau (1980). Such cold air outbreaks were also identified as a possible precursor to jet extension events by Jaffe et al. (2011) and may play a role in the evolution of extended jets.

Within these composite analyses, consistent high-amplitude impacts were noted downstream over North America in the days after the peak in the respective jet mode. For TE-EOF 1, the jet extension (retraction) mode is associated with a large region of low-level warmth (cold) over much of Alaska and western Canada at D0 (Fig. 3.3h, 3.4h), with temperature anomalies in excess of 4˚C magnitude. These anomalies suggest such weather might be a common downstream impact of each EOF 1 phase. Similarly, the phases of TE-EOF 2 are associated with even stronger downstream impacts over North America, with both poleward and equatorward shift events leading to low-level temperature anomalies in excess of 8˚C. Neither of these anomalies are of high magnitude prior to D-5d (Fig. 3.5g, 3.6f), but rather intensify over North America as the shift of the jet exit region maximizes (at D0). High magnitude temperature anomalies are maintained through D+5d (Fig. 3.5i, 3.6h) and up to an additional five days after the poleward shift (Fig. 3.5j), suggesting that latitudinal shifts of the jet exit region (TE-EOF 2) may affect the downstream weather over North America more significantly than jet extensions or retractions (TE-EOF 1).

Of the four phases associated with the two modes of variability discussed here, slow-moving and potentially organized tropical convection may play a significant role in two of them. A more complete analysis of the mid-latitude and tropical interactions that lead to these variations in the jet would serve to provide additional insight into the forcing behind such patterns, but is beyond the scope of this study and is left for future work. The task of identifying such tropical-extratropical interactions has been partially addressed in cases of recurving TCs interacting with the jet stream (e.g. Archambault et al. 2013), but remains a challenge for less organized episodes of persistent deep convection, a substantially more common phenomenon throughout the tropics and subtropics. The leading modes of jet variability broadly describe the most common evolutions of the North Pacific jet stream, implying a commonplace occurrence such as non-TC convection (e.g. garden-variety as well as MJO- and ENSO-driven) may play a more frequent and significant role in modulating such North Pacific jet variability.

Finally, since the analyses presented here are based upon identification of the dates of *maximum* extension, retraction, and shift, the leading modes identify, for instance, the state of the jet *being extended* rather than the *process of extension*. Thus, the transitions to and from these leading modes, while partially addressed by the lagged composite analysis, merit additional study. Similarities between the jet extension and poleward shift composites (the 850 hPa Gulf of Alaska cyclone and downstream warmth; Figs. 3.3 and 3.5) and the jet retraction and equatorward shift composites (the 850 hPa Gulf of Alaska ridge and downstream cold; Figs. 3.4 and 3.6) suggest that the leading modes, while mathematically independent, are not physically independent. Thus, examination of the nature of transitions between the phases of each mode promises additional insight into the preferred evolutions of the North Pacific jet stream.

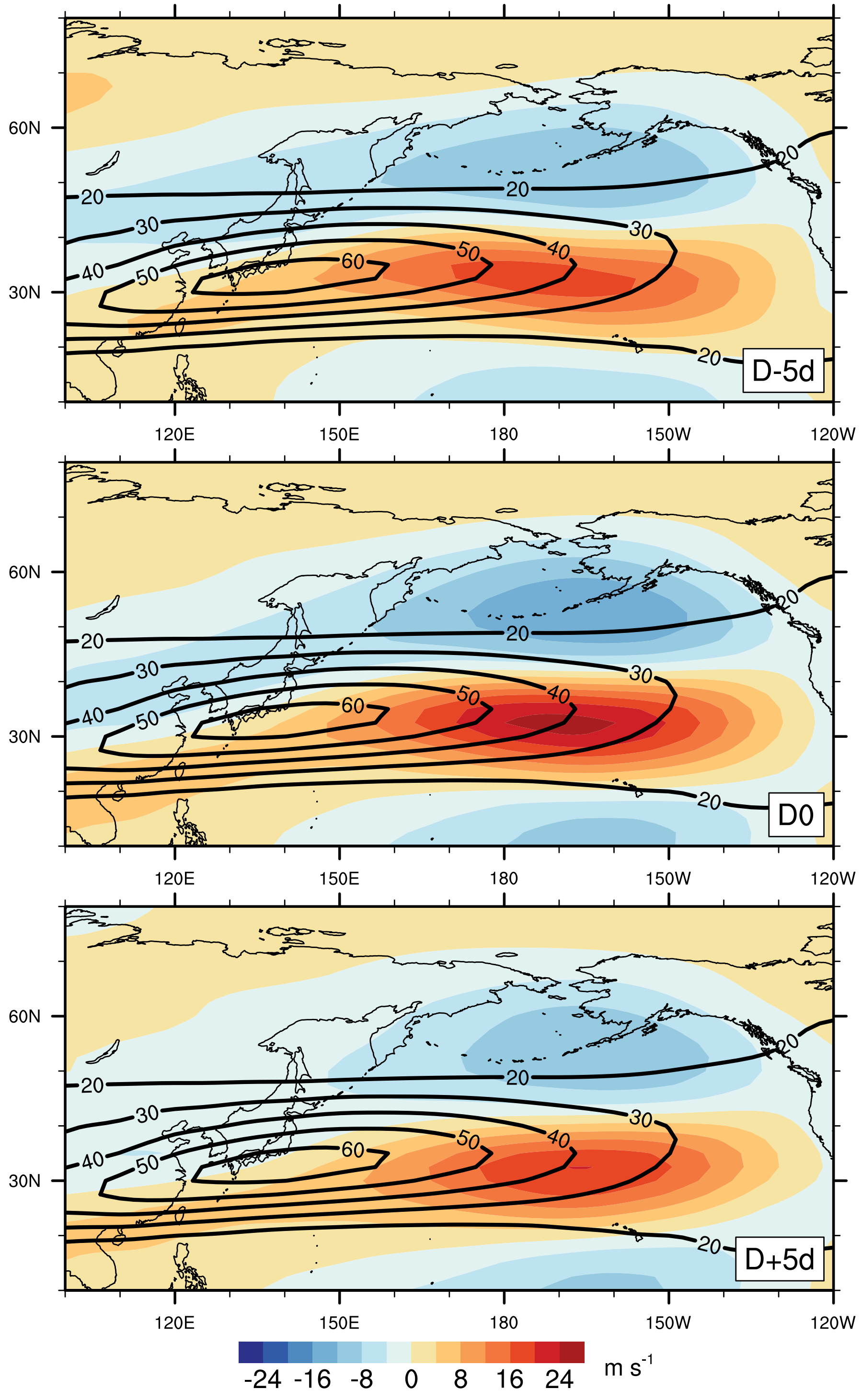

Figure 3.1. TE-EOF 1 (extension/retraction) of the 250 hPa zonal wind over the North Pacific. EOF regressed back onto anomaly data is shaded (m s^{-1}; per color bar). Climatological zonal wind is contoured in black starting at 20 m s^{-1}. Top panel (D-5d) represents the TE-EOF pattern at the beginning of the 10-day TE window; middle panel (D0) represents the pattern halfway through the TE window; bottom panel (D+5d) represents the pattern at the end of the TE window.

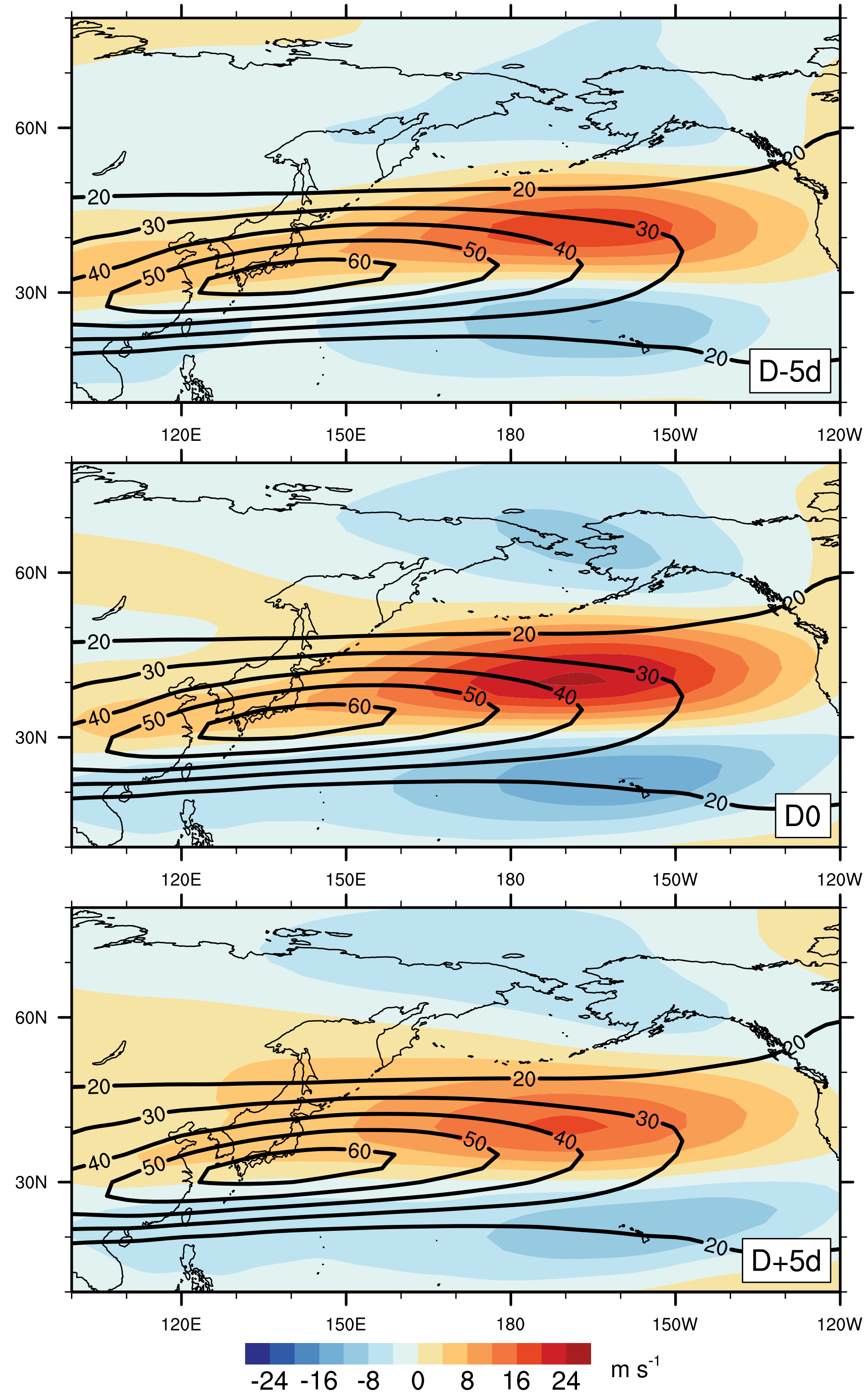

Figure 3.2. As in Fig. 3.1 but for TE-EOF 2 (meridional shift) of the 250 hPa zonal wind over the North Pacific.

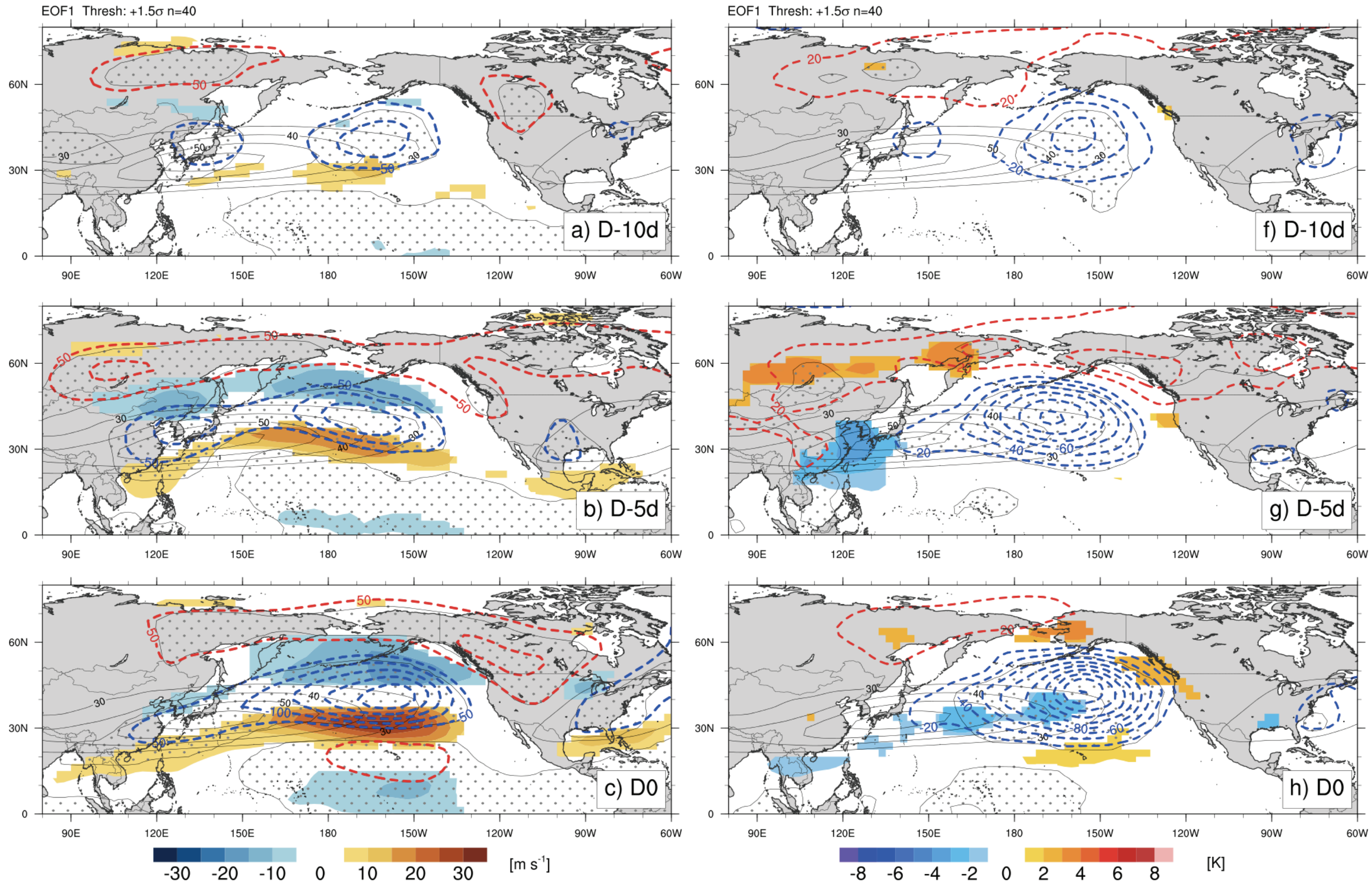

Figure 3.3. Composite of cases where PC of TE-EOF 1 was positive and was greater than 1.5 standard deviations, representing jet extension cases. D0 is defined as the midpoint of the 10-day window, where D-5d (D+5d) is the beginning (end) point. Left plots (a-e) show anomalies of 250 hPa zonal wind (shaded per color bar) and heights (dashed every 50 m). Right plots (f-j) include anomalies of 850 hPa temperature (shaded per color bar) and heights (dashed every 20 m). Both plots show the climatological zonal wind in black contours starting at 30 m s^{-1}. Composite sample size = 40.

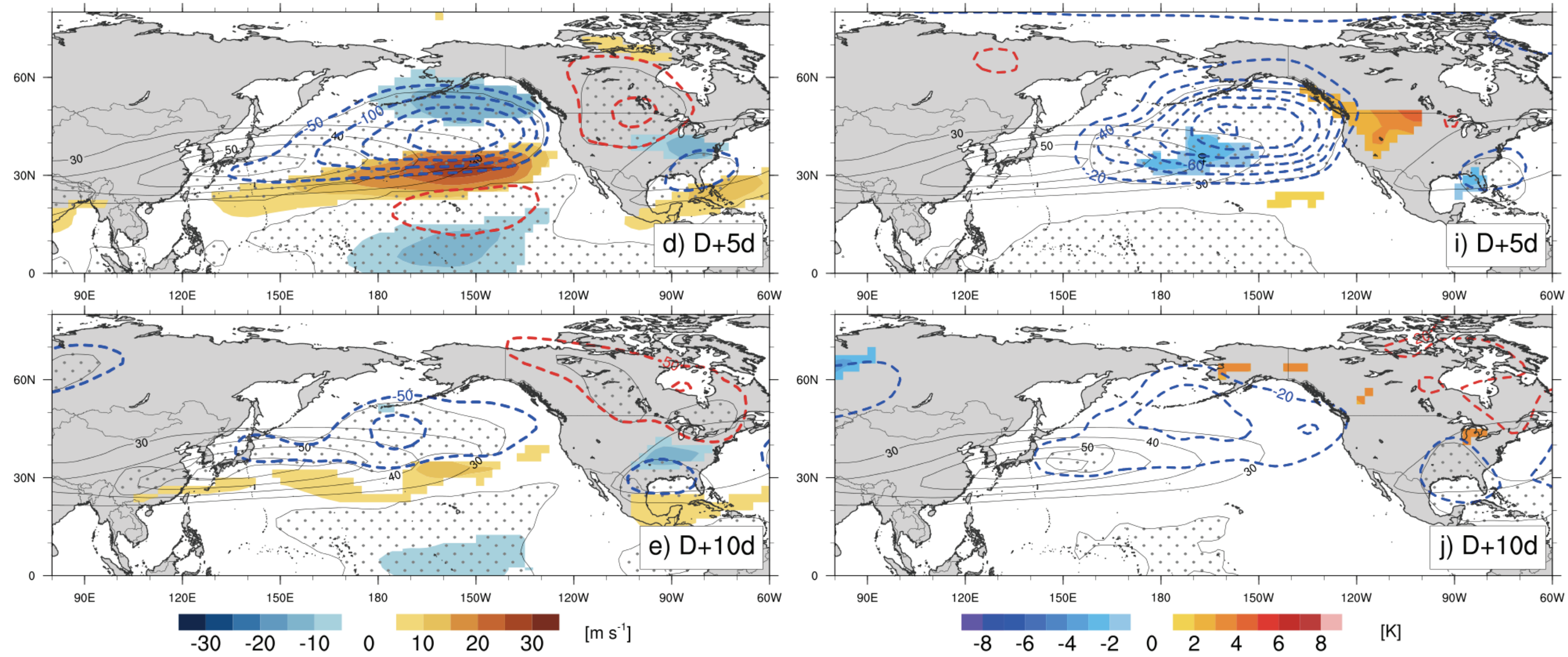

Figure 3.3, continued.

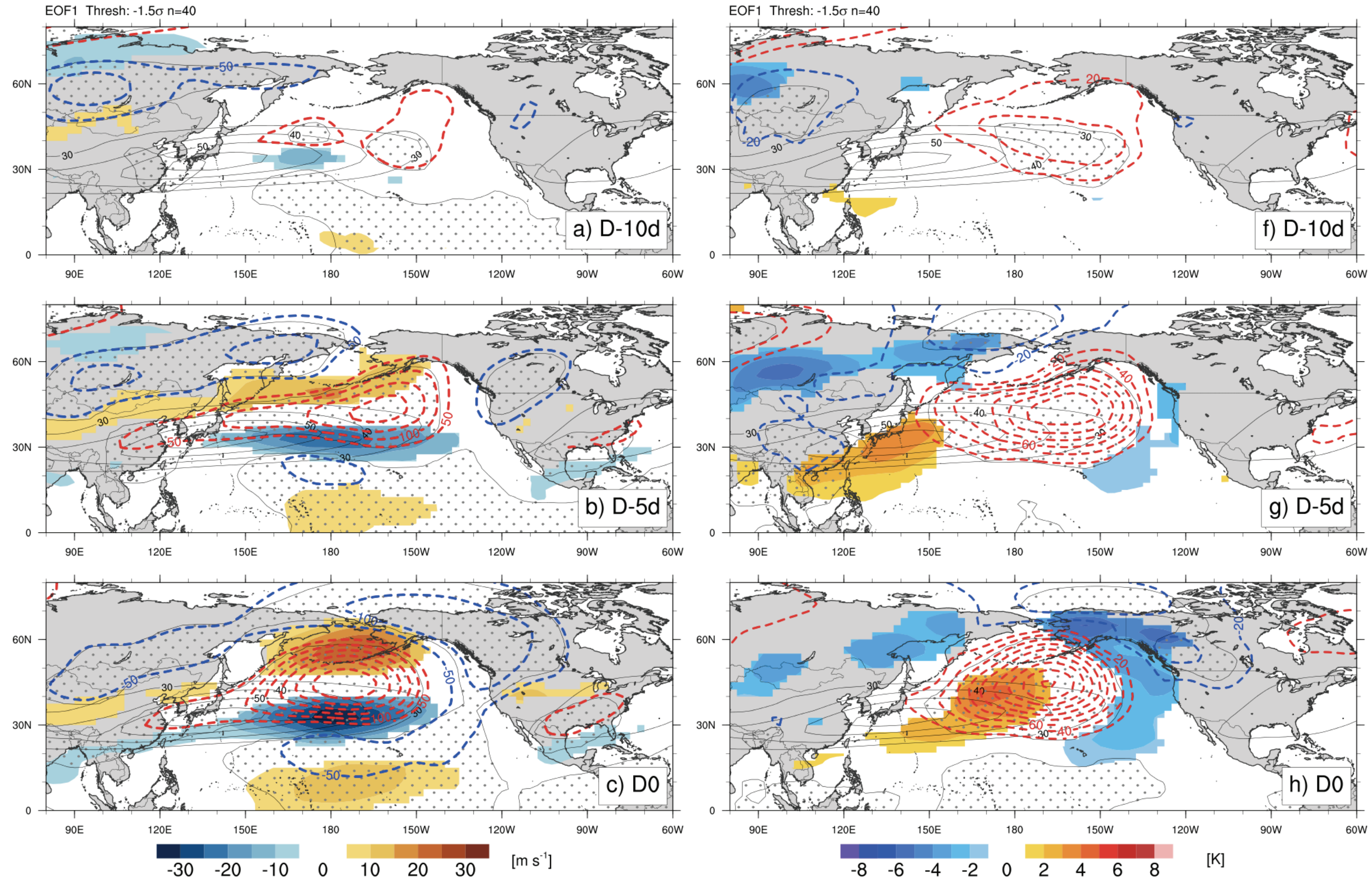

Figure 3.4. As in Fig. 3.3 for cases where the PC of TE-EOF 1 was less than -1.5 standard deviations, representing jet retraction cases. Composite sample size = 40.

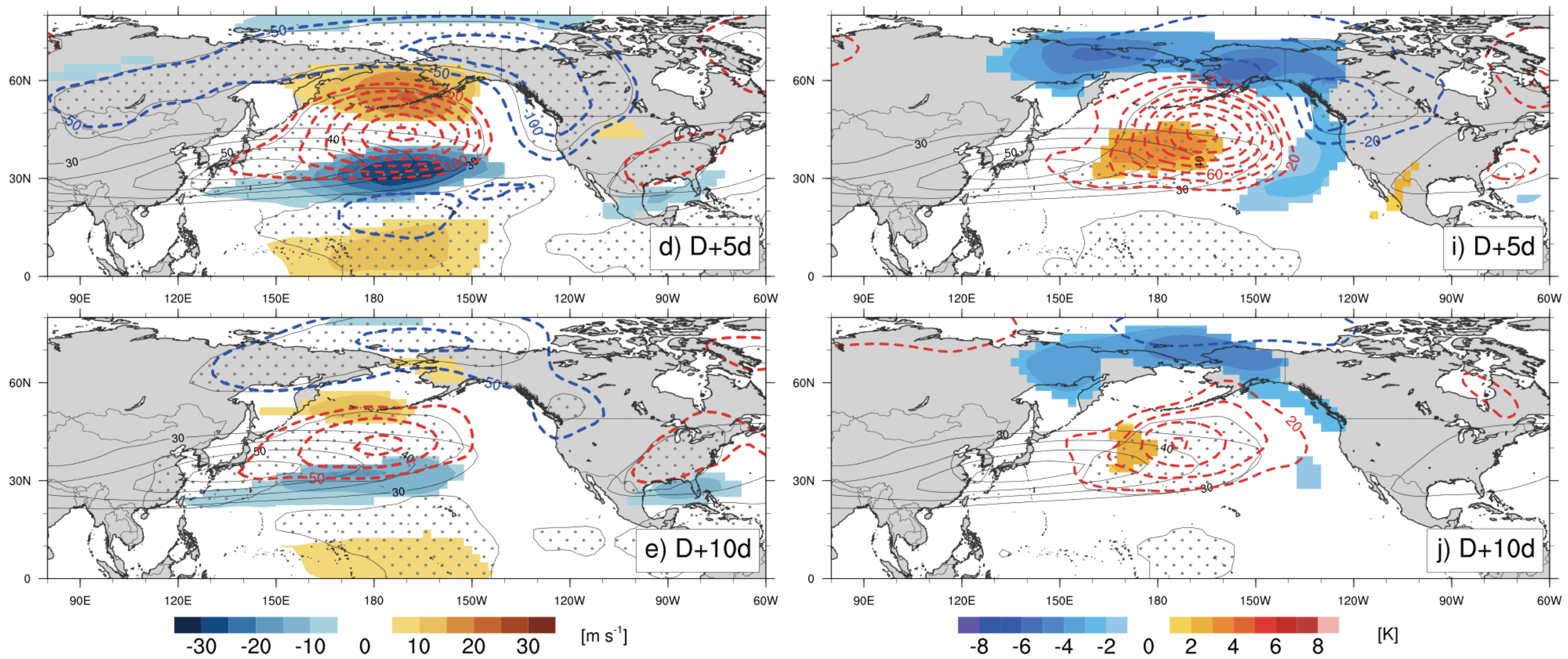

Figure 3.4, continued.

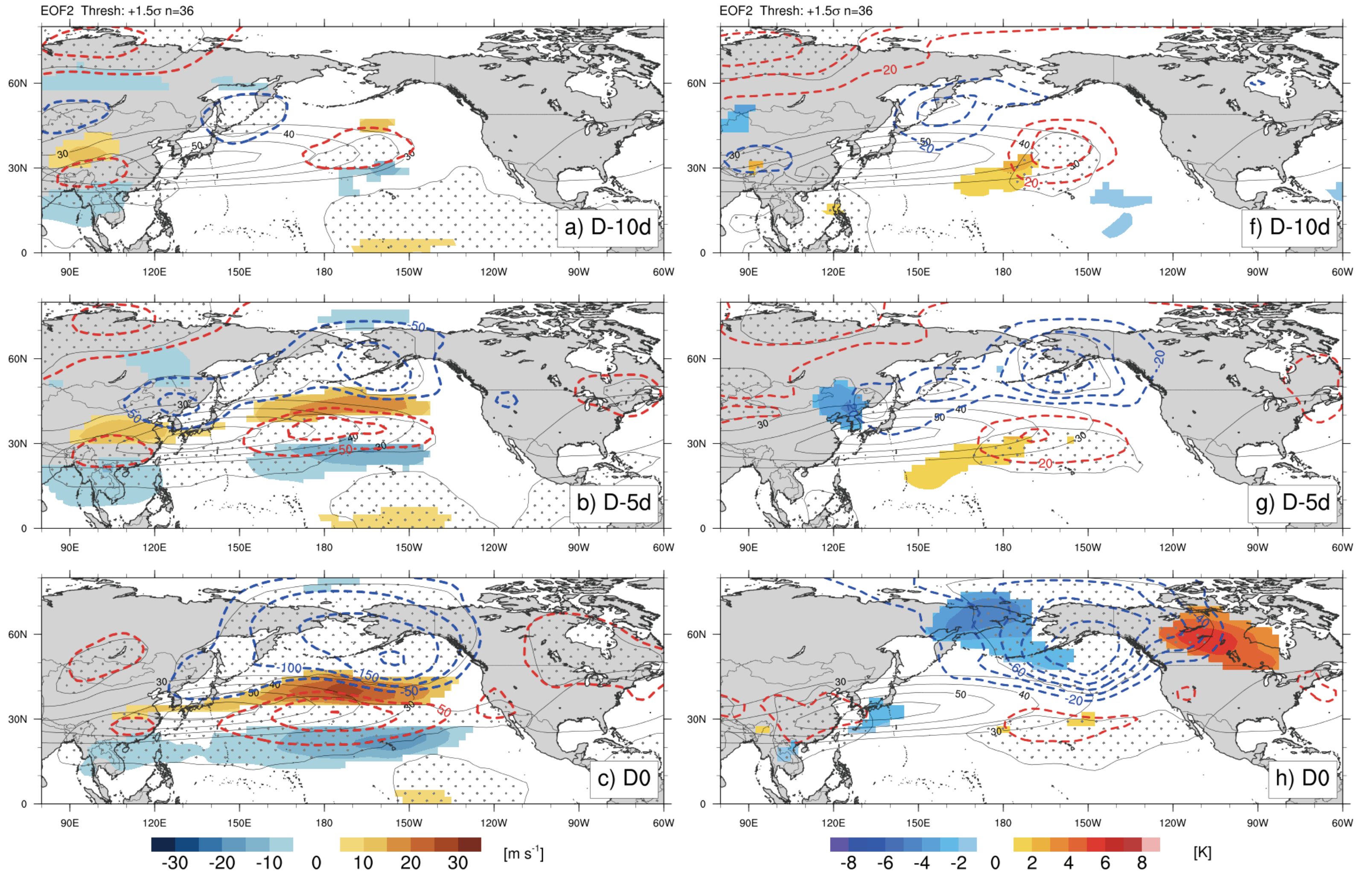

Figure 3.5. As in Fig. 3.3 for cases where the PC of TE-EOF 2 was greater than 1.5 standard deviations, representing poleward shift cases. Composite sample size = 36.

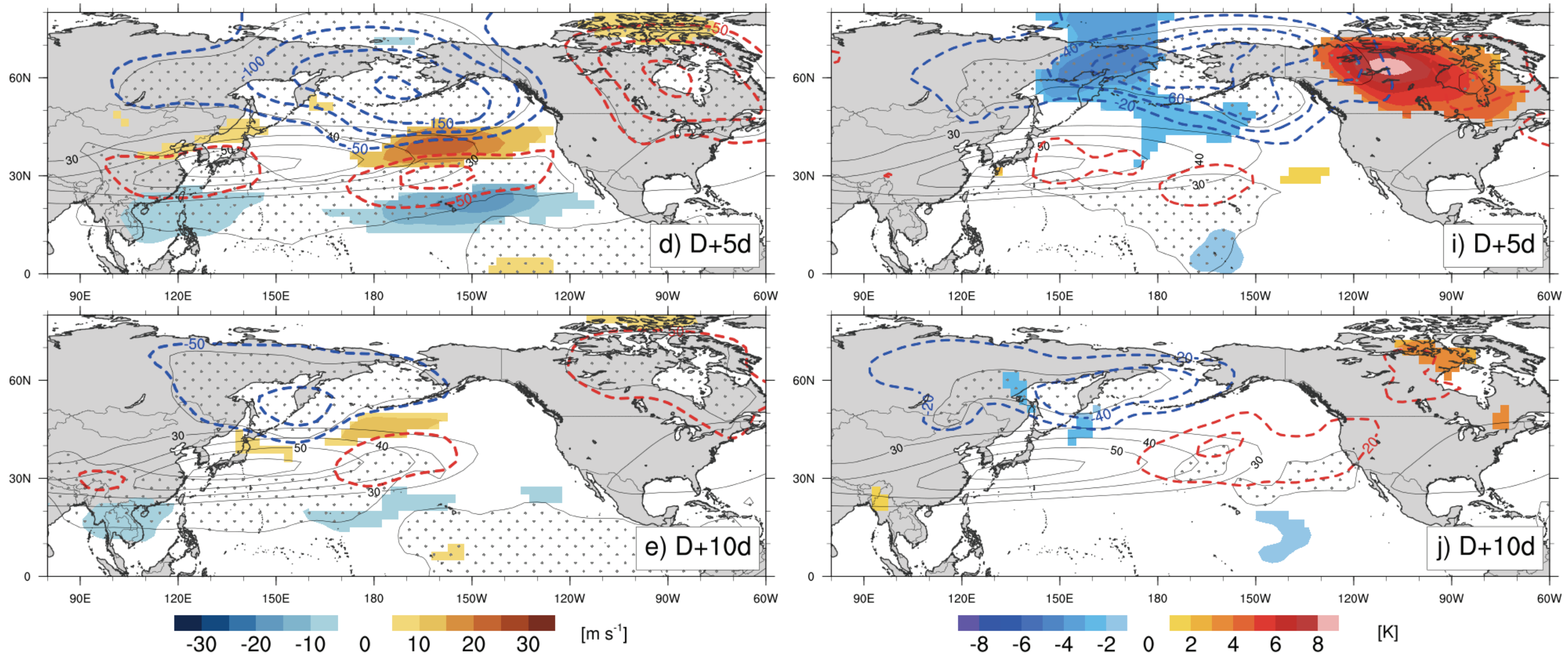

Figure 3.5, continued.

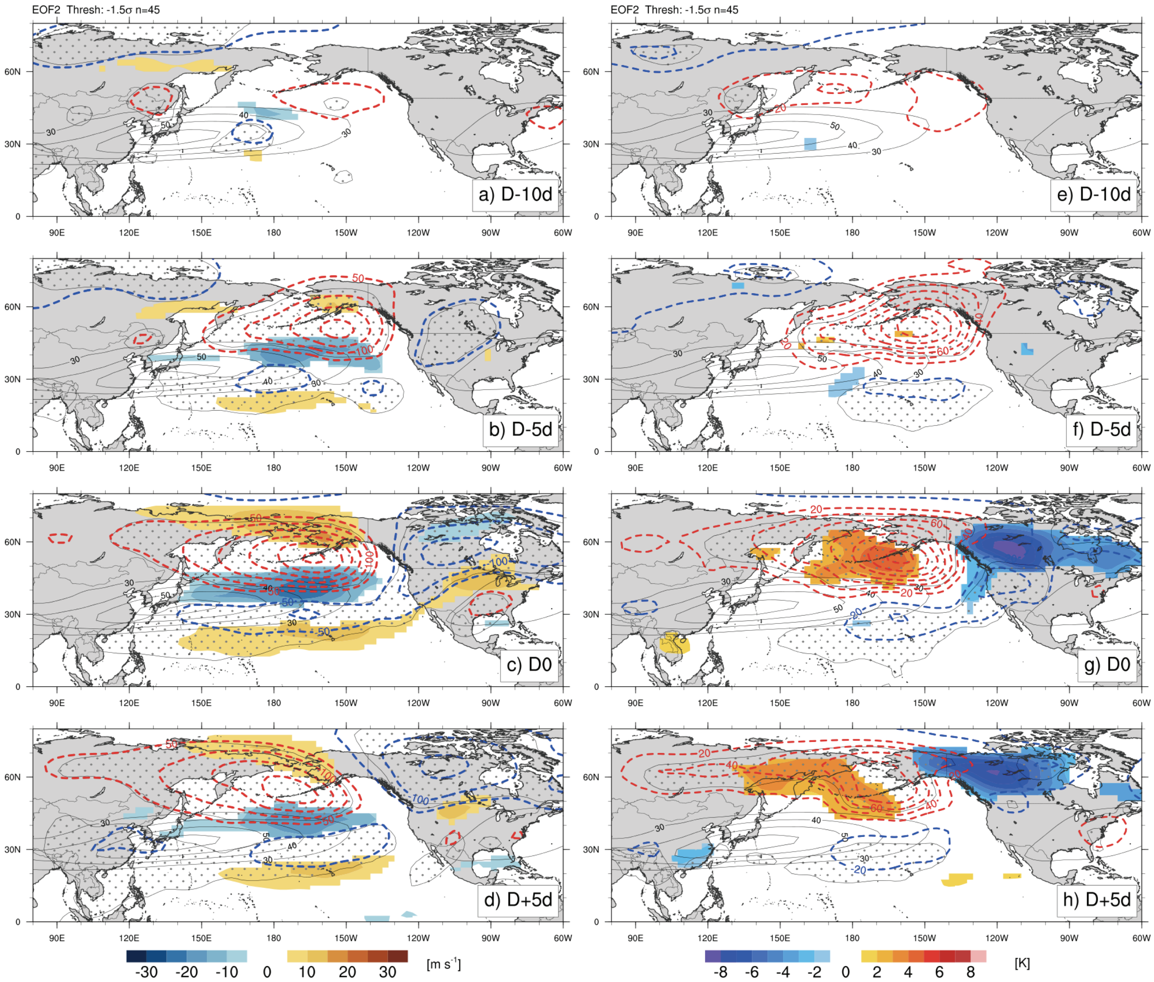

Figure 3.6. As in Fig. 3.3 for cases where the PC of TE-EOF 2 was less than -1.5 standard deviations, representing equatorward shift cases. Composite sample size = 45. Unlike the previous composites, D+10d did not contain anomalies that were both physically meaningful and statistically significant.

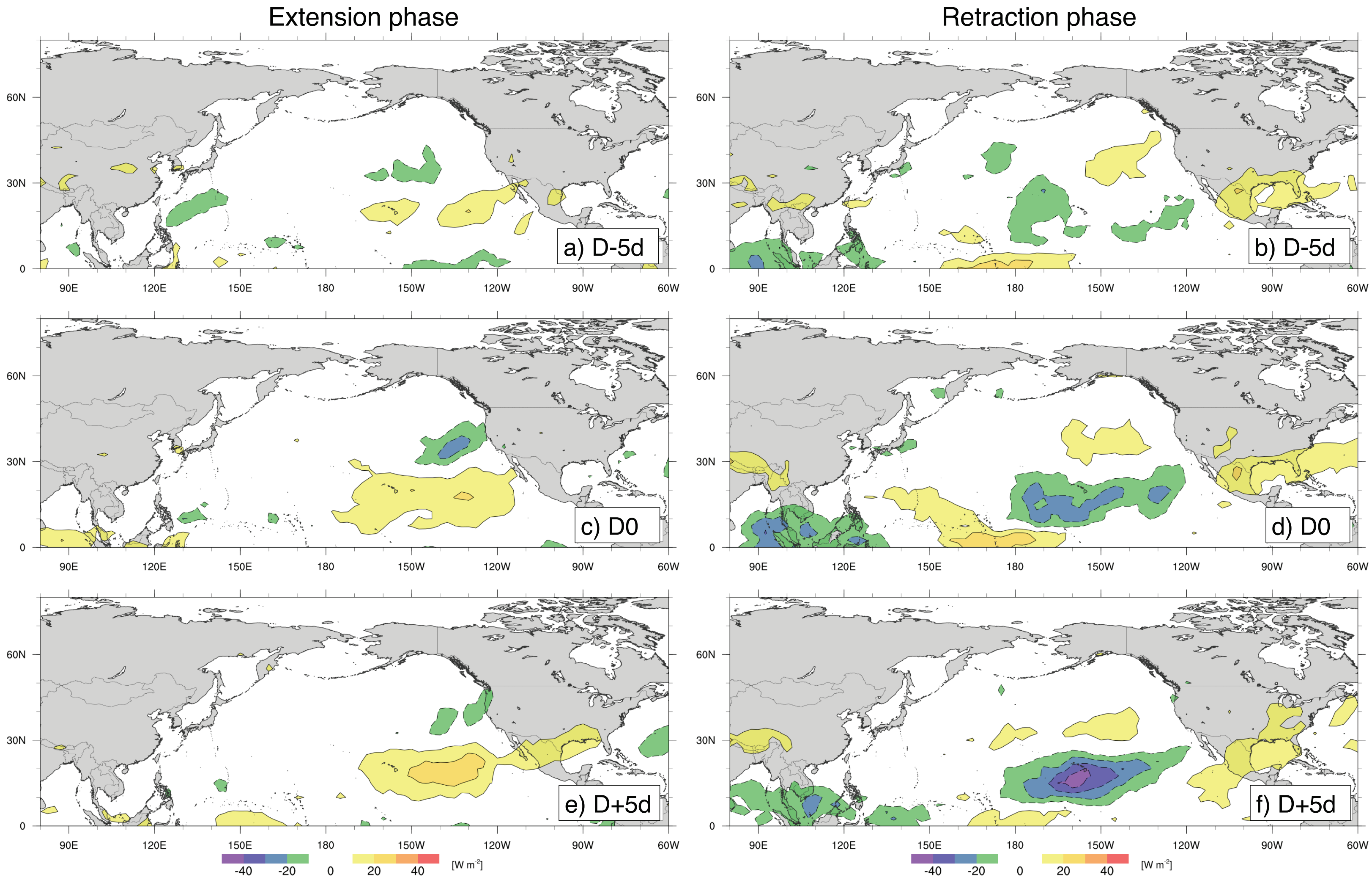

Figure 3.7. Composites of OLR (shaded, per color bar) calculated as in Fig. 3.3 and Fig. 3.4 for jet extension (a, c, e) and jet retraction cases (b, d, f), respectively, from TE-EOF 1. Numbers of cases are consistent with the respective previous composites.

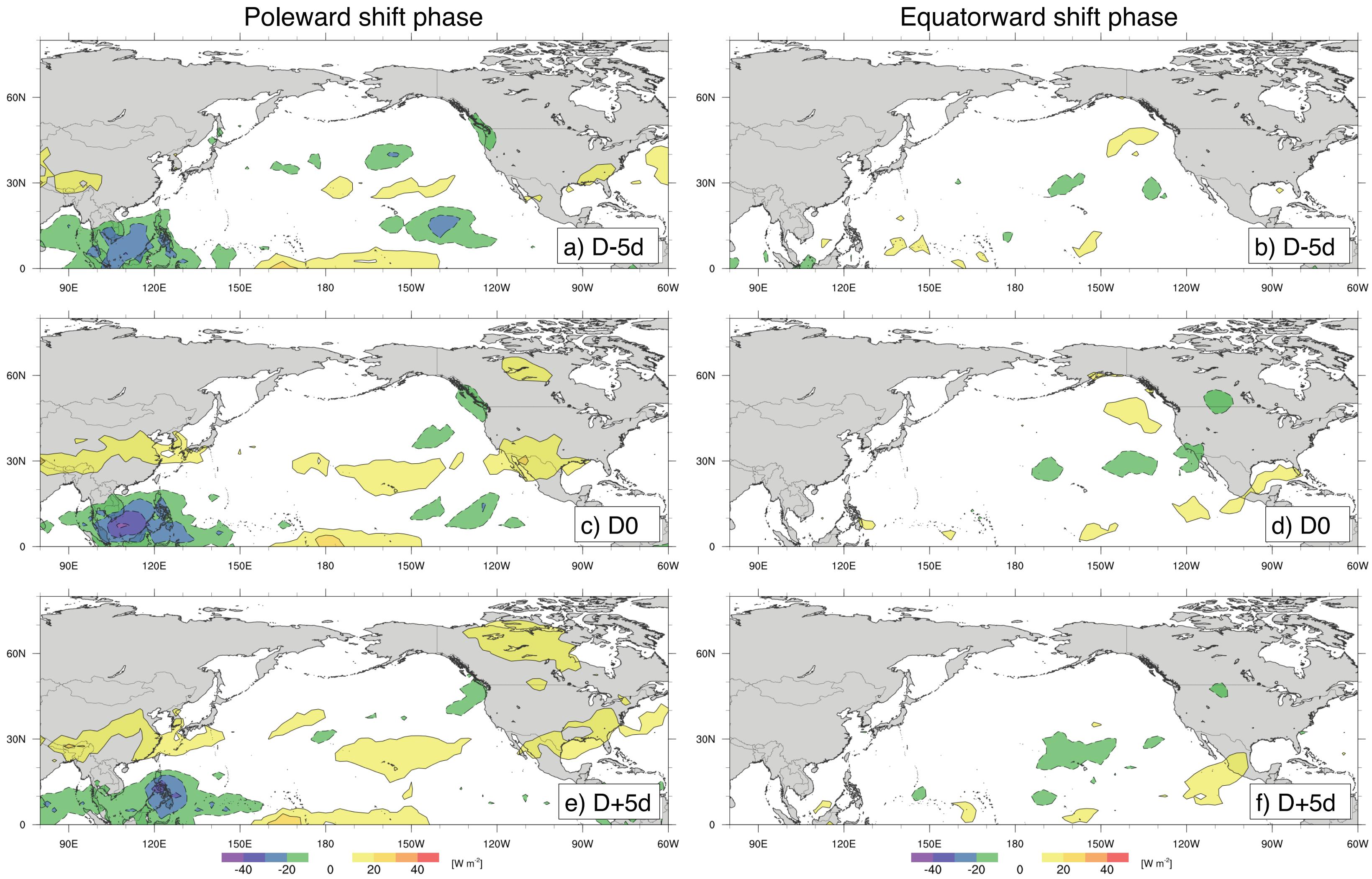

Figure 3.8. As in Fig. 3.7 for poleward shift (from Fig. 3.6; a, c, e) and equatorward shift (Fig. 3.7; b, d, f) jet cases from TE-EOF 2. Numbers of cases are consistent with the respective previous composites.

4. Isentropic pressure depth as a tool for analyzing tropical-extratropical interactions

4.1. Overview

The challenge of identifying and diagnosing interactions between the tropics and extratropics has been recognized for well over 60 years (e.g. Namias and Clapp 1949, Morhi 1953, 1959). The relationship between the tropics and extratropics has been well established via numerous studies (e.g. Gill 1980, Weickmann 1983, Kiladis and Weickmann 1992, 1997), yet little is known about the physical details that characterize such interactions. A subset of tropical-extratropical interactions involve deep convection in close proximity to a jet streak and have been shown to occur via the divergent component of the wind associated with that deep convection acting directly upon the proximate jet streak (e.g. Archambault et al. 2013). However, other interactions may originate from deep convection that is well-removed from a jet streak and thus any interactions must occur via some other process.

The remainder of this chapter is structured as follows. First, a quantity *isentropic pressure depth* is presented that allows for the identification and tracking of a balanced geostrophic response to deep convection. Isentropic pressure depth is compared to the reciprocal of potential vorticity (PV) in Section 4.2. The quantitative aspects and applications of isentropic pressure depth are examined in Section 4.3. An overview of the climatology of isentropic pressure depth in January is provided in Section 4.4. This climatology highlights some curious relationships with the jet stream over the North Pacific, which we also discuss. To demonstrate the practical utility of isentropic pressure depth, Section 4.5 contains a case study of the events leading up to the record-breaking

North American warmth in mid-March 2012. This case study places emphasis on the role of isentropic pressure depth in diagnosing the physical mechanisms driving the key tropical-extratropical interaction that preceded the event. A summary and concluding remarks are presented in Section 4.6.

4.2. Methodology

The "pressure depth" of an isentropic layer serves as a direct measure of the mass contained between the two isentropes that comprise the boundaries of that isentropic layer (Fig. 4.1a). Note also that isentropic pressure depth ($-\frac{\partial p}{\partial \theta}$) is the inverse of static stability ($-\frac{\partial \theta}{\partial p}$) and is, therefore, related to the static stability used by Mohri (1959) to track the poleward motion of tropical upper tropospheric air masses (measured as $\frac{\partial T}{\partial p}$ in that study). Thus, a local maximum (minimum) in pressure depth in a given isentropic layer represents a local maximum (minimum) in mass and a local minimum (maximum) in static stability in that layer compared to its surroundings.

Of course, atmospheric processes are not constrained to be adiabatic, and diabatic processes impact the utility and interpretations of isentropic pressure depth. In the upper troposphere, radiative cooling to space, a process known to occur at a rate of ~1-2 K per day (given a cloud-free troposphere – the cooling is often stronger in the presence of clouds), can reduce the potential temperature of a parcel. Secondly, moist convection, in which a lifted parcel may experience an increase in its potential temperature as a result of latent heat release, can render a parcel's potential temperature much higher in the upper troposphere than it originally was in the boundary layer. Moist adiabatically, the parcel's equivalent potential temperature (θ_e) at the start of its ascent will be roughly equal to its potential temperature (θ) at the level where it becomes neutrally buoyant. This implies that the upward mass flux associated with deep convection rooted in an environment with boundary layer equivalent potential temperatures θ_{eBL} will be exhausted in the upper troposphere at an isentropic level where $\theta \approx \theta_{eBL}$ (Fig. 4.1b). The relationship between the boundary layer environment and the level of upper tropospheric exhaust holds for deep convection at both tropical and middle latitudes.

Horizontal ivergence in an isentropic layer discourages conservation of the pressure depth in a given column by redistributing mass within the isentropic layer. When considering PV, changes in the vorticity compensate any changes in static stability ($-\frac{\partial\theta}{\partial p}$, the inverse of isentropic pressure depth) caused by divergence within the isentropic layer. The conservative nature of PV suggests that the PV could be better suited to tracking the migration of the tropical convective exhaust involved in tropical-extratropical interactions despite the fact that the relatively low vorticity and low stability characteristic of tropical latitudes render the variability of tropical tropospheric PV very small. Magnusdottir and Schubert (1990) considered a related variable, termed 'potential pseudo density', that is a construction of the reciprocal of PV (RPV) in a three-dimensional semi-geostrophic coordinate system. Here we have chosen to make a comparison to RPV in isentropic coordinates (Fig. 4.2). The visual similarity between the spatial distribution of the pressure depth contours (Fig. 4.2a) and RPV contours (Fig. 4.2b) is striking. Differences between the two appear largest in regions of strong cyclonic vorticity, such as the trough east of the Lesser Antilles (marked as T), as well as regions of pronounced outflow from the tropics, such as the plume of large pressure depths over the Yucatan and east of Florida that extends from TC Raymond (2013; marked as TC). In general, RPV has weaknesses related to the reduced variability in PV at low latitudes, in that the vorticity term leads to noisy RPV as the slight variations of vorticity over fine spatial scales dominate the variability in the static stability term. While Fig. 4.2 compares only a single analysis time, additional comparisons have been made across other cases and provided similar results (not shown). Thus, we believe that isentropic pressure depth provides a useful representation of the aggregate convective mass flux, especially in the tropics.

It is straightforward to calculate the isentropic pressure depths in a gridded reanalysis data set. For each grid point, the pressure depth, Δp, in an isentropic layer is given by $p_{\theta 1} - p_{\theta 2} = \Delta p$, where $\theta_1 < \theta_2$. Given the monotonically increasing vertical distribution of potential temperature, this formulation will always yield a positive value. The gridded reanalysis data is interpolated onto isentropic levels every 5 K from 300 K - 380 K to facilitate these calculations.

Isentropic pressure depths were calculated with the Climate Forecast System Reanalysis (CFSR; Saha et al. 2010), chosen for its high vertical resolution (64 model levels; 37 output pressure levels) as well its small horizontal grid spacing (0.5°). Pressure depth values were calculated for each 5 K isentropic layer (300 - 380 K) at each grid point for each six-hourly time over the entire CFSR dataset (1979-2010). From this data, it is possible to construct a climatology of pressure depths across the entire range of isentropic layers spanning the full 32 years of CFSR data. Climatological means are calculated individually at each six-hourly time over all 32 years.

To complement the climatological mean, calculations of the standard deviation were performed in order to standardize the departures from climatology in the ensuing analysis.

It was quickly determined that the frequency and distribution of such departures was not distributed normally. Thus, in order to derive a measure of standardized pressure depth anomalies, we devised a statistical measure we term the *standard departure*. The standard departure is intended to mimic the standard deviation by providing separate values for positive and negative anomalies within a given distribution, thus correcting for asymmetries in the distribution about zero. Calculation of the negative standard departure at a single grid point and time follows three steps:

1) Take a list of all pressure depth anomaly values during the climatology period (one value for each year; Fig. 4.3a) and remove non-negative anomalies from the list (Fig. 4.3b)

2) Multiply the negative anomaly values by -1 and add the resulting positive value to the list of anomalies. This doubles the size of the distribution and makes the distribution of values symmetric about zero (Fig. 4.3c).

3) Take the standard deviation of this list; this value is the *negative standard departure*.

The above process can be duplicated for the positive anomalies as well, producing a *positive standard departure* and a *negative standard departure* at each grid point and time. Pressure depth anomalies are standardized by taking positive (negative) anomalies and dividing by the positive (negative) standard departures. The resulting values, now in terms of standard departure units, can be interpreted in a manner comparable to standardized anomalies calculated with a standard deviation. These standard departures facilitate a clear and balanced comparison of positive and negative anomalies in asymmetric distributions. Standard departures can also be used to investigate the variance of the separate populations of positive and negative pressure depth anomalies, an analysis that is not possible with a traditional variance calculation. Analyses utilizing standard departures are presented in Section 4.

4.3. Applications of isentropic pressure depth

Quantitative insight can be gained from the pressure depth analyses because pressure depth relates to the thermal wind relationship in isentropic coordinates. The geostrophic wind can be written as

$$\vec{\boldsymbol{V}}_g = \frac{\vec{k}}{f} \times \nabla M$$

where M is the Montgomery streamfunction ($M = c_pT + \Phi$). Taking the vertical derivative of the geostrophic wind in isentropic coordinates gives

$$\frac{\partial \vec{\boldsymbol{V}}_g}{\partial \theta} = \frac{\vec{k}}{f} \times \nabla \frac{\partial M}{\partial \theta}.$$

Since the vertical derivative of the Montgomery streamfunction is given by

$$\frac{\partial M}{\partial \theta} = \frac{c_p T}{\theta} = c_p (\frac{p}{p_0})^{\kappa},$$

this yields a version of the isentropic thermal wind relationship,

$$\frac{\partial \vec{\boldsymbol{V}}_g}{\partial \theta} = \frac{1}{\rho f \theta}(\vec{k} \times \nabla_\theta p) \tag{1}$$

which demonstrates that the vertical shear of the geostrophic wind in an isentropic layer depends on the gradient of pressure depth in that layer. Thus, when proximate to an upper level jet streak, a large pressure depth gradient is directly responsible for some portion of the geostrophic wind speed observed within that jet streak.

According to equation (1), a broad region of positive pressure depth anomalies in a given layer is associated with an anomalous anticyclonic geostrophic vertical shear in that same layer (Fig. 4.4a). When this anomalous vertical shear is proximate to a jet streak, the shear is associated with an increase the maximum wind speeds in that jet (Fig. 4.4a). When a positive pressure depth anomaly increases in magnitude due to the flux of mass into the isentropic layer (e.g. Fig. 4.1b), the resultant increase in isentropic pressure depth directly intensifies the pressure depth gradient, resulting in an additional increase in the geostrophic vertical shear and further strengthening of a jet streak (Fig. 4.4b). Thus a physically appealing explanation of the effect of aggregate deep convection on jet streak intensity emerges. Increases in isentropic pressure depth can result from the mass flux associated with deep convection. Such increases then enhance the geostrophic vertical wind shear on the poleward side of the positive pressure depth anomaly, which contributes to strengthening the jet streak.

An important aspect of the analysis of positive pressure depth anomalies is identifying the origin of the mass inflating an isentropic layer. Moist adiabatic ascent driven by deep convection, as described in Section 4.2, likely serves as a primary source of mass for such inflation. Evidence for this suggestion lies in the relationship between climatological means of low-level θ_e (Fig. 4.5a, c) and the layer of maximum isentropic pressure depth (in 5 K layers between 320 - 380 K; Fig. 4.5b, d). The correspondence between the mean 1000 hPa θ_e and the lower isentropic bound of the climatologically thickest 5 K layer is compelling, especially over the oceans, in both January (Fig. 4.5a-b) and July (Fig. 4.5c-d). This correspondence suggests that moist adiabatic ascent in the tropics is a primary means of inflating upper tropospheric isentropic layers.

Once inflated, regions of large isentropic pressure depth often remain coherent structures for several days and are readily traceable as anomalies from a long-term climatology (not shown). As a result, coherent pressure depth anomalies can be traced visually as they move away from the original source(s) of their inflation. Thus, despite the fact that isentropic pressure depth is not a conserved quantity, the anomalous circulation associated with an individual anomalous pressure depth feature, as well as its impact on the mid-latitude circulation, can quite often be traced back to its origin.

4.4. Climatological aspects of isentropic pressure depths

As mentioned in the previous section, isentropic pressure depths can be tracked over extended periods of time as anomalies from a long-term climatology. A climatology of isentropic pressure depths for the month of January is presented in Fig. 4.6 for isentropic layers where mid-latitude convection and tropical convection commonly exhaust mass (315-330K and 340-355 K, respectively; Fig. 4.6a, Fig. 4.6b). In general, the 315-330 K climatology for the month of January (Fig. 4.6a) highlights pressure depth maxima associated with subtropical ridges between 20°-30° latitude (e.g. Rodwell and Hoskins 2001) as well as a narrow strip of large pressure depth gradient located between 30-50° latitude in each hemisphere. The tightest pressure depth gradients in the Northern Hemisphere can be noted over the western Pacific and western Atlantic, corresponding well with the locations of the climatologically strongest jet streams. In Fig. 4.6a, a single climatological contour of pressure depth (120 hPa) is commonly found near the latitudes where the magnitude of the isentropic pressure depth gradient, and therefore the vertical geostrophic wind shear in the layer, is the largest. This particular pressure depth contour therefore serves as a reasonable proxy for the position of the mid-latitude jet stream. The January climatological pressure depth maxima in the 340-355 K layer (Fig. 4.6b) are located in regions where deep convection is frequently observed, including over the warm sea surface temperatures of the western Pacific warm pool and the Amazon basin of South America. Pressure depths are also generally higher in the climatological means of both isentropic layers over regions of strong heating or elevated terrain, such as southern Africa, western Australia, and the Andes of South America (Fig. 4.6a, b).

Statistically, local maxima in the variance (calculated as the square of the standard deviation at each grid point and time) of the isentropic pressure depth anomalies highlight regions where the pressure depth varies, on average, the most over a given period of time. In a similar manner, local maxima of the positive (negative) standard departure highlight regions where the pressure depth varies, on average, the most in the positive (negative) direction. Maps of the mean January positive (Fig. 4.6c) and negative (Fig. 4.6d) standard departures in the 315-330 K isentropic layer provide insight into where pressure depth anomalies are, on average, the most positive or negative. In general, the largest positive standard departures of isentropic pressure depth are located along and north of the climatological 120 hPa contour (Fig. 4.6c) while the largest negative standard departures are along and south of the climatological 120 hPa contour (Fig. 4.6d). For both positive and negative standard departures, the regions of the largest standard departures are located between 180° and 90°W. This is the same area where the leading modes of variability of the upper level jet stream are present over the North Pacific (e.g. Athanasiadis et al. 2010, Jaffe et al. 2011, and as presented in Chapter 3). Given that the 120 hPa contour serves as a good proxy for the axis of the jet stream in the 315-330 K isentropic layer, it seems reasonable that the distribution of the standard departures of the isentropic pressure depths may inform new understanding of the leading modes of North Pacific jet variability.

To examine the implications of the observed distribution of positive standard departures of isentropic pressure depth, consider the imposition of a positive pressure depth anomaly (such as in the schematic from Fig. 4.4c) on the January mean 315-330 K isentropic pressure depth climatology (Fig. 4.6a) near the largest mean January positive standard departure (around 40°N, 170°W, Fig. 4.6c). The anomalous anticyclonic vertical geostrophic wind shear around this positive pressure depth anomaly would produce increased westerly winds along its northern flank and decreased westerly winds along is southern flank (Fig. 4.7a), resulting in a poleward reconfiguration of the exit region of the jet stream (dashed line in Fig. 4.7a). The hypothetical reconfiguration is reminiscent of the poleward shifted jet, the positive phase of the second leading mode of variability identified by Athanasiadis et al. (2010) and in Chapter 3. Given that positive pressure depth anomalies are primarily inflated by exhaust from deep convection, the suggestion is that poleward shifted jet exit region events can be tied back to that deep convection.

A similar thought experiment can be performed regarding the distribution of negative standard departures of isentropic pressure depth. Given the broad maximum of mean January negative standard departures near 35°N 135°W (Fig. 4.7b), envision a negative pressure depth anomaly imposed in that location. The anomalous cyclonic vertical geostrophic wind shear around the negative pressure depth anomaly decreases westerly winds on its northern flank (near the climatological mean 120 hPa 315-330 K pressure depth contour/proxy jet axis) and increases westerly winds along its southern flank. The resulting enhancement of the westerly flow on the southern flank of the pressure depth anomaly reorients the mean southwesterly flow to a westerly direction, resulting in the zonal extension of the climatological jet stream (Fig. 4.7b). While the dynamics of negative pressure depth anomalies have not been a focus of our descriptions thus far, we can say that the increased static stability associated with smaller values of isentropic pressure depth is likely the signature of the presence of a positive PV anomaly of mid-latitude origin. Consistent with this suggestion of an extratropical forcing for jet extension, Handlos and Martin (2016) report that some portion of jet extension events appear to relate to extratropical troughs near the jet axis. Both of these general analyses of climatological variance suggest additional investigation into the relationship between the leading modes of North Pacific jet variability and isentropic pressure depths may yield insightful results. Such an investigation is presented in greater detail in Chapter 5.

4.5. Case study - March 2012

In order to demonstrate the utility of pressure depth analyses, we present a case study of a sequence of unusual weather events from the first three weeks of March 2012 from the pressure depth perspective. March 2012 was characterized by unprecedented anomalous warmth over much of central and eastern North America, with surface temperature anomalies exceeding 15°C across parts of the Great Lakes region in mid-March (Dole et al. 2014). Two to three weeks earlier, intense tropical convection was occurring over the equatorial Indian and West Pacific Oceans in association with a high-amplitude MJO event. By calculating the mid-latitude response to idealized tropical heating anomalies similar to the observed convection in a linear model, Dole et al. (2014) showed that the deep convection associated with this strong MJO event was, in part, responsible for the subsequent anomalous warmth over North America. The response provided by the model was strikingly similar to the observed 300 hPa height anomalies over the North Pacific and North America during mid-March (not shown, Figure 6 in Dole et al. 2014). While idealized tropical heating anomalies have previously been shown to force Rossby wave trains (e.g. Hoskins and Karoly 1981, Kiladis and Weickmann 1992, 1997), an alternative physical description of the interaction provides additional insight into the role of other synoptic-scale systems in creating this exceptionally unusual event. We present a description of the evolution of events leading to the anomalous North American warmth using isentropic pressure depth to identify regions of inflated and deflated isentropic layers and their associated anticyclonic and cyclonic circulation anomalies. We aim to show the utility of this diagnostic in promoting better understanding of the physical details of tropical-extratropical interactions.

4.5.1. Interaction between tropical convection and the East Asian jet stream

A strong MJO event occurred in March 2012, with a peak amplitude of 2.77 on 3 March per the Realtime MJO Monitoring (RMM) index (Wheeler and Hendon 2004). This event was associated with anomalous OLR in excess of -50 W m^{-2} over portions of Indian Ocean and the adjacent maritime continent (near 90°E, 26 February - 9 March) as it slowly progressed eastward (Fig. 4.8). This widespread convection supports an environment in which the 340-355 K isentropic layer is anomalously deep, with pressure depth anomalies in 30-45 hPa range at 0000 UTC 3 March over much of the maritime continent region (Fig. 4.9a). By 1200 UTC 5 March, anomalies in that region had continued to increase, commonly exceeding 45-60 hPa (Fig. 4.9b). An expansion of the anomalies is most notable over southeast Asia, where the inflated 340-355 K layer extends poleward of 20˚N and borders the jet stream in that isentropic layer. A gradient of anomalous pressure depth is found along and immediately equatorward of the highest wind speeds, with the gradient over southern China along 100˚E reaching as much as 90 hPa across only ~280 km. This gradient intensifies further by 0000 UTC 8 March (Fig. 4.9c), supporting the high layer-mean wind speeds within the 340-355 K layer (90 m s^{-1}).

Subsequently, this region of anomalously large pressure depths in the 340-355 K layer begins to move eastward in concert with the jet core over central China and extends east of Japan by 1200 UTC 10 March (Fig. 4.9d). The eastward progression of the region of large pressure depth anomaly continues through 0000 UTC 12 March, where the anomaly can be seen centered well east of Japan (near 160˚E; Fig. 4.11b). From 10 March (Fig. 4.9d) through 12 March (Fig. 4.11b), the exit region of the jet stream in the 340-355 K layer shifts eastward roughly 30˚ (~2600 km) while remaining on the poleward flank of the positive pressure depth anomaly. A backward trajectory analysis of the parcels within the center of the region of anomalously large pressure depths at 1200 UTC 10 March reveals the parcels originated four or more days earlier in the lower to middle troposphere near the equator (Fig. 4.10). Nearly all parcels traced in this backward trajectory analysis experience significant nonconservation of potential temperature, indicating diabatic processes, frequently associated with deep convection, at work. Although the timing varies, most parcels undergo ascent between 1200 UTC 3 March (the beginning of the trajectory analysis) and 0000 UTC 7 March, a period during which the air parcels were within the envelope of the ongoing MJO event (Fig. 4.8, Fig. 4.10). The regionally widespread and persistent nature of convection within the MJO envelope (e.g. Zhang 2005) supports the prolonged nature of the ascent noted for some of the parcels in the trajectory matrix (Fig. 4.10).

4.5.2. Transition from tropically-driven to extratropically-driven evolution

The eastward extension of the jet stream over the western North Pacific facilitates a rapid cyclogenesis event east of Kamchatka by 0000 UTC 12 March. Supported by upward vertical motion in the poleward exit region of this extending jet stream, this cyclone's central pressure falls to ~960 hPa (Fig. 4.11b) while developing its own intense vertical motions associated with strong baroclinic zones (not shown). These vertical motions lead to the ascent and exhaust of additional mass in the 315-330 K layer (Fig. 4.11a), made manifest as a positive pressure depth anomaly immediately downstream of the cyclone in conjunction with an amplifying ridge. This 315-330 K positive pressure depth anomaly contributes to the intensification of the jet streak to its north over the Bering Sea and Gulf of Alaska. In turn, the Sawyer-Eliassen circulation associated with the entrance region of this jet stream supports the further development of the deep cyclone east of Kamchatka and additional inflation of isentropic layers within, or vertically proximate to, the 315-330 K layer.

This region of positive pressure depth anomalies slides to the southeast before moving eastward over the next several days and merging with another region of positive pressure depth anomalies (not shown). The amalgamated anomaly becomes centered over the western United States by 0000 UTC 16 March (Fig. 4.12a) and continues over eastern North America in subsequent days (Fig. 4.12b, c).

The significance of the evolution surrounding the cyclone east of Kamchatka cannot be overstated. The intense cyclone is originally forced by the circulation associated with the exit region of the extending Asian jet stream, whose intensity and extension are both driven in part by the anomalous mass in the 340-355 K isentropic layer immediately on the equatorward flank of the jet. As vertical motion with the cyclone intensifies, the mass flux from convection in the cloud head of the cyclone exhausts into the 315-330 K layer and becomes the impetus for an increasingly large positive pressure depth anomaly in the mid-latitudes. Continued intensification of the associated pressure depth gradient intensifies the associated jet on the north side of the pressure depth anomaly and sets the stage for the new 315-330 K pressure depth anomaly to potentially impact the downstream mid-latitude pattern.

4.5.3. Development of a pressure depth anomaly from frontal convection

Upstream from the events associated with the cyclone near Kamchatka, a developing frontal wave can be seen in infrared satellite imagery ahead of a trough and negative 315-330 K pressure depth anomaly near 170˚E at 0000 UTC 16 March (Fig. 4.12a). Emanating eastward from the expanding cloud shield, a region of positive pressure depth anomalies (maximized at >60 hPa near 175°W) appears well aligned with the plume of clouds in the infrared satellite image. This alignment improves just twelve hours later as the anomaly rapidly doubles in magnitude (to values >120 hPa) and the cloud shield expands on the anticyclonic shear side of a poleward-moving jet streak (Fig. 4.12b). As this positive pressure depth anomaly grows larger, it amplifies the flow in its vicinity, transforming a zonally oriented jet stream at 0000 UTC 16 March (Fig. 4.12a) into one with significant anticyclonic curvature approximately 1000 km farther north by 1200 UTC 17 March (Fig. 4.12c). In response, the broad region of negative pressure depth anomalies off the west coast of North America on 16 March become concentrated and move southward and develop into even larger anomalies. Flow around the amplified trough then drives strong southerly upper-level flow over western North America (Fig. 4.12c), aiding in the northward and eastward progression of the positive 315-330 K pressure depth anomalies originally spawned by the rapid cyclogenesis event near Kamchatka several days earlier.

The collocation of the isolated positive pressure depth anomalies with the cloud shield along and ahead of the frontal wave near the dateline suggests that this event may be particularly useful in demonstrating the process by which air is lifted and exhausted in the mid-latitudes. A cross section taken through the maximum positive pressure depth anomaly immediately after the rapid increase in its magnitude (as indicated on Fig. 4.12b) highlights two distinct plumes of upward vertical motion, both rooted in a region of strong lower tropospheric baroclinicity (Fig. 4.13). The strongest plume appears associated with upright convection rooted in the surface baroclinicity and supported by weak convective stability. Equivalent potential temperatures (θ_{eBL})at the base of the upward vertical motion plume are around 310 K to 315 K and potential temperatures at the top of the plume (θ) are between 320 and 325 K. Since air parcels are likely entrained and detrained throughout the vertical extent of the plume and no one parcel travels the entire vertical extent of this instantaneous vertical motion plume, the conceptual model of air parcels rising from an environment of a given equivalent potential temperature θ_{eBL} to one with a potential temperature θ where $\theta \approx \theta_{eBL}$ (Fig. 4.1b; as described in Section 4.2) appears to be a reasonably good approximation in this real case.

Additional slantwise convection appears to be occurring along the baroclinic zone with a base near the 850 hPa level. Parcels are lifted from this 850 hPa environment with θ_{eBL} around 300-315 K to a potential temperature in the 305-315 K range near 600 hPa (Fig. 4.13), again agreeing well with the $\theta \approx \theta_{eBL}$ approximation. These parcels continue upward from near the 600 hPa level in a region of weaker ascent. The tops of the plumes from both the slantwise and upright convection are characterized by regions of large pressure depth (in the 320-335 K layer for both convective plumes) and low potential vorticity (below 0.25 PVU). The parallels between the large pressure depth and the low potential vorticity values in this cross section reinforce the comparison made previously in Section 4.2 and further highlight the complementary nature of isentropic pressure depth and potential vorticity analyses.

At 0000 UTC 16 March, warm air over North America (Fig. 4.14a) is associated with both large 1000-300 hPa thicknesses (representing tropospheric-deep warmth; Fig. 4.15a) and the positive pressure depth anomalies inflated by the cyclone near Kamchatka (now over North America; Fig. 4.11a, 4.12a). Simultaneously, the frontal wave upstream over the central North Pacific begins to develop (Fig. 4.12a) and amplify the mid-latitude flow and associated positive pressure depth anomalies downstream (Fig. 4.12b,c). This amplification propagates downstream, amplifying the trough and increasingly negative pressure depth anomaly over the west coast of North America (Fig. 4.12b) that, in turn, amplifies the downstream pattern over North America through 19 March. The tropospheric-deep trough and associated low-level cyclone over western North America (Fig. 4.14b, 4.15b, 4.16a) further amplifies the downstream ridge and associated warmth over central and eastern North America, as tropospheric-deep warm air advection is implied across much of the central United States by 0600 UTC 19 March (Fig. 4.14b, 4.15b). At this time, the 315-330 K pressure depth anomalies reach values in excess of 270 hPa and 850 hPa temperature anomalies exceed 25˚C by 1200 UTC 20 March (Fig. 4.14c, 4.16b) as the region of greatest 1000-300 hPa thickness continues to be advected poleward into south central Canada (Fig. 4.15c). Such large isentropic pressure depths continue to be associated with large tropospheric-deep thickness and exceptionally warm temperatures across much of the eastern United States on 20-22 March 2012 (Fig. 4.14b, c; Dole et al. 2014).

4.6. Summary and discussion

A large body of research has firmly established that tropical convection exerts both local and remote impacts on the mid-latitude circulation. While there have been studies that examine some of these relationships from a physical processes perspective (e.g. Jones et al. 2003, Riemer et al. 2008, Riemer and Jones 2010, Grams et al. 2011, 2013, Archambault et al. 2013, 2015), the largest fraction of these investigations suggest that the forcing on the mid-latitudes derives from convective heating without explicitly demonstrating the physical nature of the relationship (e.g. Hoskins and Karoly 1981, Weickmann 1983, Kiladis and Weickmann 1992). Analysis of isentropic pressure depth provides a physically intuitive way to follow mass exhausted by convection and to account for circulations created by the increased mass in a given isentropic layer. While not conserved, large "pools" of pressure depth can be followed over several days, enabling the attribution of remote impacts to the original source of the pressure depth anomaly.

As an illustration of the diagnostic utility of the isentropic pressure depth perspective, the sequence of six events that characterized the March 2012 case is illustrated schematically in Fig. 4.17. The strong MJO event over the Maritime Continent exhausted convection northward (event 1 in Fig. 4.17), creating positive pressure depth anomalies south of the Asian jet (event 2). Consequently, the jet intensified and extended, eventually contributing to the development of a deep cyclone via its exit region circulation which, in turn, inflated pressure depths downstream in the 315-330 K layer (event 3). The resulting inflated 315-330 K layer moved across the eastern Pacific, slowly drifting over North America 4-7 days later (event 4). Farther upstream, the growth of a frontal wave on 16 March resulted in the inflation of the 315-330 K isentropic layer (event 5) and, in turn, the amplification of the downstream flow. This amplified flow reaches western North America in time to build the pre-existing positive pressure depth anomalies from event 4, now over central and eastern North America, farther poleward (event 6). The amplification of the positive pressure depth anomalies in the 315-330 K isentropic layer over North America coincides with the warmest days of the warm spell (20-21 March 2012, Fig. 4.14c, 4.15c).

As described in the March 2012 case study, convection in different environments will inflate different isentropic levels. The specific level is closely tied to θ_e of the boundary layer (θ_{eBL}) in which the convection is rooted. Although the comparison in Fig. 4.5 shows that the 5 K isentropic layer with the greatest pressure depth corresponds well to the average 1000 hPa θ_e regardless of season in the tropics, such a relationship does not hold in the mid-latitudes. While convection in the tropics is frequently widespread, convection in the mid-latitudes tends to be confined to regions characterized by strong forcing for ascent, such as mid-latitude cyclogenetic environments. These two environments result in deep convection inflating vastly different isentropic layers. Monitoring pressure depths in well chosen isentropic layers provides the ability to separately follow mass exhausted from tropical convection versus that exhausted from mid-latitude convection.

The distinct origins of convection that inflates different isentropic layers suggests the utility of analyses that distinguish when forcing for a pattern shifts from tropical to mid-latitude origins. In the March 2012 case, this transition occurred around 12 March (event 3 in Fig. 4.17), as the tropical plume of pressure depth anomalies aided in the intensification and subsequent extension of the east Asian jet stream. The circulation associated with exit region of this jet stream aided in the rapid intensification of the cyclone and the corresponding development of the convection that was responsible for inflating the 315-330 K layer. The 12 March transition shifted focus from the tropics and the 340-355 K layer to the mid-latitudes and the 315-330 K layer, as illustrated schematically (Fig. 4.17) by the switch from red objects (representing the 340-355 K layer) to the blue objects (representing the 315-330 K layer). It seems reasonable to hypothesize that many instances of tropical-extratropical interaction are similarly characterized by a transition phase in which the primary driver of the synoptic-dynamic sequence of events shifts from tropical and subtropical to extratropical processes.

We suggest that the isentropic pressure depth perspective promises further explication of relationships similar to the one proposed by Dole et al. (2014; relating the MJO directly to a mid-latitude response over North America) by partitioning the physical sequence into two readily identifiable processes. The first process examines the nature by which inflations of the 340-355 K layer, typically forced by tropical convection, impact the mid-latitudes. In the March 2012 case, it appears that tropical processes contributed to the extension of the jet and subsequent rapid cyclogenesis. The second process examines the downstream impacts of these mid-latitude interactions, such as the inflation of the 315-330 K layer of the 12 March cyclone near Kamchatka and the amplification of the flow by the 16 March frontal wave near the dateline.

Together, these two processes present a physically coherent explanation of the relationship between remote phenomena. For the case of March 2012, the explanation by Dole et al. (2014) can be complemented by a description of the roles played by the Asian jet and the rapidly deepening mid-latitude cyclone in connecting the MJO to the unusually amplified mid-latitude flow over North America.

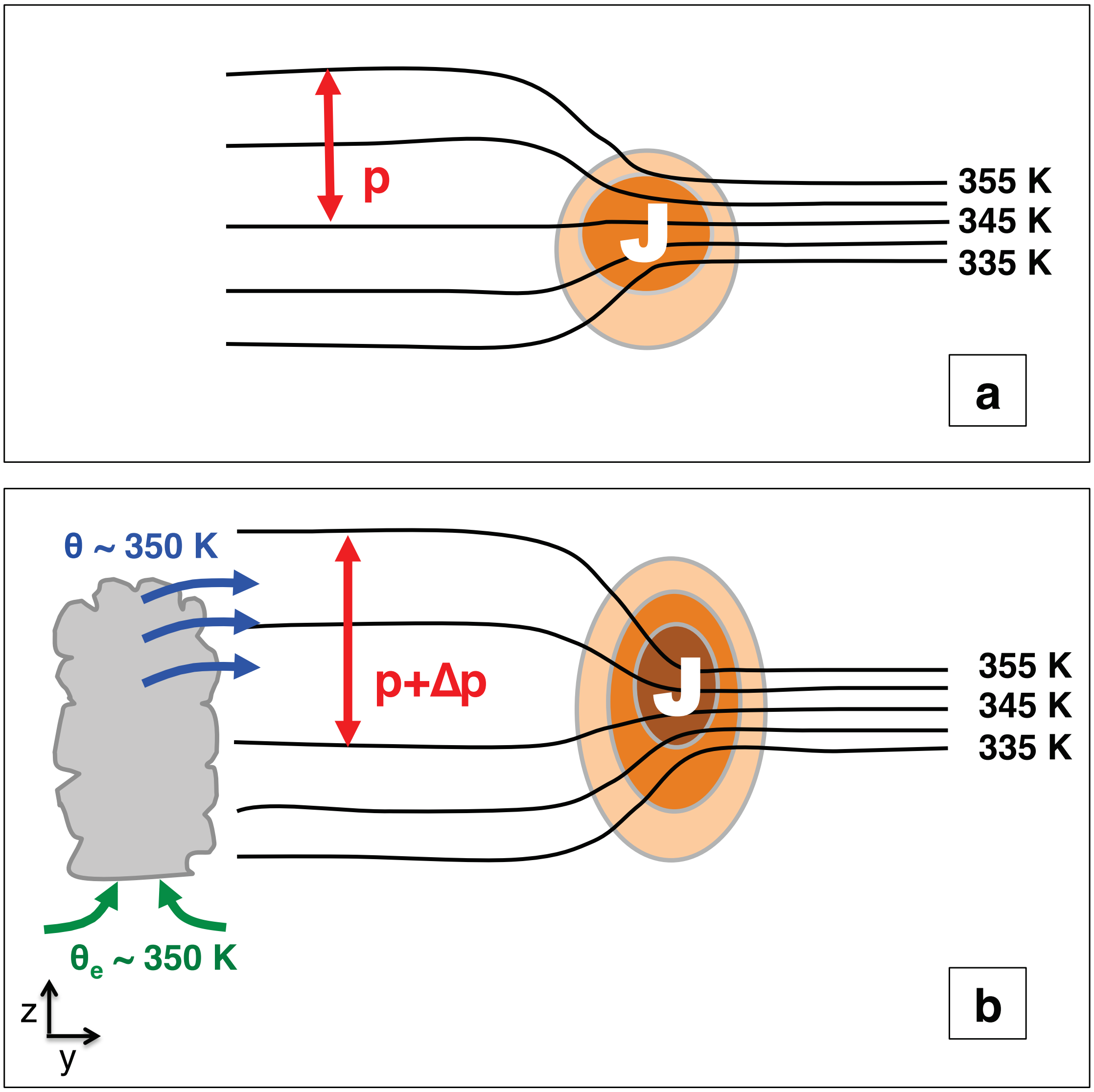

Figure 4.1. Vertical schematics of isentropic pressure depth. Black lines represent isentropes and orange shading represents isotachs. Red line in (a) indicates the pressure depth *p* of an isentropic layer. That layer is inflated by the upward mass flux by deep convection in (b), increasing the isentropic pressure depth to *p+Δp*.

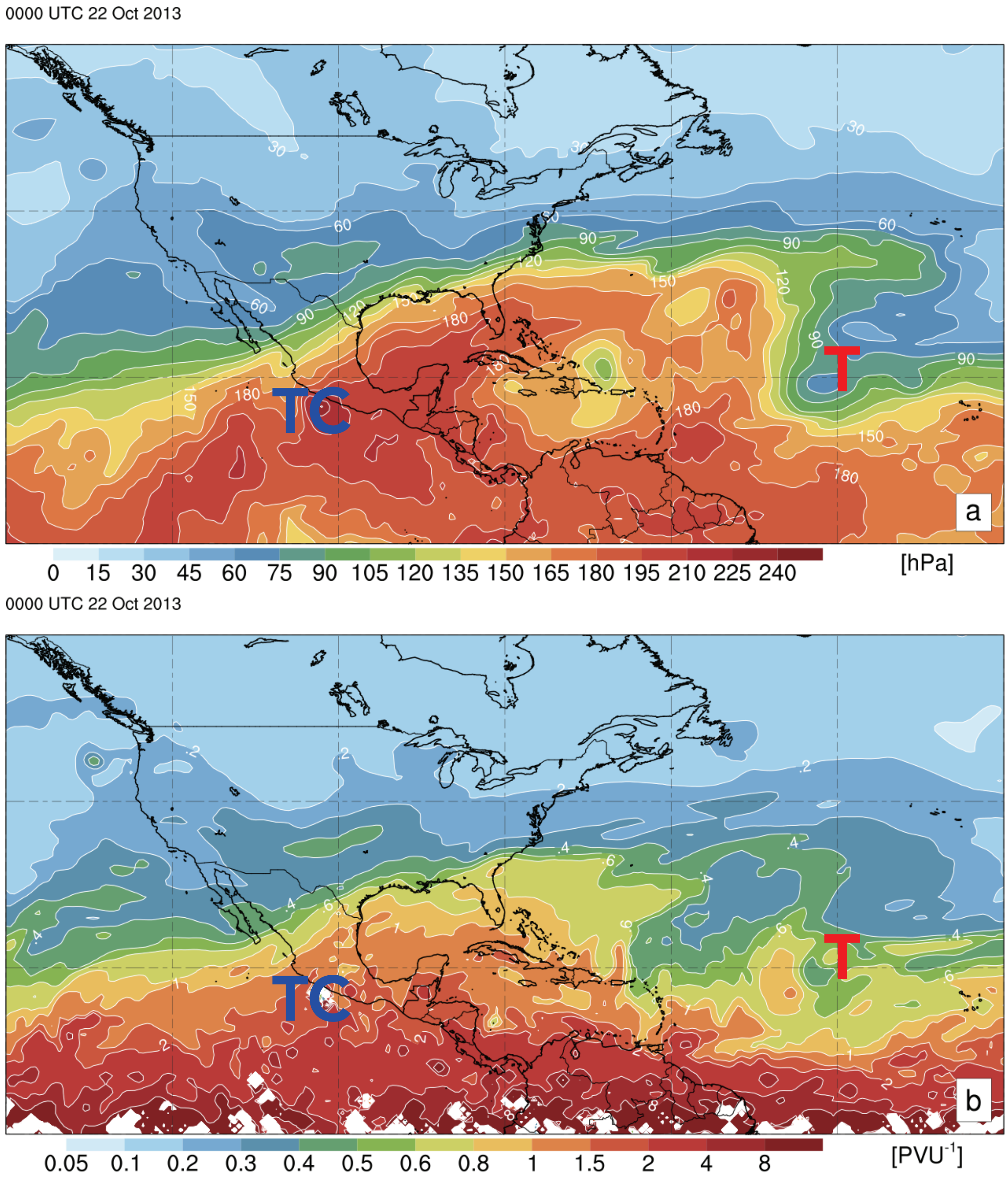

Figure 4.2. Pressure depth (a) and reciprocal of potential vorticity (RPV; b) in the 340-355 K isentropic layer, shaded and contoured per the color bar, for 0000 UTC 22 October 2013. Red “T” indicates the location of an upper level trough, while the blue “TC” indicates the position of TC Raymond.

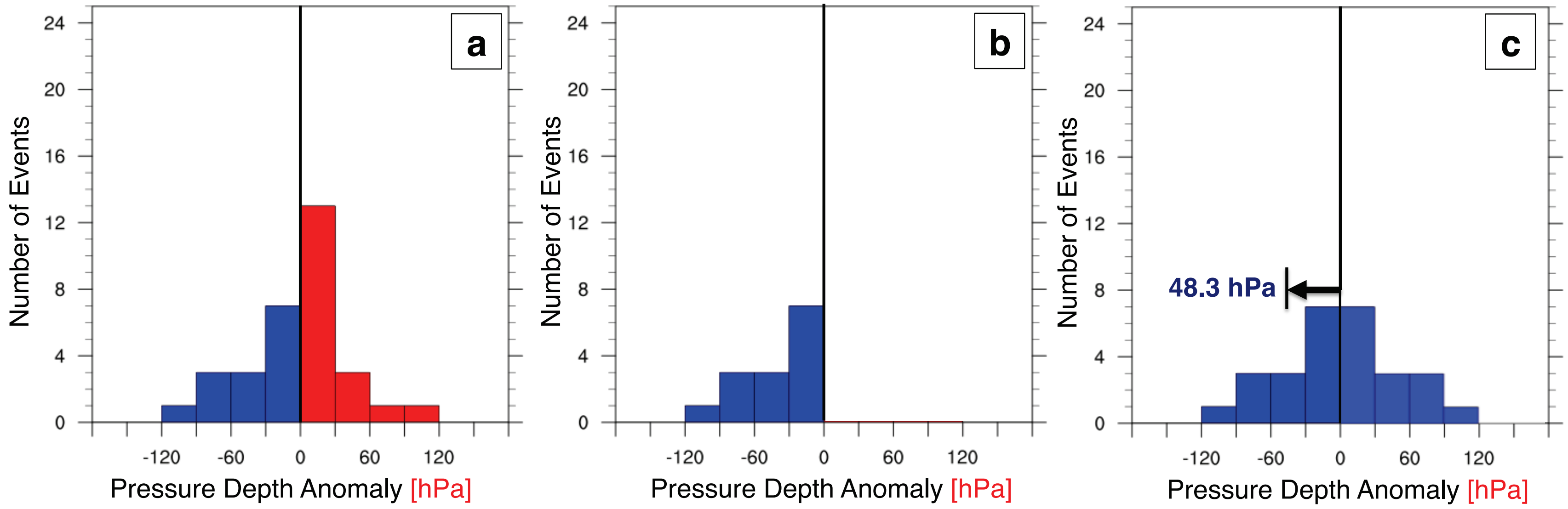

Figure 4.3. Schematic demonstration of the calculation of a negative standard departure value. (a) Distribution of isentropic pressure depth anomalies for a single grid point at a single time across all 32 years of CFSR data. (b) Select only the negative anomaly values from that distribution. (c) Taking the negative of the values remaining in the distribution and include in a new distribution. The *negative standard departure* is then the standard deviation of this newly constructed symmetric distribution.

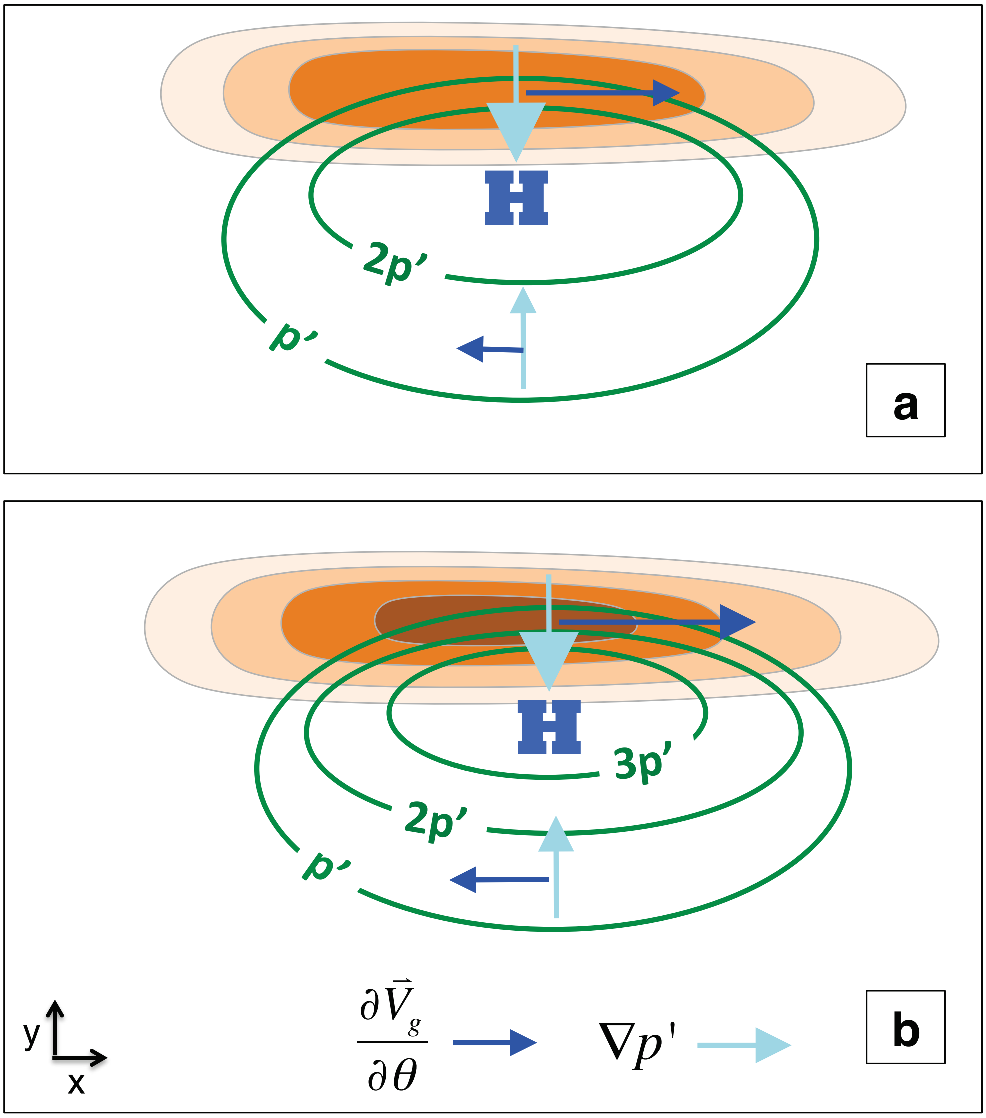

Figure 4.4. Horizontal schematics of isentropic pressure depth. Green lines represent isopleths of isentropic pressure depth within a given isentropic layer and orange shading represents isotachs. An increase in isentropic pressure depth from ~2p’ (a) to ~3p’ (b) can tighten the isentropic pressure depth gradient (light blue arrows) and locally increase the vertical geostrophic wind shear (dark blue arrows) and mean wind speed in that isentropic layer.

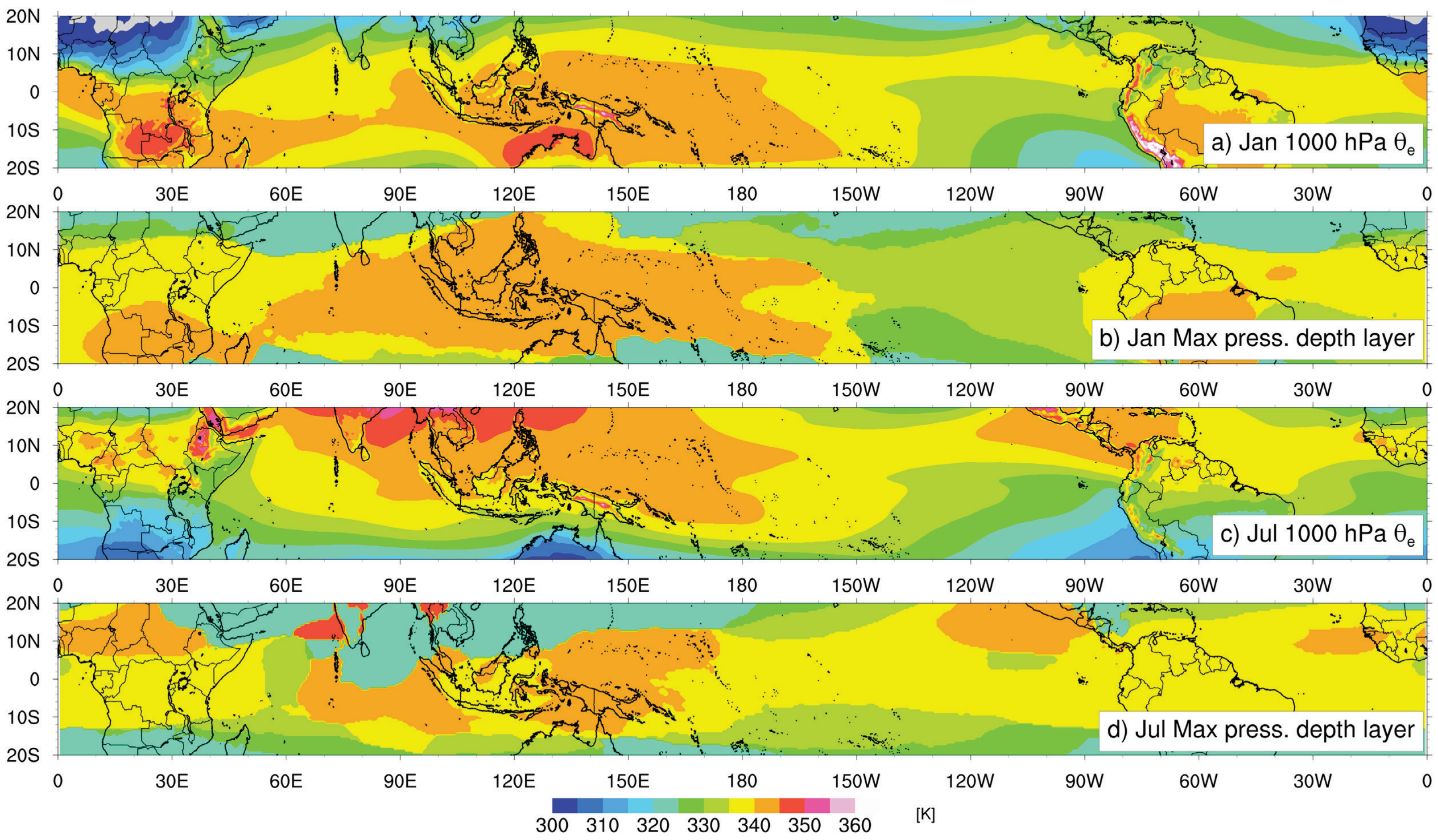

Figure 4.5. Mean 1000 hPa equivalent potential temperature for (a) January and (c) July. Bottom isentropic layer of the thickest 5 K isentropic layer in the climatology of pressure depths for (b) January and (d) July, such that a value of 340 K signifies that the 340-345 K isentropic layer is thicker than any other isentropic layer in that monthly mean.

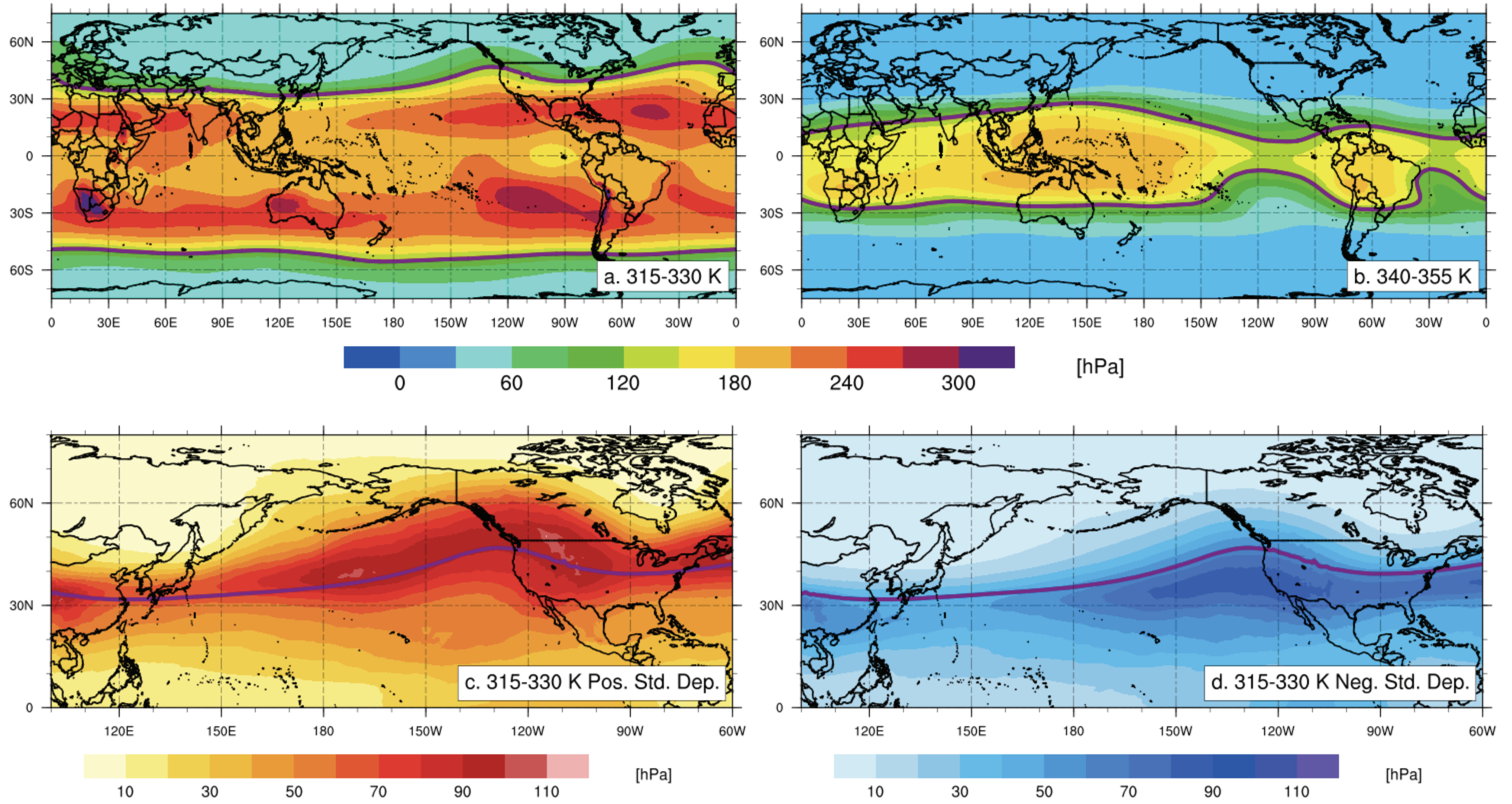

Figure 4.6. Mean January isentropic pressure depths for (a) 315-330 K and (b) 340-355 K layers. Mean January (c) positive and (d) negative standard departures of isentropic pressure depths in the 315-330 K layer. The purple line in (a) and (b) represent the mean 120 hPa isentropic pressure depth isopleth. The 120 hPa isopleth from (a) is reproduced for reference in (c) and (d). Shading per the respective color bars.

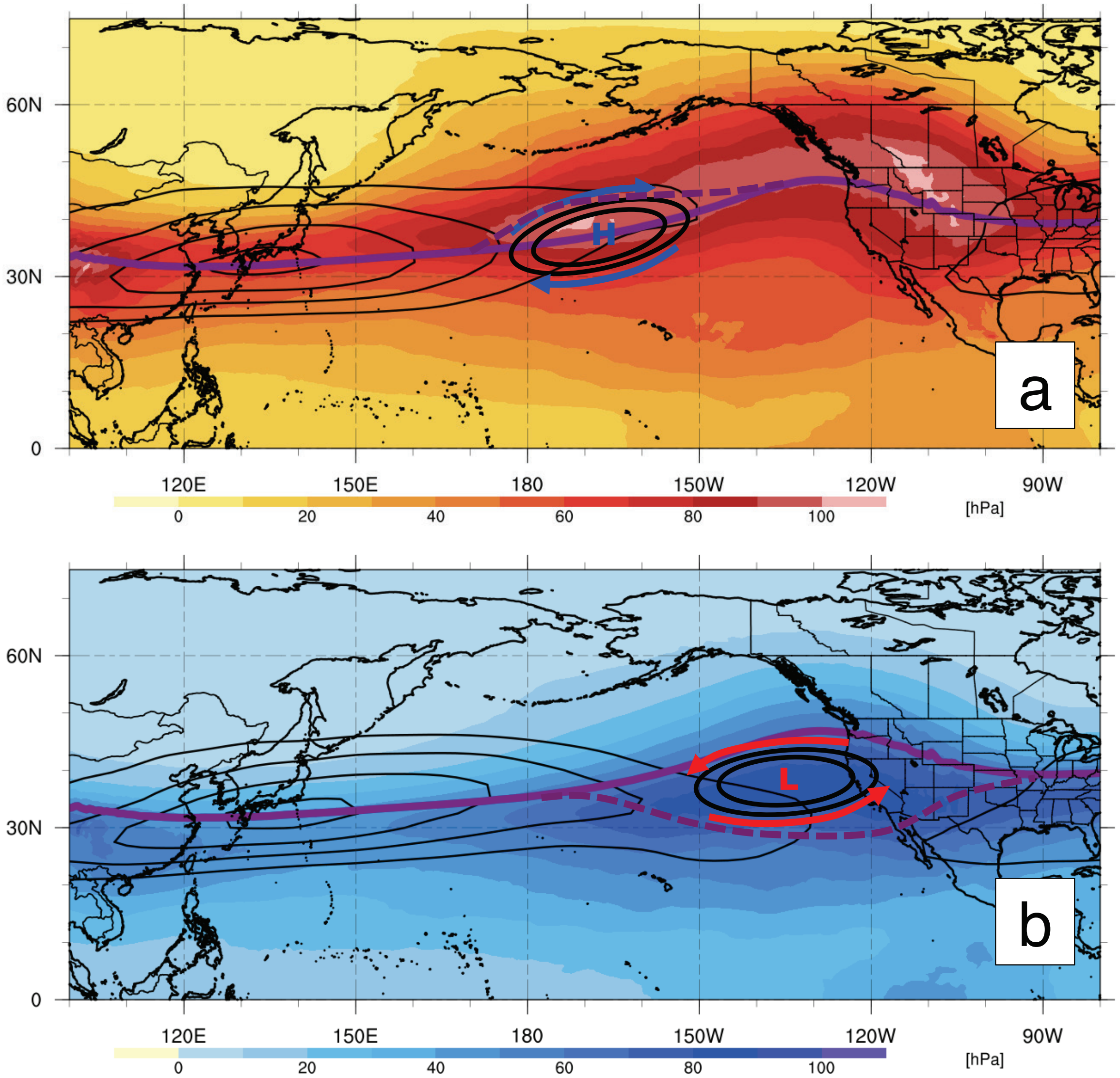

Figure 4.7. Mean January positive (a) and negative (b) standard departures of isentropic pressure depth (shading) in the 315-330 K isentropic layer. Purple line represents the mean January 120 hPa pressure depth isopleth in the 315-330 K layer. Composite zonal wind (black contours) associated with events where isentropic pressure depth exceeds (a) +1.5 standard departures at 42.5˚N, 167.5˚W (blue H) and (b) -1.0 standard departure at 37.5˚N and 137.5˚W (red L). Thick black contours are representative isentropic pressure depth anomalies, with the (a) blue and (b) red arrows indicating the direction of the vertical geostrophic wind shear associated with each representative anomaly. The dashed purple line indicates where the solid purple line (120 hPa isopleths) might shift in response to the imposition of the representative anomalies.

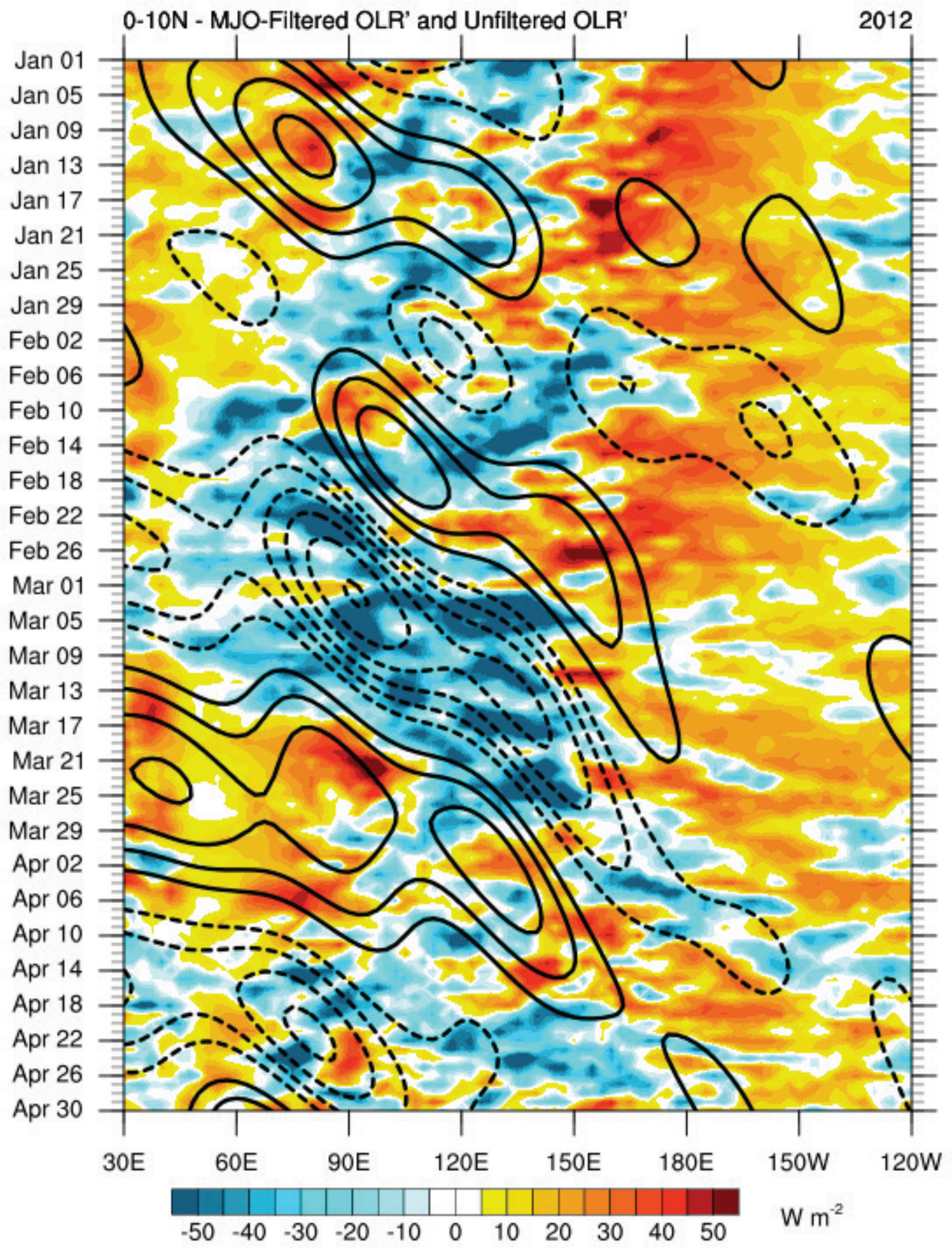

Figure 4.8. OLR anomalies (shaded, W m^{-2}) and OLR filtered for MJO in wavenumber-frequency space (per Kiladis 2009) in contours (dashed where negative, signifying active MJO convection; every 5 W m^{-2}, excluding the zero contour).

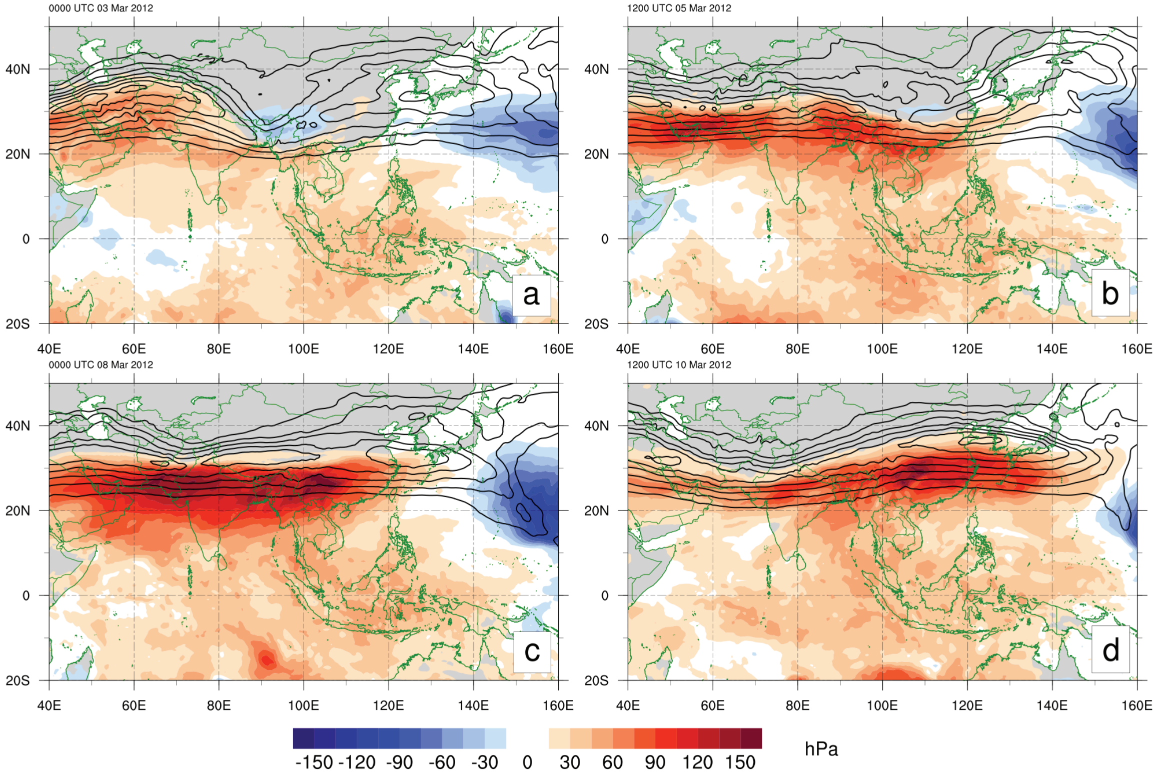

Figure 4.9. 340-355 K layer mean wind speed (shaded; >30 m s^{-1}) and pressure depth anomalies (red where positive, blue where negative, contoured every 15 hPa) for (a) 0000 UTC 3 March 2012, (b) 1200 UTC 5 March, (c) 0000 UTC 8 March, and (d) 1200 UTC 10 March.

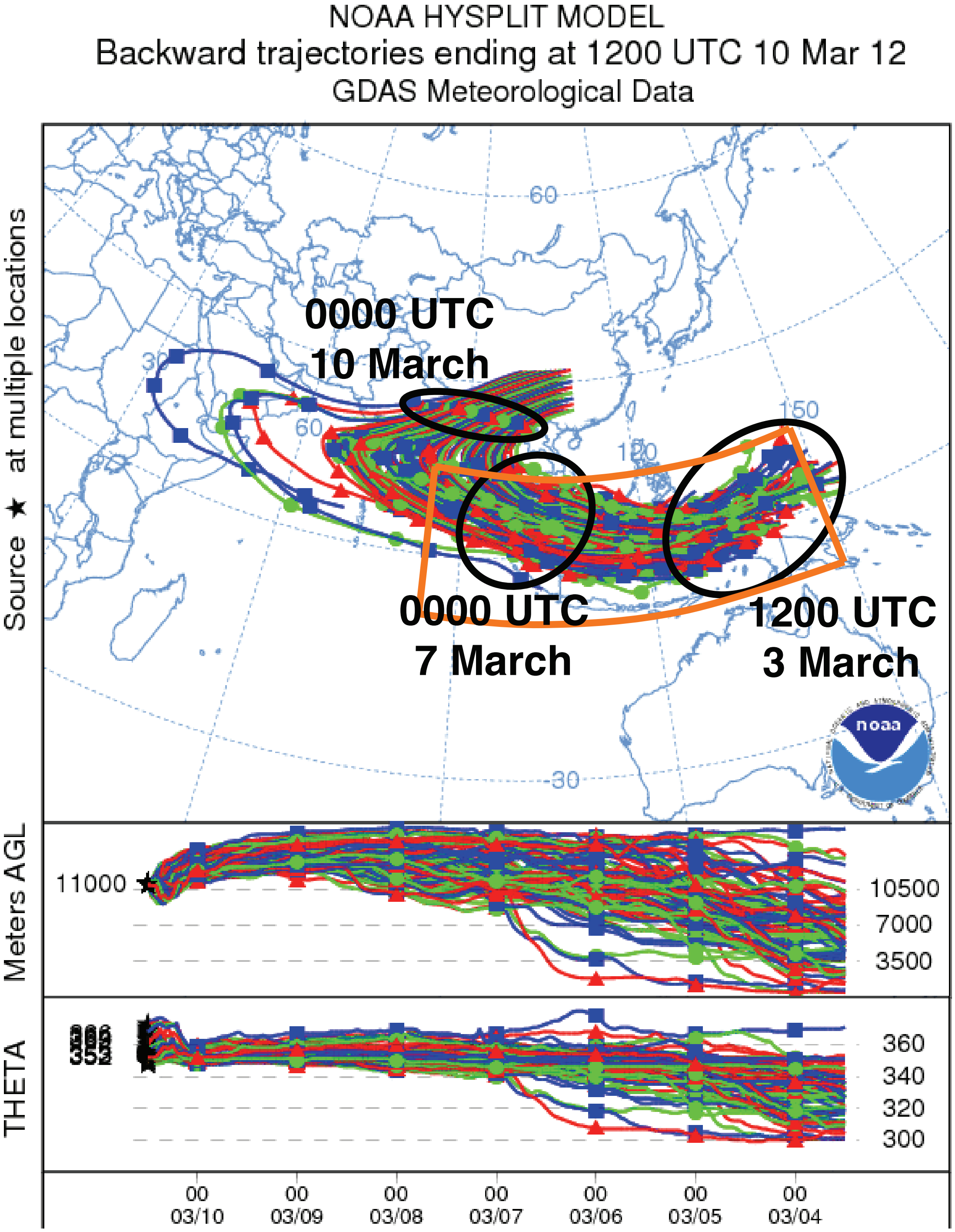

Figure 4.10. Backward trajectories initialized at 1200 UTC 10 March and run backward 7 days (dots at 0000 UTC each day) from NOAA HYSPLIT. Black circles encompass nearly all trajectory locations at the labeled times. Orange box indicates the approximate envelope of the MJO event between 3 March and 8 March, consistent with data in Fig. 4.8. Time series of altitude and potential temperature are also plotted along path of trajectories in inset.

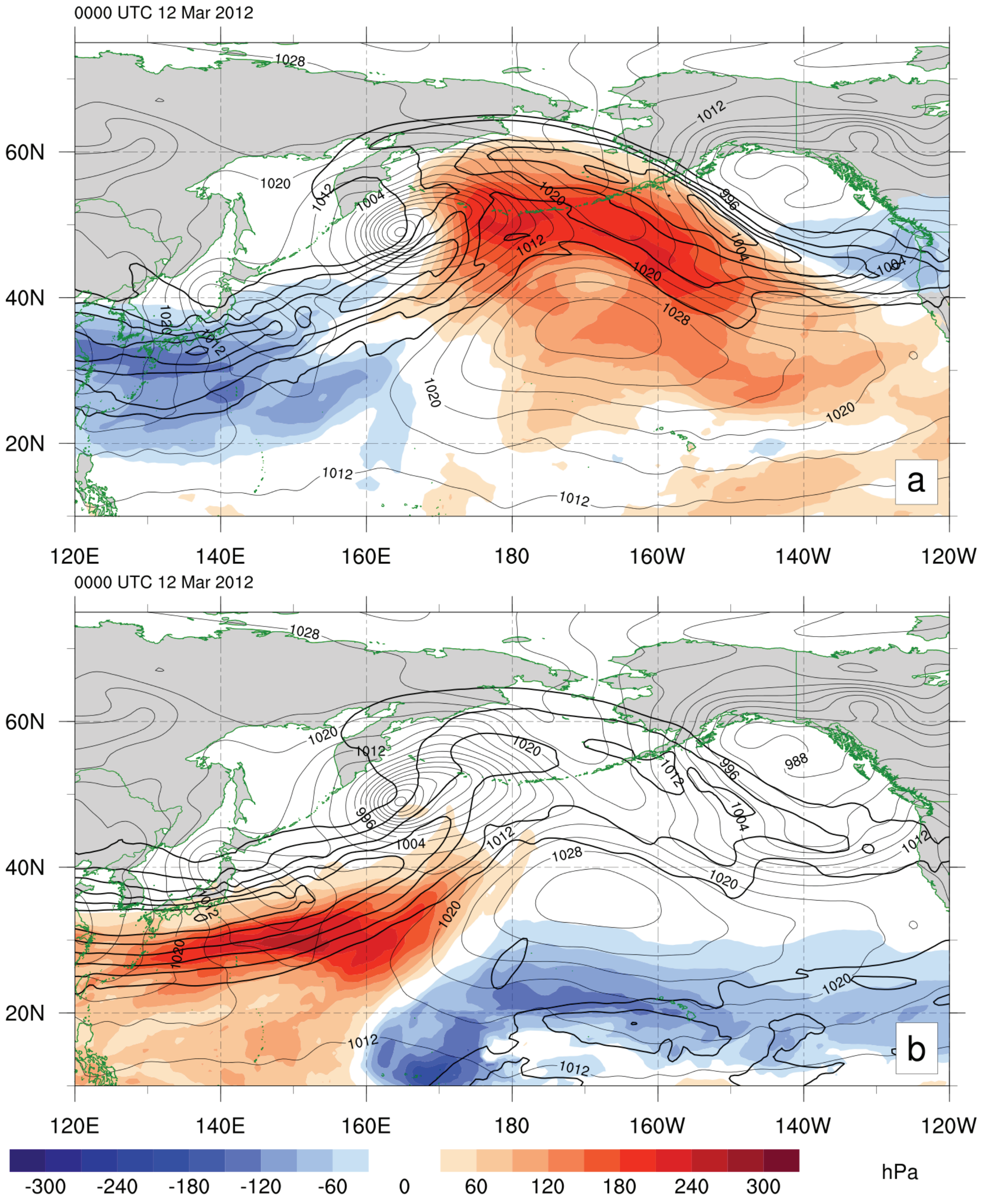

Figure 4.11. As in Fig. 4.9 for 0000 UTC 12 March in (a) 315-330 K (pressure depth anomalies contoured every 30 hPa) and (b) 340-355 K. Mean sea level pressure (black contours, every 4 hPa) plotted in each panel.

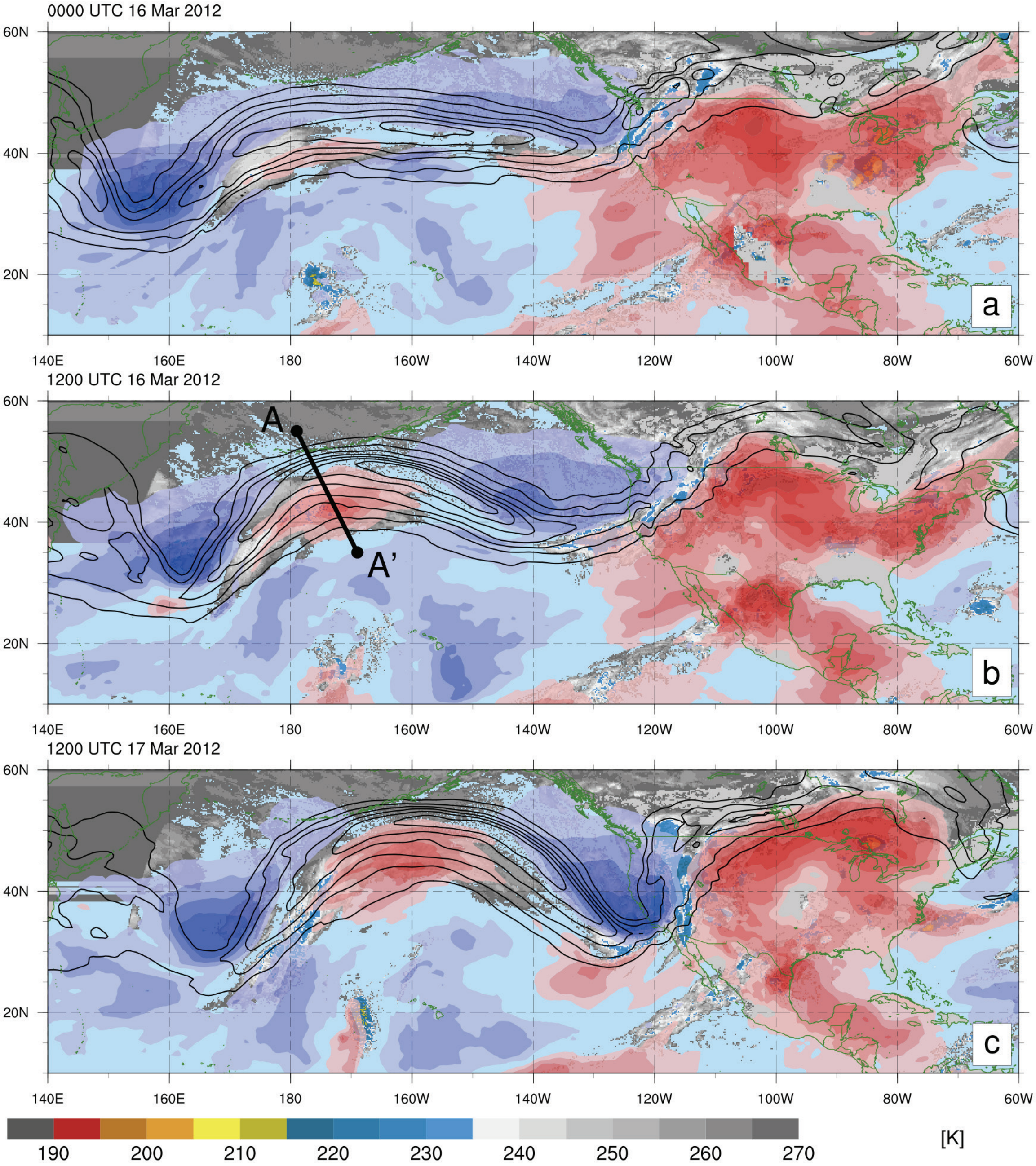

Figure 4.12. As in Fig. 4.9 in the 315-330 K layer at (a) 0000 UTC 16 March, (b) 1200 UTC 16 March, and (c) 1200 UTC 17 March. Infrared imagery at each time is underlain where brightness temperatures are colder than 270 K. Black line A-A' on (b) indicates location of cross section presented in Fig. 4.13.

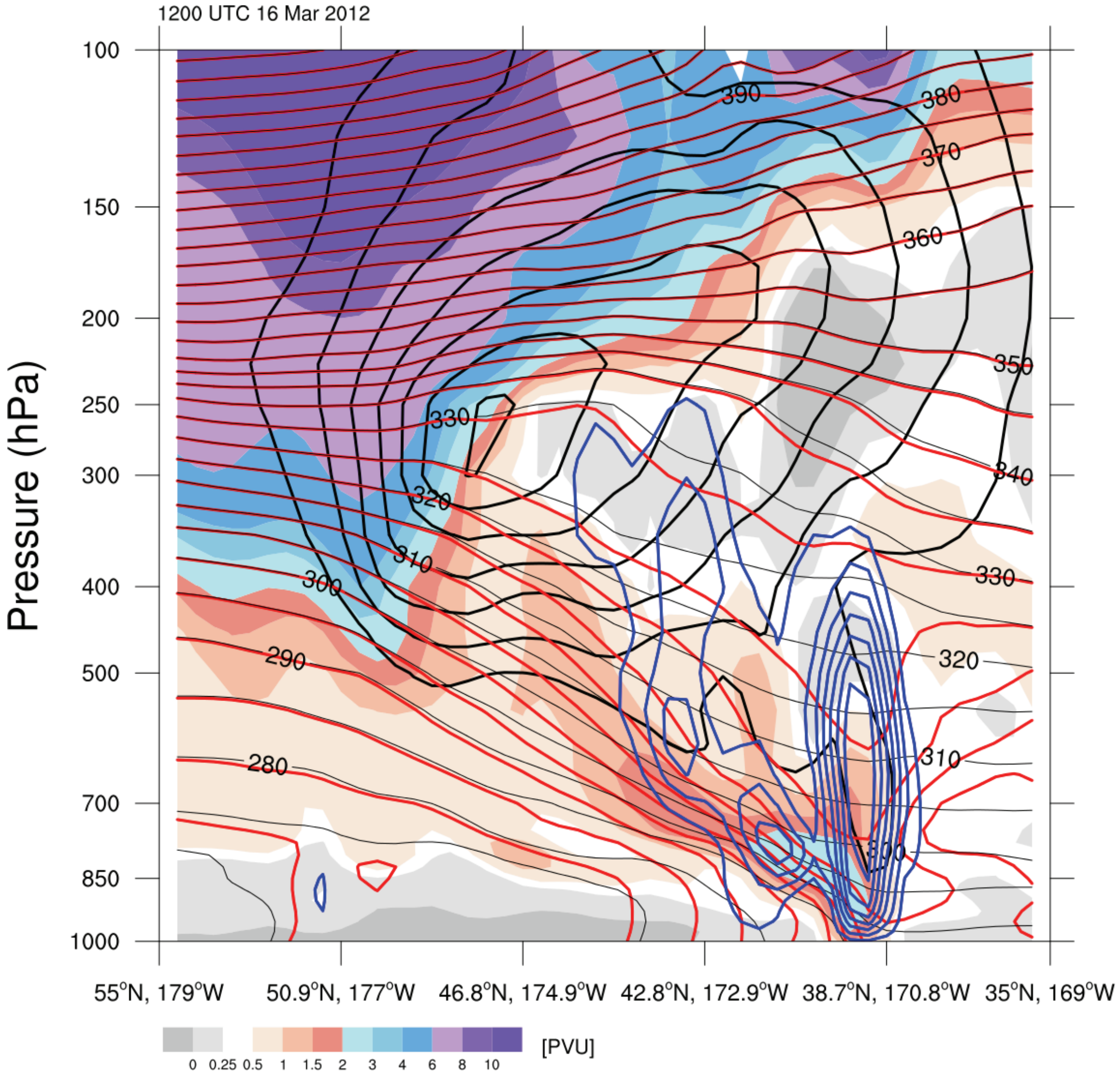

Figure 4.13. Cross section along line as indicated in Fig. 4.12b. Plotted are potential vorticity (shaded), isotachs of wind speed perpendicular to the cross section (thick black contours; every 10 m s^{-1} starting at 30 m s^{-1}), potential temperature (thin black lines as labeled, every 5 K) and equivalent potential temperature (red lines, every 5 K). Upward vertical motion is plotted every .25 hPa s^{-1}.

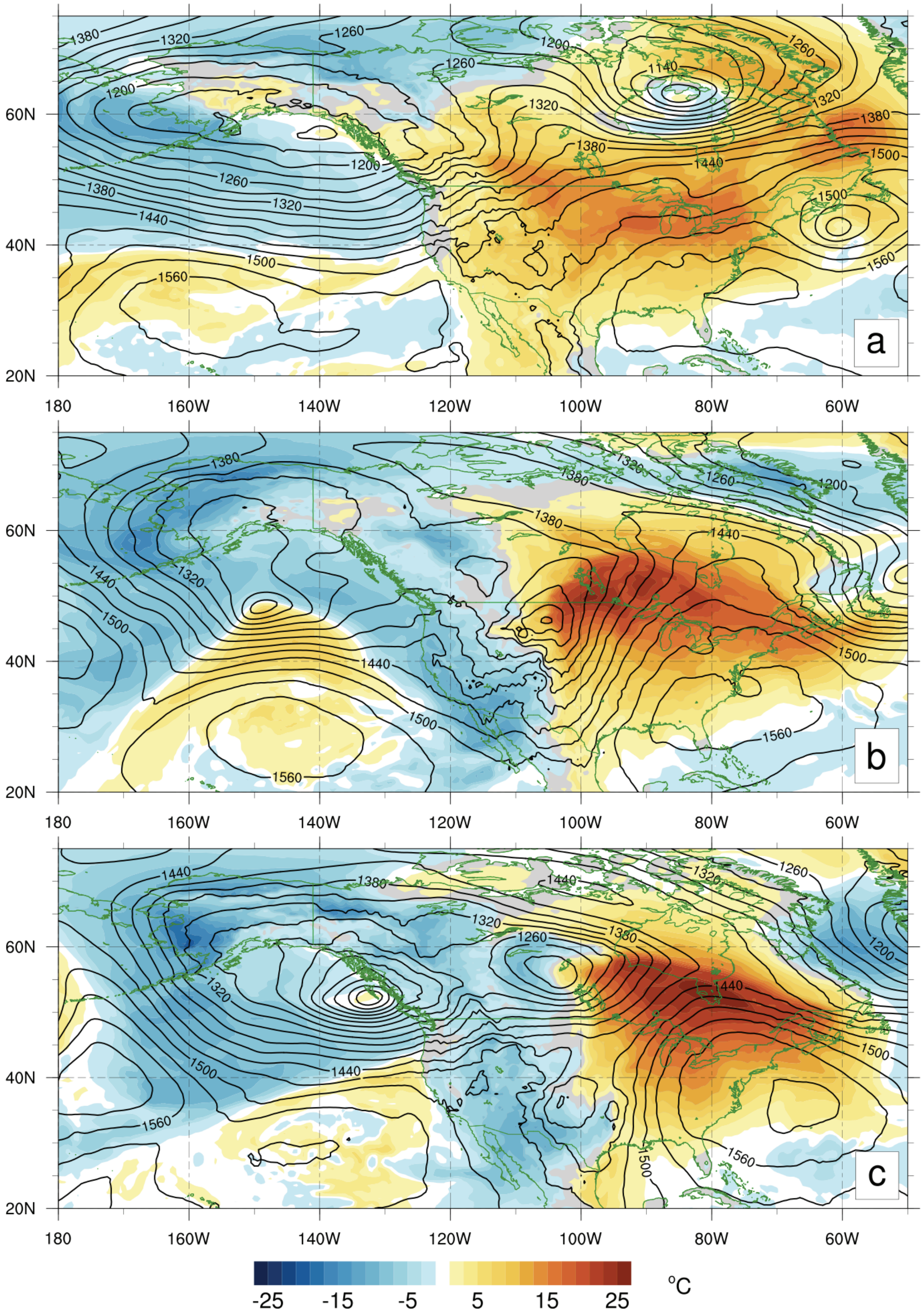

Figure 4.14. 850 hPa heights (contours; m) and temperature anomalies (shading; ˚C) at (a) 0000 UTC 16 March 2012, (b) 0600 UTC 19 March, and (c) 1200 UTC 20 March.

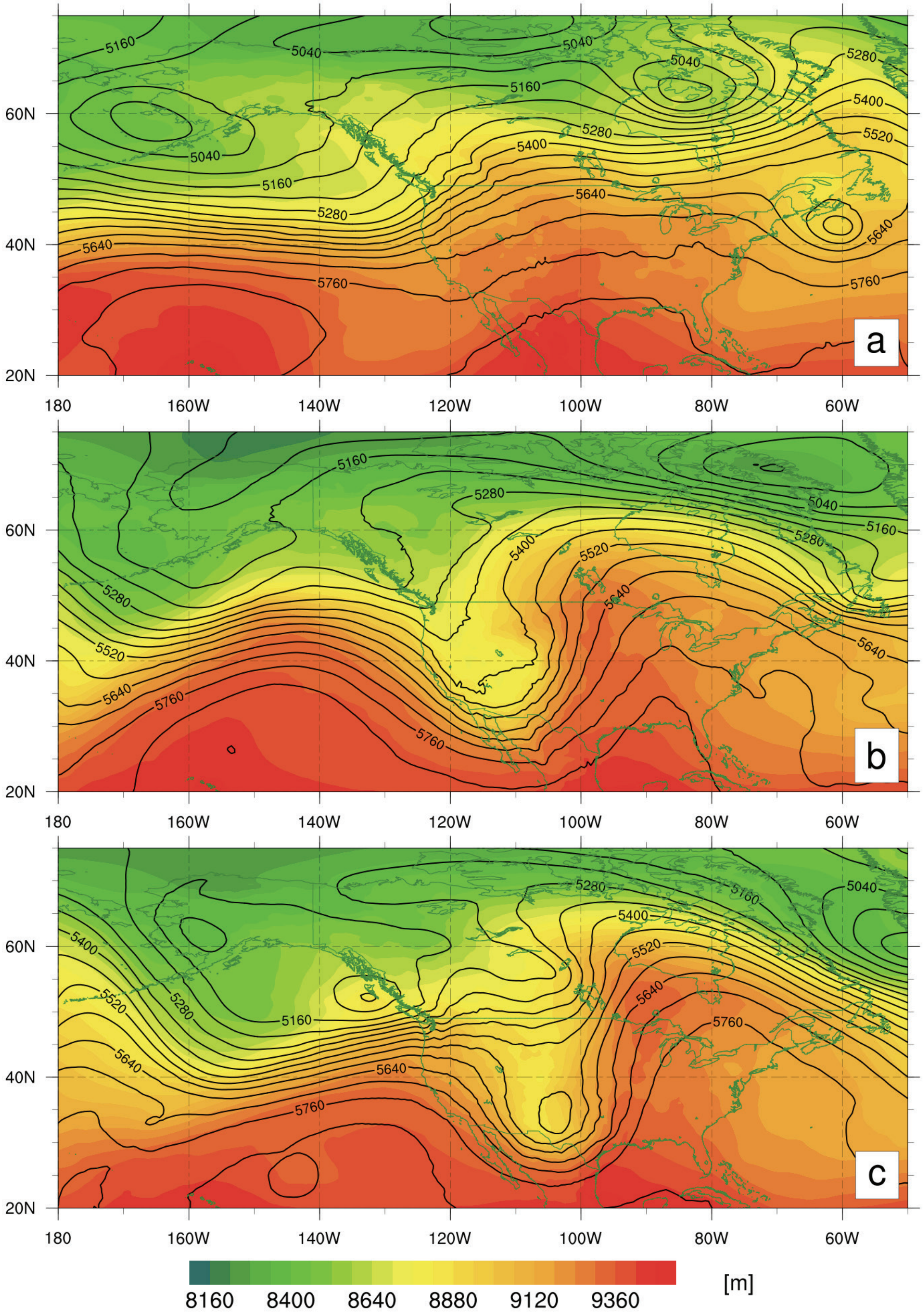

Figure 4.15. 1000–300 hPa thickness (shading; m) and 500 hPa height (black contours, every 60 m) at (a) 0000 UTC 16 March, (b) 0600 UTC 19 March, and (c) 1200 UTC 20 March.

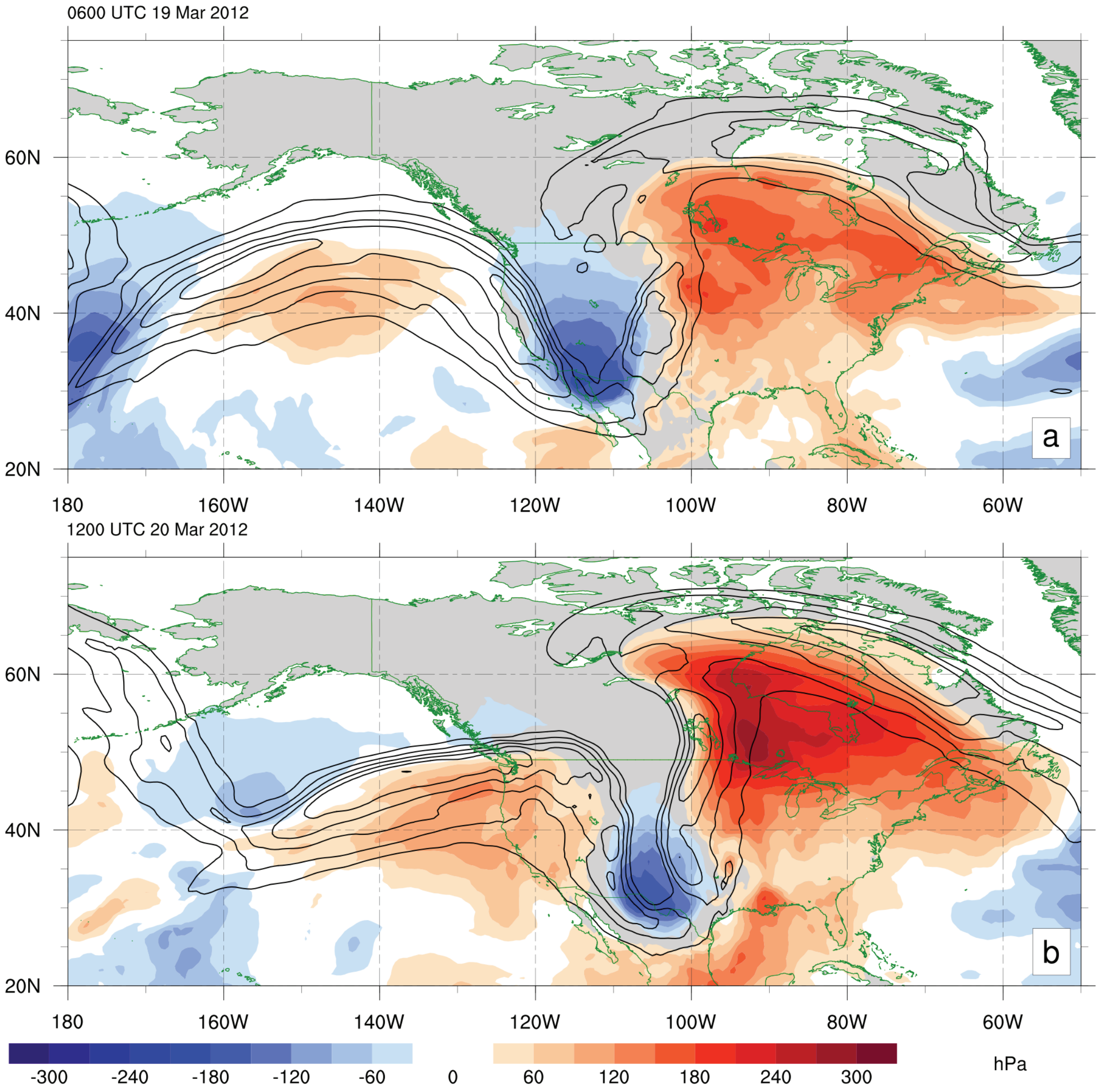

Figure 4.16. As in Fig. 4.9 for the 315-330 K layer at (a) 0600 UTC 19 March and (b) 1200 UTC 20 March.

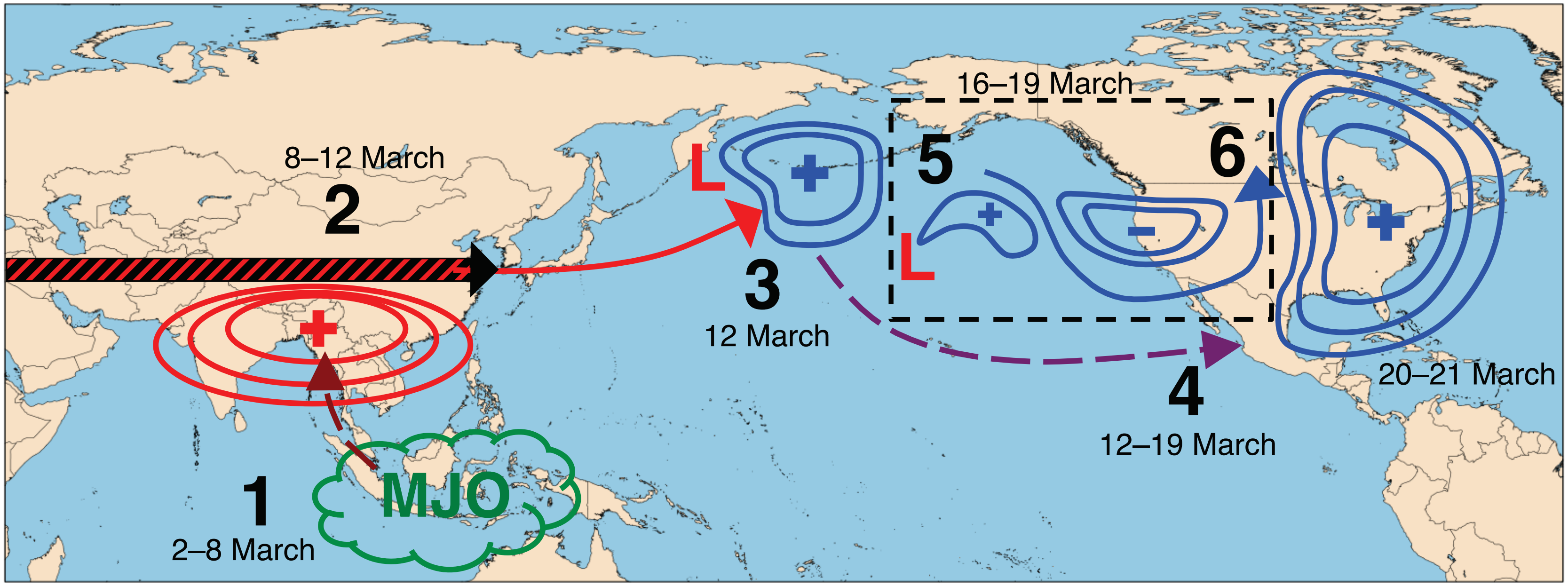

Figure 4.17. Schematic of March 2012 case study. Events in the 340-355 K layer are colored in red while events in the 315-330 K layer are colored in blue. Numbers correspond with events as referenced in section 4.6.

5. Isentropic pressure depth precursors to preferred modes of variability of the North Pacific jet stream

The composite analyses based upon TE-EOFs of the North Pacific jet presented in Chapter 3 found several upstream Asian precursors to certain phases of the leading modes of variability. Similar composite OLR analyses (Figs. 3.7 and 3.8) suggested an association with deep convection for both the retracted jet phase and the poleward shifted jet phase. Utilization of isentropic pressure depths may help to better understand such connections and provide insight into the origins of the upstream Asian precursors, both tropical and extratropical. As discussed in the previous chapter, the pressure depth of the 340-355 K isentropic layer contains the exhaust from deep convection in the tropics. Consequently, growth of positive pressure depth anomalies in tropical and subtropical latitudes can be connected with deep convection. The pressure depth of the 315-330 K isentropic layer, on the other hand, traces the exhaust from convection rooted in the mid-latitudes.

As discussed in Chapter 4, the greatest additional insight provided by isentropic pressure depth stems from examining the impact of mass exhausted by deep convection on the mid-latitudes. Intrigued by the OLR composites presented in Figures 3.7 and 3.8, additional composite analyses have been constructed as discussed in Chapter 2 to supplement the composite analyses presented in Chapter 3. Since a primary use of isentropic pressure depths is to trace the exhaust from deep convection, these composite analyses focus on utilizing this diagnostic tool to examine the events preceding peaks in each of the phases of the two leading modes of variability.

5.1. Composite analyses of extended jet cases

In the composite analyses constructed from extended jet cases, two prominent negative pressure depth anomalies are already present in the 315-330 K isentropic layer at D-15d (Fig. 5.1a) - one around the Tibetan plateau and one south of the Aleutian Islands near the climatological exit region of the jet stream. Each anomaly remains quasi-stationary through D-10d (Fig. 5.1b), and by D-5d (Fig. 5.1c), the magnitude of the anomalies increases significantly as the Tibetan anomaly expands into the core of the climatological 250 hPa jet and spreads eastward over the western Pacific. In doing so, the Tibetan anomaly begins to merge with the negative pressure depth anomaly centered around 170˚W, creating a single broad negative pressure depth anomaly stretching from 80˚E to 140˚W. Such an expansive anomaly within a composite analysis may represent a single broad trough or the mean of a series of troughs spread across a range of longitudes. Across much of that longitude range, the negative anomalies are contained between 15˚-45˚N and span the core of the climatological 250 hPa jet.

The sprawling negative anomaly peaks in magnitude at D0 (less than -72 hPa; Fig. 5.1d) while centered near 155˚W, a location farther east than on D-5d. While negative anomalies continue to extend as far south as 15˚N, a tight gradient in pressure depth aligns well with the core of the 250 hPa zonal wind anomalies along 30˚N east of 180˚ longitude. East of the jet exit region, over western North America, a positive pressure depth anomaly has increased in magnitude and extent, perhaps in response to the strong negative pressure depth anomaly upstream via a process similar to downstream development (e.g. Simmons and Hoskins 1979, Orlanski and Sheldon 1993). Immediately downstream of this positive pressure depth anomaly, this downstream development appears to continue as a small region of negative pressure depth anomalies also increase in magnitude at D0 and D+5d over the southeast United States (Fig. 5.1d, e). The most prominent feature in the composites beyond D+5d is the large negative pressure depth anomaly south of the Aleutians, which weakens dramatically from D0 through D+10 (Fig. 5.1f). The 25-day persistence of this feature strongly suggests jet extension events have a preference for a background state that favors the existence of a trough in this location.

A simpler pattern emerges from composites of pressure depth anomalies in the 340-355 K isentropic layer. A broad positive pressure depth anomaly spans much of the central and eastern tropical Pacific at D-15d (Fig. 5.2a) while a small positive anomaly over south China enters the entrance region of the climatological jet stream by D-10d (Fig. 5.2b). These two anomalies have merged by D-5d (Fig. 5.2c) as the positive anomaly in the tropical Pacific expands westward while the south China anomaly has moved through the core of the jet and into the jet exit region. Both have combined to create a broad positive pressure depth anomaly located immediately equatorward of the climatological exit region of the jet west of 180˚ longitude at D-5d (Fig. 5.2c). The 250 hPa zonal wind anomaly poleward of this pressure depth anomaly takes on an anticyclonically curved shape, aided in its amplification by a small negative pressure depth anomaly along the coast of China. The positive pressure depth anomaly shifts 20˚ eastward in the following days and is centered near 165˚W at D0 (Fig. 5.2d), supporting a large zonal wind anomaly in excess of 30 m s^{-1} at that same longitude. The anomaly continues shifting eastward through D+5d (Fig. 5.2e) and weakens back toward its original tropical east Pacific position by D+10d (Fig. 5.2f).

Considering the evolution of these two isentropic layers in concert leads to a straightforward conceptual model of the evolution of extended jet events. First, a large cyclonic circulation anomaly forms on the poleward flank of the climatological jet exit region, inducing anomalous westerly winds to its south. At the same time, a broad anticyclonic circulation anomaly forms on the equatorward flank of the climatological jet exit region, inducing anomalous westerly winds to its north. The vertical superposition of anomalous westerly winds, or more specifically, westerly geostrophic vertical wind shear, supports an intense and deep vertical wind shear profile across the 315-330 K and 340-355 K isentropic layers, which is in turn reflected as anomalous upper tropospheric westerly winds. This pairing of pressure depth anomalies occurs in 78% of the 40 jet extension events at D0 (Fig. 5.1d), with only 5% of cases having neither a negative anomaly in the 315-330 K layer nor a positive anomaly in the 340-355 K layer[2].

Less clear, however, is the evolution of the synoptic scale patterns that precede the establishment of each of the two main pressure depth anomalies. In the 315-330 K layer, two distinct negative pressure depth anomalies appear to come together in the composite mean, but are not necessarily present simultaneously. Only 53% of the 40 jet extension events contain both negative pressure depth anomalies (in excess of -24 hPa in the 315-330 K isentropic layer) prior to the merger, when each is centered over the Tibetan Plateau and the central Pacific at D-10d (Fig. 5.1b). The resulting implication that either one of these anomalies may be weak or absent in nearly half of the jet extension cases in the composite analysis greatly contrasts with the composite mean. Further analysis of the

---

[2] Pressure depth anomalies are identified for each case in the 315-330 K layer when negative anomalies near the location of minimum composite pressure depth anomaly exceeded -24 hPa. Positive pressure depth anomalies exceeding +12 hPa were identified in 340-355 K layer in a similar manner. The presence of anomalies for each event was then cross checked in both layers in order to calculate the percentage of jet extension events where the anomalies were present simultaneously.

frequency with which features from the composite mean appear in individual cases will allow for a better understanding of the various sequences that may lead to jet extensions.

5.2 Composite analyses of retracted jet cases

Separate regions of positive pressure depth anomalies can be identified in the 315-340 K isentropic layer near the Tibetan Plateau and across much of the eastern North Pacific at D-10d in association with retracted jet cases (Fig. 5.3b). While generally absent at D-15d (Fig. 5.3a), the positive pressure depth anomalies consolidate between D-10d and D-5d (Fig. 5.3c) as the Asian anomalies move into the climatological jet stream by D-9d (not shown) and begin to merge with the eastern North Pacific anomalies by D-5d. This leads to a more intense positive pressure depth anomaly that supports a tighter pressure depth gradient on its equatorward flank leading, in turn, to stronger negative zonal wind anomalies at 250 hPa by D-5d that are also generally equatorward of the eastern part of the anomaly.

The negative 250 hPa zonal wind anomaly intensifies through D0 (Fig. 5.3d) as the positive pressure depth anomaly reaches its greatest intensity in excess of 84 hPa just east of 180° longitude. At this point in time, the higher latitudes are characterized by enhanced westerly winds (greater than 20 m s^{-1} at 250 hPa) on the poleward flank of the composite positive pressure depth anomaly while the mid-latitudes are characterized by decreased westerly winds on the equatorward flank of the pressure depth anomaly, (peaking below -30 m s^{-1} at 250 hPa). This pattern at D0 remains quasi-stationary through D+5d (Fig. 5.3e), during which time the positive pressure depth anomaly maintains its maximum magnitude (greater than 84 hPa). The longevity of this positive pressure depth anomaly suggests the resulting pattern blocks the mid-latitude flow (e.g. Rex 1950, Jayawardena and Chen 2006) as early as D-5d (Fig. 5.3c). While still somewhat present at D+10d (Fig. 5.3f), the positive pressure depth anomaly has weakened and no longer implies blocked flow in the composite mean.

The composite pressure depth anomaly evolution in the 340-355 K layer also has two main features, with a weak positive pressure depth anomaly near the coast of China at D-15d (Fig. 5.4a) and broad negative pressure depth anomalies over the eastern Pacific south of 30˚N and east of 160˚E. These negative pressure depth anomalies expand westward by D-10d (Fig. 5.4b) into a region equatorward of the exit region of the climatological jet stream. The negative 250 hPa zonal wind anomalies at D-10d align well with the northern gradient of the negative pressure depth anomaly, suggesting the resultant anomalous geostrophic wind shear likely contributes to the reduced westerly flow. The magnitudes of both the negative zonal wind anomaly and negative pressure depth anomaly are notably greater by D-5d (Fig. 5.4c) as both extend as far west as the coast of Japan and the core of the climatological 250 hPa jet.

D0 brings about the most intense negative pressure depth anomaly in the 340-355 K isentropic layer (less than -48 hPa; Fig. 5.4d), with the greatest associated pressure depth gradient positioned in the core of the negative 250 hPa zonal wind anomaly. Simultaneously, the positive pressure depth anomaly over south China has become larger and more intense since D-5d (Fig. 5.4c), an inflation that may be occurring in response to anomalous outgoing longwave radiation (OLR) in the region as shown in a similar composite analysis in Chapter 3 (Fig. 3.7b). Deep convection associated with the composite negative OLR anomalies over Indonesia and adjacent portions of the Indian Ocean likely exhausts mass in the 340-355 K isentropic layer, inflating it, and growing the positive pressure depth anomalies over the D-5d to D0 period. However, as noted in Chapter 3, these negative OLR anomalies are not particularly strong and may not be present in all jet retraction cases, a caveat that also applies for the positive pressure depth anomaly over southern China (the positive pressure depth anomaly exceeds 12 hPa in about 70% of cases at D0 and is present in fewer than 60% at D-5d and D+5d). While small lobes of this composite positive pressure depth anomaly move into or through the jet core by D+5d (Fig. 5.4e), it is unclear whether these lobes impact the position or intensity of the large negative pressure depth anomaly further east. That composite negative anomaly retreats eastward and weakens to a magnitude of about -36 hPa by D+5d, but does not retreat southward. Likewise, the negative 250 hPa zonal wind anomaly also shifts eastward while only weakening slightly. A more marked reduction in both the magnitude of the negative pressure depth anomaly and the zonal wind anomaly occurs by D+10d (Fig. 5.4f). A corresponding frequency of occurrence analysis shows that in the core of the negative pressure depth anomalies at D-5d, D0, and D+5d, over 80% of the 40 composited events contained anomalies less than -12 hPa. While this frequency rises above 60% as early as D-15d and exceeds 70% by D-10d, it falls to near 60% by D+10d, implying that the presence of negative pressure depths in the 340-355 K layer is more common over the two weeks prior to peak jet retraction and the negative anomalies decay more rapidly after peak retraction.

Composites of the 315-330 K and 340-355 K layers allow for the construction of a conceptual model of jet retraction events similar to that presented for jet extension events. In the composite jet retraction, peak retraction (D0) occurs with an intense and expansive positive pressure depth anomaly in the 315-330 K layer on the poleward flank of the climatological jet exit region (Fig. 5.3d) and a comparably intense negative pressure depth anomaly in the 340-355 K layer on the equatorward flank of the climatological jet exit region (Fig. 5.4d). Both pressure depth anomalies are associated with a pressure depth gradient that allows for the superposition of anomalous easterly geostrophic vertical wind shear in the region of negative 250 hPa zonal wind anomalies. This superpositioning of anomalous vertical wind shear demonstrates how pressure depth anomalies in different isentropic layers may constructively interact with each other and impart a larger influence on the jet stream than either would impart alone.

5.3 Composite analyses of poleward shifted jet cases

Composites of poleward shifted jet cases show loosely organized pressure depth anomalies in the 315-330 K isentropic layer at D-15d (Fig. 5.5a) and D-10d (Fig. 5.5b). The primary anomaly features are an expansive region of positive pressure depth anomalies over the eastern North Pacific and southern North America as well as a region of negative pressure depth anomalies over much of south Asia. While the positive pressure depth anomalies appear to concentrate between 180° and 150°W by D-10d, the negative anomalies are punctuated by the sudden emergence of a positive pressure depth anomaly over central China, immediately downstream of the Tibetan Plateau. This feature, located in the entrance region of the climatological jet at D-10d (Fig. 5.5b), moves into the core of the jet by D-8d and begins to exit the jet by D-6d (not shown), leading to a merger with the stronger positive pressure depth anomaly east of 180° by D-5d (Fig. 5.5c). Interestingly, the positive pressure depth anomaly peaks in magnitude (in excess of 60 hPa) at D-5d and not at D0 (Fig. 5.5d), as is the case in the other composite analyses. Becoming less coherent, the positive pressure depth anomaly moves quickly eastward toward the coast of North America by D0. Simultaneously, the negative anomaly over Asia moves through the jet at D0 and emerges over the central North Pacific by D+5d (Fig. 5.5e). By D+10d (Fig. 5.5f), any anomalies that remain in the 315-330 K isentropic layer do not appear to be associated with the poleward shifted jet.

A more coherent story exists in the 340-355 K isentropic layer, starting at D-15d (Fig. 5.6a) where a dipole of pressure depth anomalies of similar magnitude exists across the lower latitudes of the North Pacific. The positive pressure depth anomalies over Asia begin moving eastward through the core of the climatological jet stream by D-10d (Fig. 5.6b), intensifying south of the climatological jet core by D-5d (Fig. 5.6c) as a positive 250 hPa zonal wind anomaly forms in the jet exit region, well to the north and east of the easternmost extent of the positive pressure depth anomaly. At this initial time (D-5d), the positive 250 hPa zonal wind anomaly over the central North Pacific is predominantly the result of the anomalous vertical geostrophic wind shear associated with the pressure depth gradient on the poleward flank of the 315-330 K pressure depth anomaly (Fig. 5.5c). Between D-5d and D0, support for the 250 hPa zonal wind anomaly is handed off to anomalies in the 340-355 K isentropic layer as the eastern portion of the positive pressure depth anomaly intensifies and expands eastward. In turn, this further strengthens and extends the positive 250 hPa zonal wind anomaly (Fig. 5.6d). In the 315-330 K layer, D0 is also the time that the positive pressure depth anomaly that had been supporting the positive zonal wind anomaly progresses rapidly eastward and seemingly abandons the zonal wind anomaly (Fig. 5.5d). Unfortunately, composite analyses do not allow for a detailed examination of how this handoff occurs, why it occurs, or how often, implying individual studies may provide the greatest additional insight here.

The eastern portion of the positive pressure depth anomaly continues moving eastward through D+5d (Fig. 5.6e) and the positive zonal wind anomaly continues eastward as well on its poleward flank, traveling ~15° of longitude over the five day period. Between D-5d and D+5d, the negative pressure depth anomalies over the tropical eastern Pacific have remained quasi-stationary and shrunk back toward the southeast only when encroached upon by the eastward moving positive pressure depth anomaly. The pressure depth gradient between the positive pressure depth anomaly to the north and the negative pressure depth anomaly to the south supports a negative 250 hPa zonal wind anomaly in excess of -15 m s^{-1} at both D0 and D+5d (Fig. 5.6d, e). Both zonal wind anomalies weaken by D+10d (Fig. 5.6f) with the eastern portion of the positive pressure depth anomaly disappearing completely from the composite mean. Only the western portion of the positive pressure depth anomaly remains near the south China coast at D+10d, as it has throughout the 25-day period.

A key aspect of this positive pressure depth anomaly is its origin. While the existence of the anomaly itself in the composite analysis likely precedes D-15d, its proximity to and apparent connection with the OLR anomalies presented in Chapter 3 with similar composites based on poleward shifted jet events is intriguing. In Fig. 3.8, the OLR anomalies are centered near 110°E at D-5d and shift slowly eastward to around 120°E by D+5d, a progression mimicked by the centroid of the positive pressure depth anomaly over the same D-5d (Fig. 5.6c) to D+5d (Fig. 5.6e) period. The highly anomalous and continuous nature of the deep convection combined with the spatial proximity to and temporal alignment with the positive pressure depth anomaly suggest that these two composite anomalies are closely related to one another. The growth of the eastern lobe of the positive pressure depth anomaly in the 340-355 K isentropic layer at D-5d may be due, in part, to a portion of the mass exhausted from the anomalous deep convection moving away from southeast Asia and supporting the maintenance of the poleward shifted jet at D0 and D+5d (Fig. 5.6d, e).

A frequency analysis shows that of the 36 poleward shifted jet cases in the composite analyses, only 44% contain both a positive pressure depth anomaly in excess of 24 hPa in the 315-330 K layer at D-5d (Fig. 5.5c) and a positive pressure depth anomaly in excess of 12 hPa in the 340-355 K layer at D0 (Fig. 5.6d) in the central North Pacific[3]. Considered independently, 35 of the 36 cases (97%) meet this criteria for at least one of the points, implying that the presence of both of these anomalies is not necessary for a poleward shift, and the presence of either almost always allows a poleward shifted jet.

5.4 Composite analyses of equatorward shifted jets

Composite analyses based upon the 45 equatorward shifted jet cases (negative TE-EOF 2) reveal a muddled composite mean of pressure depth anomalies in the 315-330 K isentropic layer. Few anomalies are present at D-15d (Fig. 5.7a) before a small positive pressure depth anomaly begins forming south of the Aleutian Islands at D-10d (Fig. 5.7b). This positive pressure depth anomaly becomes more intense by D-5d (Fig. 5.7c), at which point other anomalies also begin to come into focus. Two small negative pressure depth

---

[3] The times and locations for the frequency analysis are both chosen to correspond with maximum magnitude of each anomaly – at D-5d near 37˚N 162˚W in the 315-330 K layer and at D0 near 28˚N 105˚E in the 340-355 K layer.

anomalies develop along 30°N between 180° and 130°W, south of the positive pressure depth anomaly at D-5d. The pressure depth gradient between the two supports a decreased geostrophic wind shear and contributes to reducing the 250 hPa zonal wind along and north of the climatological jet axis (roughly 35°N). This negative 250 hPa zonal wind anomaly becomes more pronounced by D0 (Fig. 5.7d) as do the negative pressure depth anomalies equatorward of 35°N. South of these negative pressure depth anomalies, a small area of enhanced westerly zonal winds is evident along 20°N at D-5d and especially at D0. However, the weak pressure depth gradient on the equatorward flank of the negative pressure depth anomaly appears to be too weak to support the 250 hPa zonal wind anomaly, suggesting additional support (in the form of a more intense pressure depth gradient) may lie in the 340-355 K isentropic layer. By D0, this enhancement of the zonal wind extends northeastward over North America ahead of an additional negative pressure depth anomaly along the western coast of the continent, further strengthening the flow from the subtropics to the mid-latitudes over the United States at this time.

By D+5d (Fig. 5.7e), both the positive and negative pressure depth anomalies over the Pacific have begun to decay, but a smaller pressure depth anomaly over the eastern United States that developed around D0 has become more expansive and spread westward by D+5d. While the Pacific pressure depth anomalies are nearly gone by D+10d (Fig. 5.7f), as are the positive zonal wind anomalies over the subtropical Pacific, the positive pressure depth anomaly over North America continues to intensify with anomalies exceeding 36 hPa at D+10d.

It is worth noting that there do not appear to be any meaningful upstream precursors in any of the equatorward shifted composites that precede D0, implying any such signals are not traceable in the composites of pressure depth. Analysis on a case-by-case basis may provide additional insight, however it is possible that the negative phase of this mode of jet variability does not have systematic and identifiable mid-latitude precursors.

Composite analyses of pressure depth anomalies in the 340-355 K isentropic layer reveal more coherent anomalies at D-15d (Fig. 5.8a) than the corresponding 315-330 K layer composite analyses do at that time (Fig. 5.7). A broad negative pressure depth anomaly exists over much of southeast Asia and the Pacific west of 150°E at D-15d and D-10d (Fig. 5.8b) before sliding east off the Asian continent by D-5d (Fig. 5.8c). The emergence of a positive pressure depth anomaly finally occurs on D0 (Fig. 5.8d) around Hawaii, but the gradient between it and the negative pressure depth anomaly that has continued progressing east through D0 remains weak. This pressure depth gradient does help support the low latitude portion of the previously mentioned positive 250 hPa zonal wind anomaly along 20°N that eventually extends over North America. These anomalies both fade by D+5d (Fig. 5.7e) and become weak and indistinct by D+10d (Fig. 5.7f).

5.5. Summary and discussion

The evolution of the pressure depth anomalies in composites of jet extension and retraction suggests two complementary conceptual models. First, the composite large-scale pattern associated with jet extension cases is characterized by a large negative pressure depth anomaly in the 315-330 K isentropic layer and a large positive pressure depth anomaly in the 340-355 K layer (Fig. 5.9a). These anomalies evolve separately and become juxtaposed such that they are on the poleward and equatorward side of the climatological jet exit region, respectively, at the time of maximum extension. This juxtaposition allows for the anomalous geostrophic vertical wind shear associated with each pressure depth anomaly to constructively interact in supporting the positive 250 hPa zonal wind anomalies that define a jet extension (Fig. 5.9a). A similar juxtaposition characterizes the large-scale pattern associated with jet retraction cases, but with the positive pressure depth anomalies in the 315-330 K layer on the poleward flank of the climatological jet and the negative pressure depth anomalies in the 340-355 K layer on the equatorward flank of the jet (Fig. 5.9b). This juxtaposition, also across the climatological jet exit region, allows each pressure depth anomaly to support the negative 250 hPa zonal wind anomalies that constitute a jet retraction.

These two flow configurations, while similar but opposite in their construction, also share similarities in the evolution that leads up to D0 in each composite. In both jet extension and retraction cases, the large pressure depth anomaly in the 315-330 K layer on the poleward flank of the jet merges with a smaller pressure depth anomaly that originates over China and travels through the core of the climatological jet (Fig. 5.1c-d and Fig. 5.3b-d). By the time this smaller anomaly reaches the exit region of the jet, it enters a diffluent flow characterized by deformation along a poleward-oriented axis of dilatation (Figs 5.1d and 5.2d for extended jet events; Figs. 5.3d and 5.4d for retracted jet events). This diffluent deformation renders the originally zonally elongated positive (negative) pressure depth anomalies more isotropic poleward of the exit region of the jet stream, resulting in the retraction (extension) of the jet. Additional investigation of these pressure depth anomalies as they progress through the core of the jet could verify whether the evolution in the composite mean is consistent with the evolution of individual cases.

In the jet retraction case, the small positive pressure depth anomaly in the 315-330 K isentropic layer moves through the core of the climatological jet stream between D-10d and D0 (Fig. 5.3b-d) and can be traced back to its origin near the Tibetan Plateau (at D-15d and D-10d; Fig. 5.3a,b). The plateau serves as a potential source of elevated radiational heating that inflates isentropic pressure depths in a manner similar to the latent heat release from deep convection. This stands in contrast to the positive pressure depth anomaly in the 340-355 K isentropic layer that emerges from a similar region at D-5d (Fig. 5.4c) and strengthens through D+5d (Fig. 5.4e), strengthening consistent with the simultaneous presence of OLR anomalies over Indonesia in the composite shown in Chapter 3 (Fig. 3.7b,d,f).

The similar but opposite structure of the pressure depth anomalies associated with each phase of TE-EOF1 (Fig. 5.9) starkly contrasts with the seemingly unrelated nature of the pressure depth anomalies associated with each phase of TE-EOF2. The composite analyses associated with the poleward shift phase present coherent positive pressure depth anomalies in the 340-355 K isentropic layer (Fig. 5.6) that co-evolve with anomalies in the 315-330 K isentropic layer (Fig. 5.5), creating perhaps the most complex composite-mean evolution associated with any of the four phases of jet variability. In contrast, the pressure depth anomalies in the equatorward shift composite are of smaller maximum magnitudes and do not describe a coherent evolution of that shift through the 25 days of time lags (Figs. 5.7, 5.8). The contrasting nature of these composites suggests that the apparent precursors to poleward shifted jets may not have corresponding opposites that drive the equatorward shift mode. In part, this stems from how the inflation of isentropic layers via outflow from deep convection in the poleward shifted jet composite (Fig. 5.6a-c) is a process for which there is no immediately apparent opposite to drive the deflation of isentropic layers in the corresponding equatorward shifted jet composite. It is therefore no surprise that a complementary but opposite storyline does not emerge from a comparison of the composite means for the two phases. It is important to note that the equatorward shifted jet composite does contain a broad but weak negative pressure depth anomaly in the 340-355 K isentropic level over southeast Asia (Fig. 5.8a-c), although the process by which a deflation of the 340-355 K layer occurs at low latitudes (10-30°N) is not immediately clear.

The unusual co-evolution of the positive pressure depth anomalies in the poleward shift composite (Fig. 5.10) may help outline a framework for more broadly diagnosing cases of tropical-extratropical interaction and potentially quantifying the resultant impact on mid-latitudes. The presence of anomalous OLR over much of the maritime continent in the poleward shifted jet composite presented in Chapter 3 (Fig. 3.8a) appears to serve as the source of deep convective outflow that inflates the 340-355 K isentropic layer over southeast Asia near 25°N in the days preceding D0 (Fig. 5.10c, Fig. 5.6a-c; consistent with the March 2012 case study in the previous chapter). At D-5d (Fig. 5.6c), the positive pressure depth anomaly inflated by this convective outflow begins moving eastward off the Asian continent, bringing the enhanced 250 hPa zonal winds supported by the northern pressure depth gradient eastward as well (Fig. 5.10d). However, positive pressure depth anomalies in the 315-330 K layer have moved into a position to support a separate enhancement of the zonal wind in the jet exit region farther east by D-5d (Fig. 5.5c; Fig. 5.10a). This positive pressure depth anomaly in the 315-330 K isentropic layer acts independently of the pressure depth anomalies in the 340-355 K layer to support a positive zonal wind anomaly that characterizes the poleward shift of the jet exit region. Support for this positive 250 hPa zonal wind anomaly transitions quickly from the pressure depth anomaly in the 315-330 K isentropic layer to the gradient on the northern flank of the positive pressure depth anomaly in the 340-355 K isentropic layer by D0 (Fig. 5.6d; Fig. 5.10b). At this time, the pressure depth anomaly in the 315-330 K layer has moved downstream and become more diffuse (Fig. 5.5d). As described in this poleward shifted jet composite, support for synoptic scale features (such as a ridge or anomalous jet) can transition between pressure depth anomalies of mid-latitude and tropical origin (Fig. 5.10). Such events may not occur frequently, but may provide a basis from which broader consideration of the dynamics of tropical-extratropical interactions can proceed. Specific details of how pressure depth anomalies interact across layers would also provide additional insight into the evolution of the leading modes of North Pacific jet variability themselves, as three of the four phases of the two leading modes involve these interactions between the 315-330 K and 340-355 K isentropic layers.

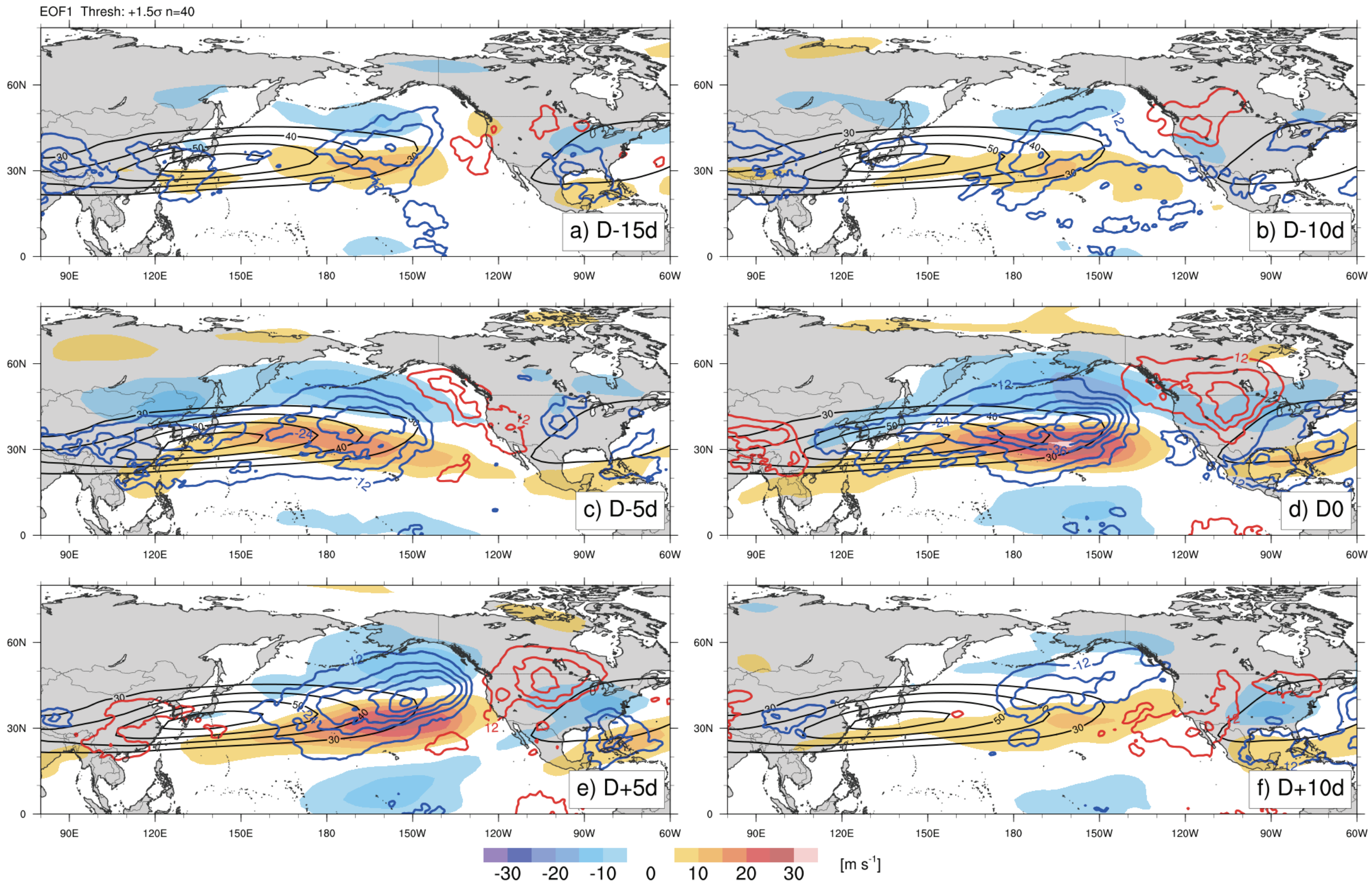

Figure 5.1. Time lagged composite analyses based upon maxima above 1.5 standard deviations in the TE-PC time series associated with TE-EOF 1 from GM16 (for jet extension events). Composite zonal wind anomalies (shaded; m s^{-1}) and isentropic pressure depth anomalies in the 315-330 K layer (contoured; red where positive, blue where negative; every 12 hPa, zero contour excluded) computed at 5 day steps from (a) 15 days prior to the TE-PC maximum through (f) 10 days after.

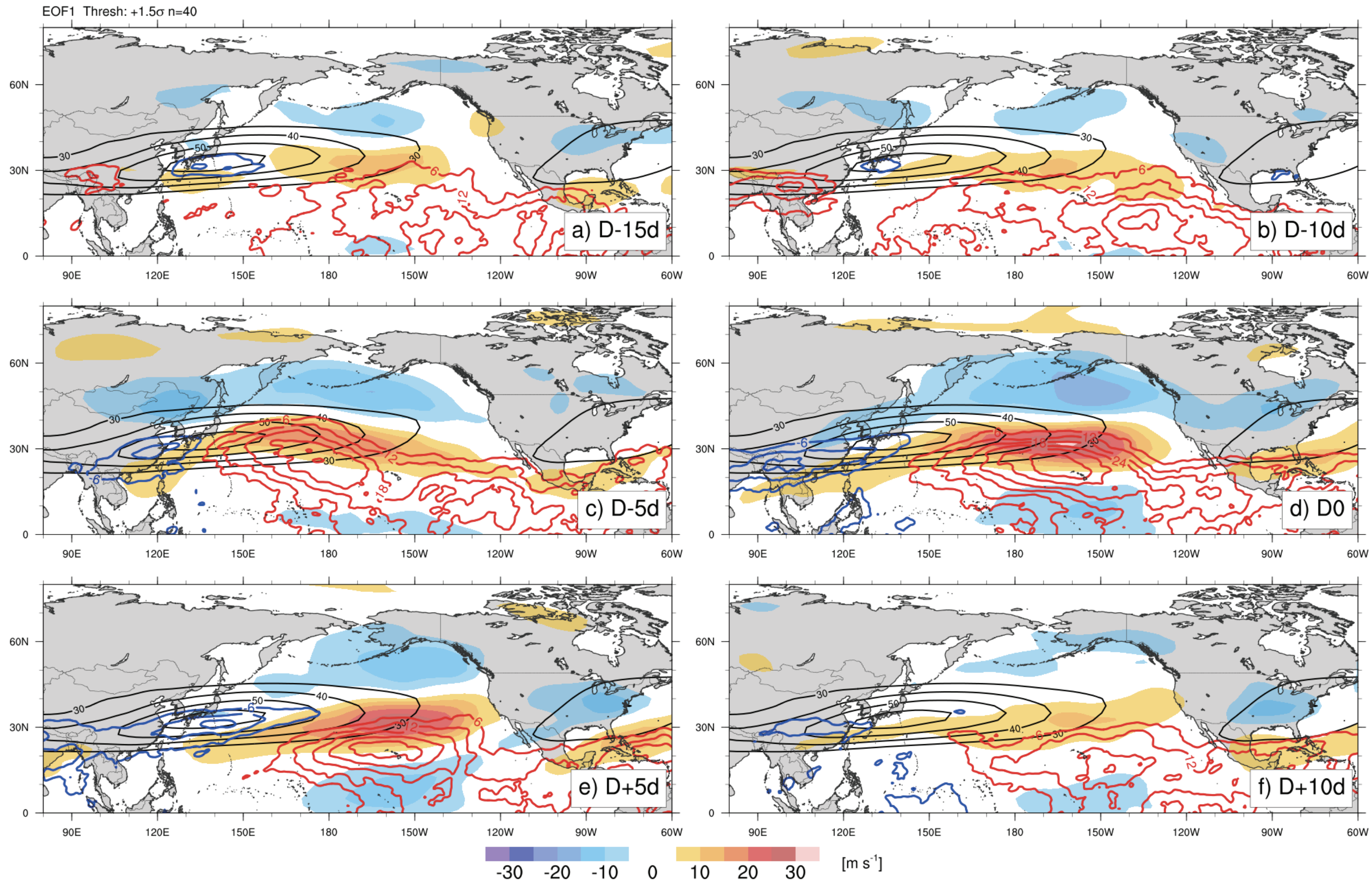

Figure 5.2. As in Fig. 5.1 (for jet extension events), but with isentropic pressure depth anomalies in the 340-355 K layer (contoured every 6 hPa, zero contour excluded).

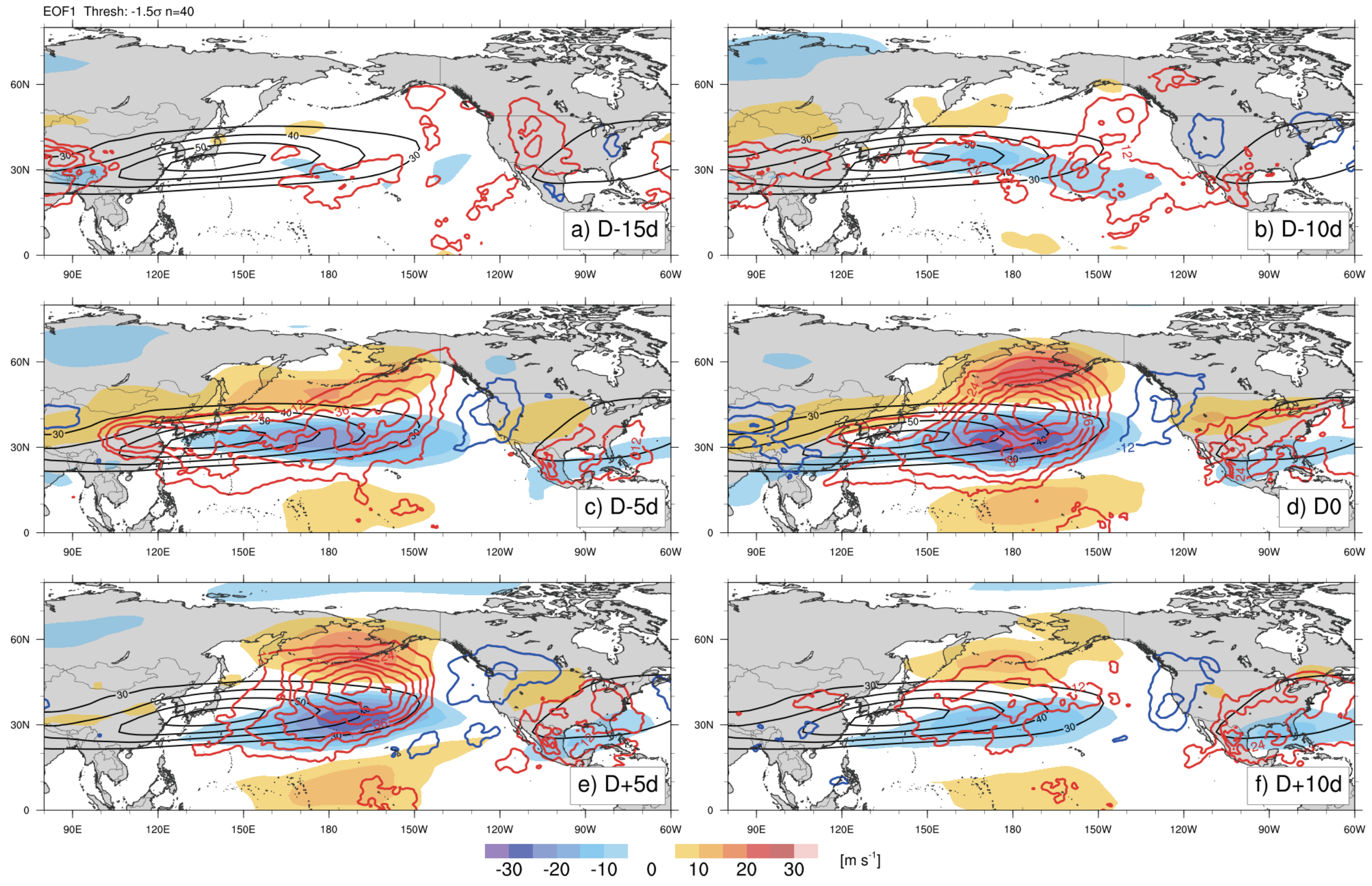

Figure 5.3. As in Fig. 5.1, but with composites constructed around local minimum below -1.5 standard deviations in the TE-PC 1 time series (for jet retraction events).

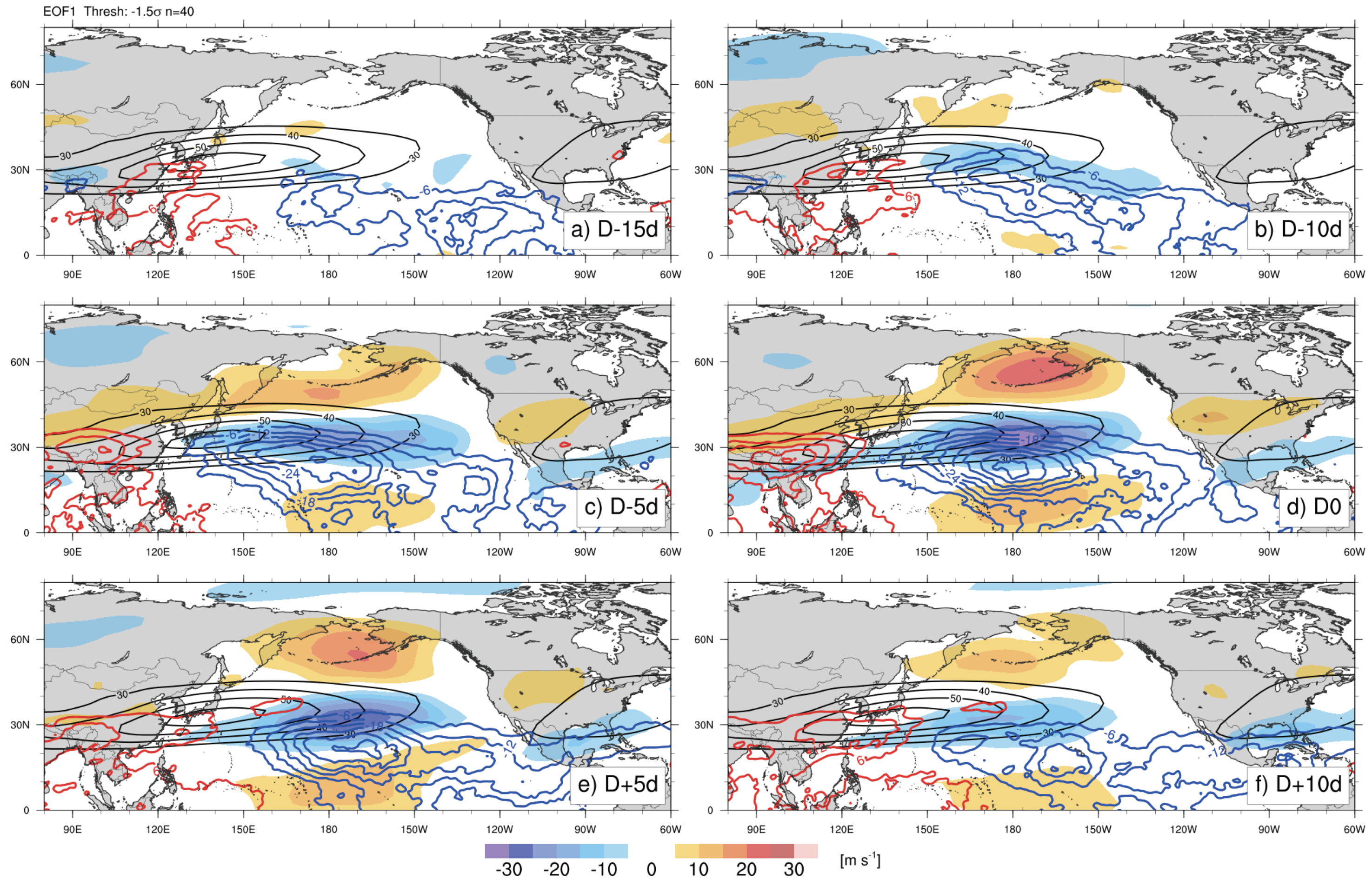

Figure 5.4. As in Fig. 5.2, but with composites constructed around local minimum below -1.5 standard deviations in the TE-PC 1 time series (for jet retraction events).

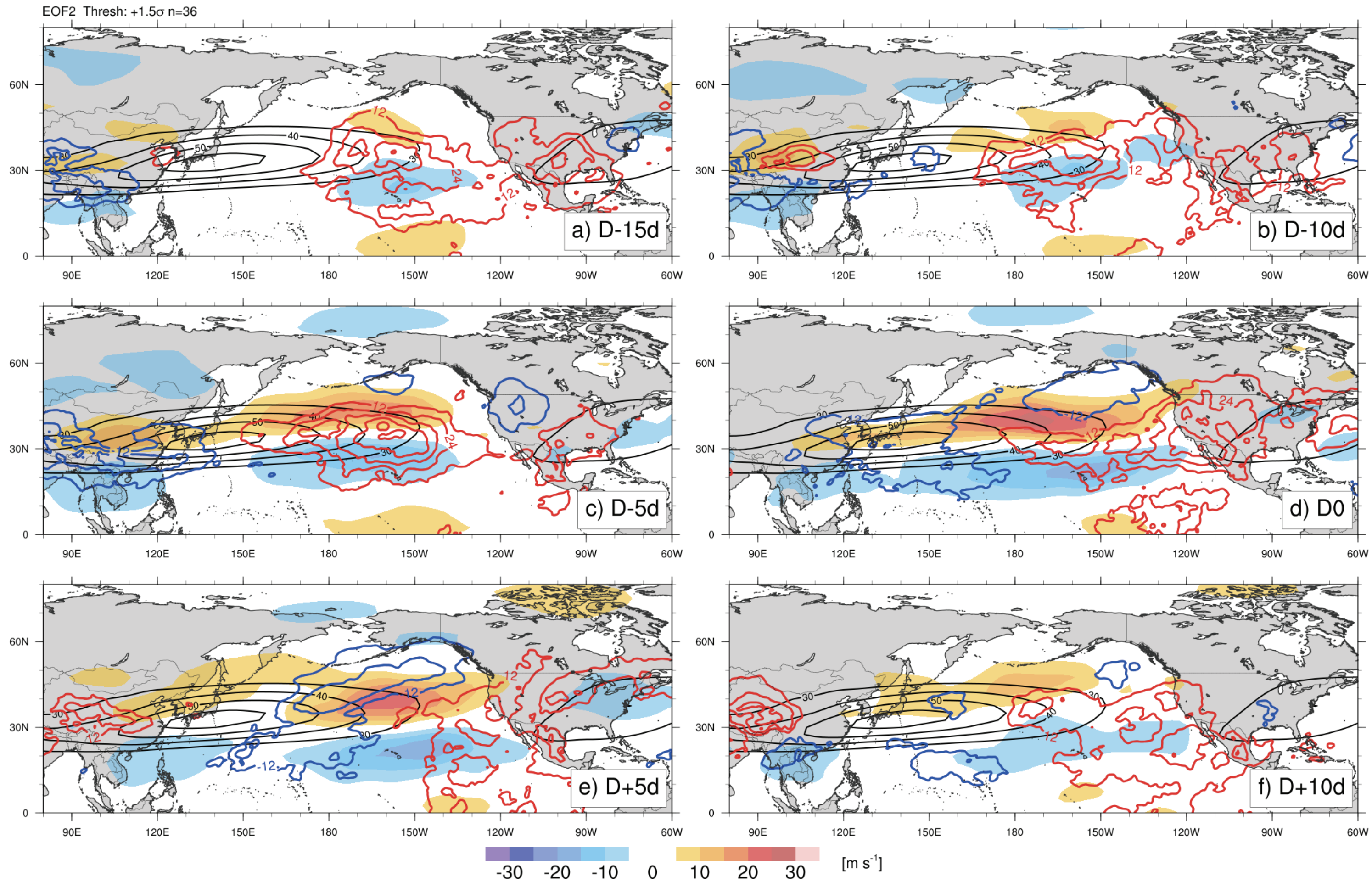

Figure 5.5. As in Fig. 5.1, but with composites constructed around local maximum above 1.5 standard deviations in the TE-PC 2 time series (for poleward shifted jet exit region events).

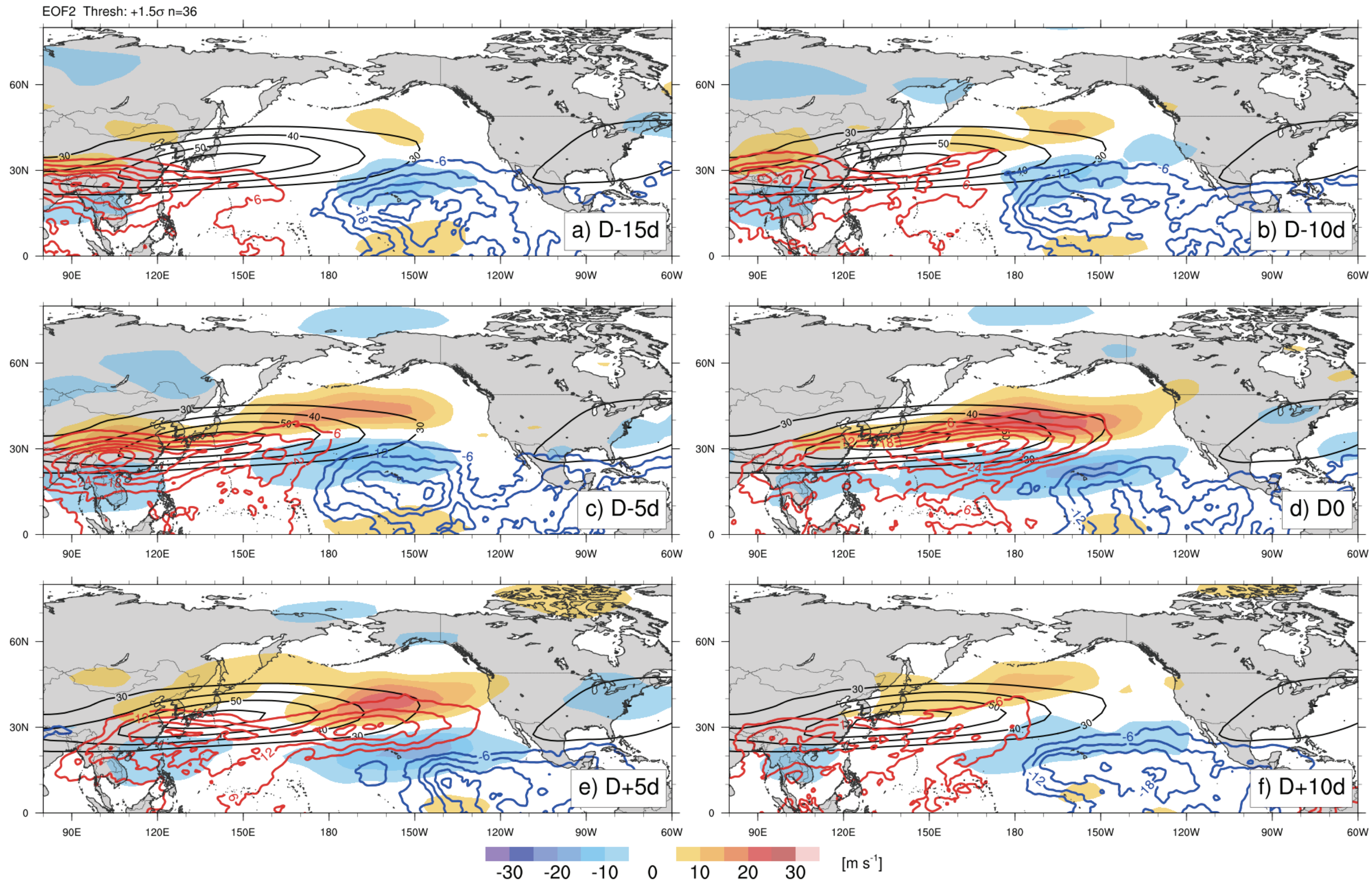

Figure 5.6. As in Fig. 5.2, but with composites constructed around local maximum above 1.5 standard deviations in the TE-PC 2 time series (for poleward shifted jet exit region events).

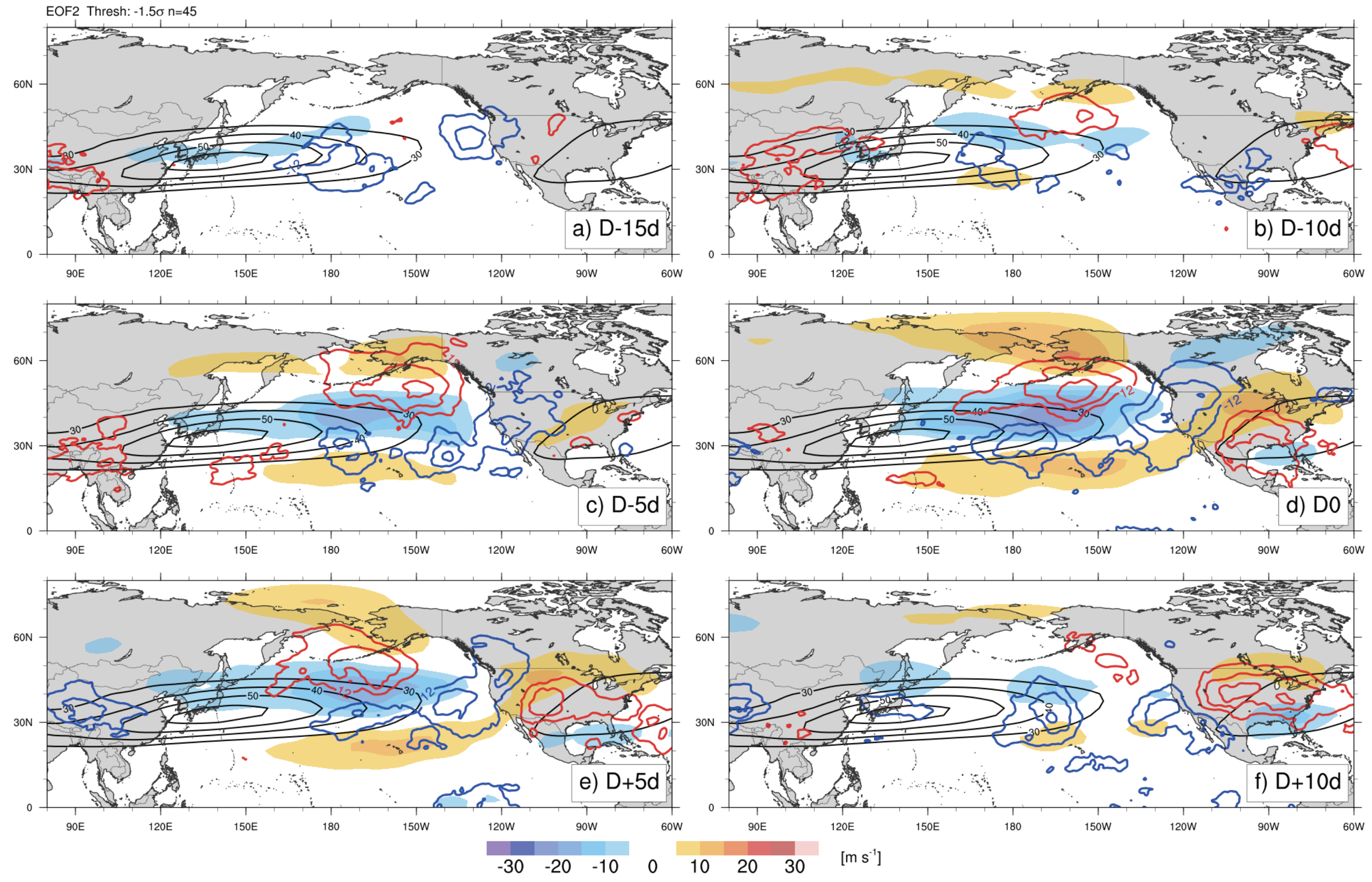

Figure 5.7. As in Fig. 5.1, but with composites constructed around local minimum below -1.5 standard deviations in the TE-PC 2 time series (for equatorward shifted jet exit region events).

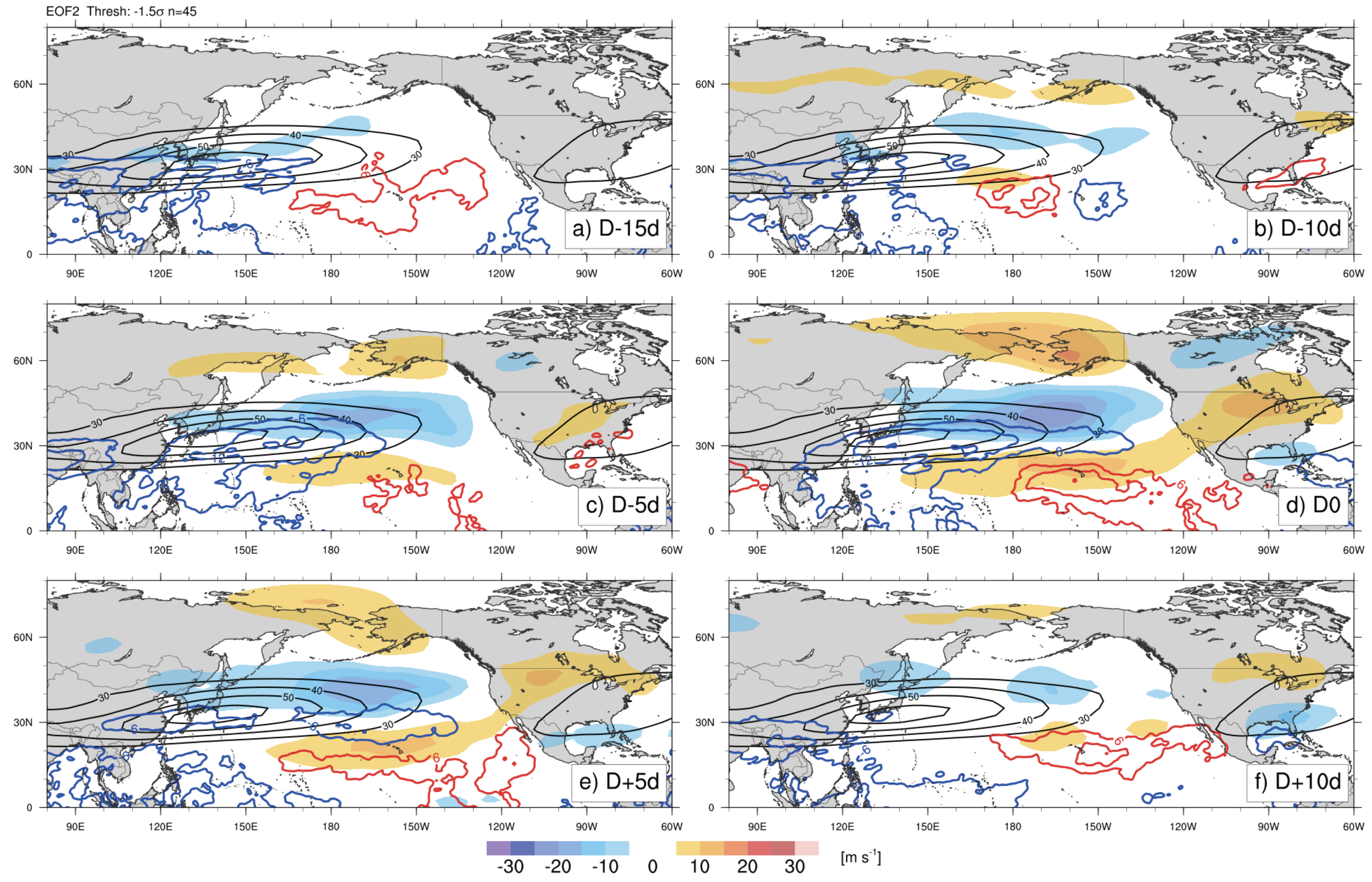

Figure 5.8. As in Fig. 5.2, but with composites constructed around local minimum below -1.5 standard deviations in the TE-PC 2 time series (for equatorward shifted jet exit region events).

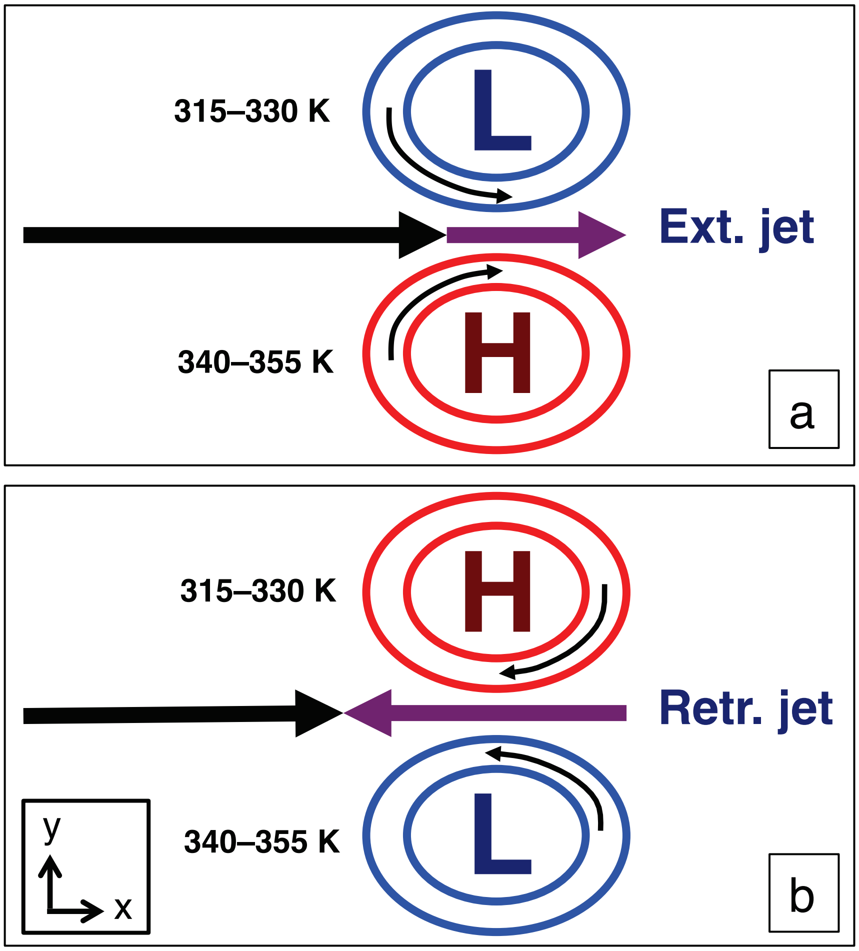

Figure 5.9. Conceptual model of pressure depth anomalies (red and blue contours; in isentropic layers as labeled), the climatological jet stream (thick black arrow), and zonal wind anomalies (thick purple arrow) for (a) jet extension events and (b) jet retraction events.

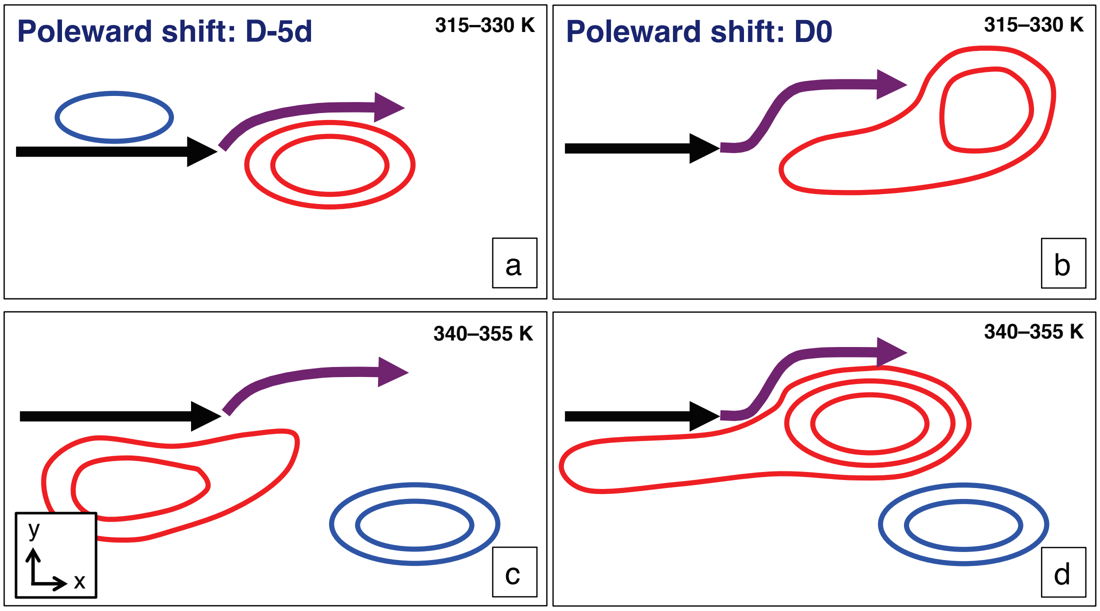

Figure 5.10. Conceptual model of the poleward shifted jet events, with annotations as described for Fig. 5.9. Pressure depth anomalies are in the 315-330 K layer in panels (a) and (b), and in the 340-355 K layer in panels (c) and (d). Panels (a) and (c) represent the position of features at 5 days prior to peak poleward shift (D-5d), while panels (b) and (d) represent the time of maximum poleward shift (D0).

6. Summary, discussion, and future work

Our understanding of jet stream variability over the North Pacific has improved markedly in recent years, with work by Athanasiadis et al. (2010) and Jaffe et al. (2011) leading the way. Given that the leading modes of zonal wind variability over the North Pacific are becoming well-established, some attention can shift toward understanding the events that precede and follow periods where the jet varies notably within one or both of its two leading modes. Jaffe et al. (2011) highlighted the role of synoptic-scale mid-latitude precursors over Asia about a week in advance of an anomalous jet. Little previous work has focused on the downstream mid-latitude impacts associated with the leading modes of jet variability. An interest in examining both upstream precursors and downstream impacts as they related to the leading modes of North Pacific jet variability motivated the work presented in Chapter 3.

An association with deep convection in the tropics had also been noted in the study of jet retraction events by Jaffe et al. (2011). Other previous studies (e.g. Kiladis and Weickmann 1992, 1997, Riemer et al. 2008) explored such an association by examining anomalous tropical convective events and looking for a mean downstream impact in the mid-latitudes. Jaffe et al. (2011) provided results that suggested that convection may, in fact, be a characteristic upstream precursor to at least the jet retraction phase of variability. Additional work was needed to establish exactly *how* the relationships from their jet retraction study as well as relationships from other studies of tropical-extratropical interactions could be borne out physically, motivating the work presented in Chapters 4 and 5.

6.1 Summary

Use of the TE-EOF technique offers a robust means of identifying the preferred evolutions of the tropopause-level jet stream over the North Pacific at synoptic time scales. The leading modes of jet variability identified in Chapter 3 (Figs. 3.1, 3.2) are consistent with the two leading modes of North Pacific jet variability identified via the traditional EOF analyses presented by Athanasiadis et al. (2010) and Jaffe et al. (2011). The two phases of each mode, namely jet extension/retraction for TE-EOF 1 and poleward/equatorward shift of the jet for TE-EOF 2, can be identified using the TE-PCs corresponding to each TE-EOF. Chapter 3 presented a series of composite analyses based on events during which each phase of the first two TE-EOFs exceeded 1.5 standard deviations in magnitude. These composites highlighted the presence of a strong negative (positive) height anomaly in the Gulf of Alaska for jet extension (retraction) events (Figs. 3.3, 3.4). Poleward (equatorward) shifted jets were characterized by a similar distribution of height anomalies though of lesser magnitude and a northward phase shift. Upstream precursor height anomalies over Asia vary among the composites, but are of generally low amplitude. However, anomalous convective activity over the Maritime Continent was also noted throughout the composites of the retraction phase (Fig. 3.7b,d,f) and poleward shift phase (Fig. 3.8a,c,e).

Downstream, the jet extension (Fig. 3.3) and jet retraction (Fig. 3.4) modes are associated with a limited area of significant low-level temperature anomalies over North America between D-5d and D+5d (Fig. 3.3g-i, Fig. 3.4g-i). These anomalies peak near a magnitude of 4°C, while the 850 hPa temperature anomalies peak in excess of +8°C (-8°C) during poleward (equatorward) shifted jet events at both D0 and D+5d (Fig. 3.5h,i, Fig. 3.6h,i). The magnitude of the 850 hPa temperature anomalies associated with TE-EOF 2 events are significantly larger than those associated with the TE-EOF 1 events even though the variability of the jet stream itself explains a lower portion of the total zonal wind variance. It is not immediately apparent why this relationship holds true.

Isentropic pressure depth, introduced in Chapter 4, is a tool that can be used to trace the upper tropospheric mass exhausted from deep convection (Fig. 4.1). The horizontal gradient of isentropic pressure depth is directly related to the vertical shear of the geostrophic wind in a given isentropic layer. Thus, when positive pressure depth anomalies abut a jet streak, they can contribute to the intensification of that jet streak (Fig. 4.4). It is possible to follow those pressure depth anomalies back to the original source of their inflation and thereby attribute that contribution to the jet streak's intensification to a region of aggregate deep convection.

An example of the diagnostic utility of isentropic pressure depth is provided in Chapter 4 via a study of the sequence of tropical and extratropical pressure depth inflation events that led to a period of extreme warmth over eastern North America in March 2012. A key event in that sequence is the rapid cyclogenesis event near Kamchatka on 12 March (event 3 in Fig. 4.17). Prior to this cyclogenesis event, the sequence of events centered around the evolution of the 340-355 K pressure depths, containing mass exhausted from tropical deep convection. After this cyclogenesis event, the sequence of events centered around the evolution of the 315-330 K pressure depths, containing mass exhausted from mid-latitude convection. The rapidly deepening cyclone associated with this transition relates back to the eastward evolution of the jet stream from the Asian coast during 8-12 March in response to the positive pressure depth anomalies associated with a strong MJO event (events 1 and 2 in Fig. 4.17).

These two perspectives are brought together in Chapter 5, where composites of anomalous isentropic pressure depth are constructed based on events during which each phase of the first two TE-EOFs exceeded 1.5 standard deviations in magnitude. In these isentropic pressure depth composites, focus was placed on examining the events preceding and concurrent with the TE window for each phase of the two leading modes of North Pacific jet variability. Jet extension events are dominated by an intense negative pressure depth anomaly in the 315-330 K layer over the Gulf of Alaska and a positive pressure depth anomaly in the 340-355 K layer near 25°N at D0 (Figs. 5.1d, 5.2d, 5.9a). Jet retraction events were characterized by a similar distribution of pressure depth anomalies though of opposite sign in each isentropic layer (Figs. 5.3d, 5.4d, 5.9b). In the 315-330 K layer, the large pressure depth anomaly in each of the jet extension and retraction composites evolves, in part, from an anomaly that originates upstream over Asia and progresses through the climatological jet (Figs. 5.1b-d, 5.3a-d). A similar progression of 315-330 K positive pressure depth anomalies is observed in the poleward shifted jet composite, contributing to a positive pressure depth anomaly in the climatological jet exit region at D-5d (Fig. 5.5c). Although lagging behind the 315-330 K isentropic layer anomalies by about 5 days, the 340-355 K layer contains a similar progression of a large positive pressure depth anomaly from over southeastern Asia at D-10d (Fig. 5.6b) toward the jet exit region by D0 (Fig. 5.6d). Many of these positive pressure depth anomalies appear to originate over Asia, suggesting deep convection or elevated heating as likely causes of these anomalies. In the case of jet retraction and the poleward shift of the jet, the origin of the positive pressure depth anomalies is consistent with the presence of anomalous OLR in the composites presented by Jaffe et al. (2011) and in Chapter 3 (Figs. 3.7b,d,f; 3.8a,c,e).

6.2. Correlations between TE-EOFs and the PNA

The downstream impacts associated with each of the two TE-EOFs share similarities with the Pacific North American (PNA; e.g. Wallace and Gutzler 1981) pattern. These similarities are examined by calculating a correlation for DJF of each year 1980-2010 at lags of -20 to +20 days from a given day in the TE-PC time series. This calculation is performed by taking each day's TE-PC and the PNA value (obtained from the Climate Prediction Center at http://www.cpc.ncep.noaa.gov/products/precip/CWlink/pna/pna.shtml) and correlating across the entirety of a single DJF season. Each season's correlations were averaged to produce the seasonal mean (solid lines in Fig. 6.1) and the ±1 standard deviation value of those seasonal mean correlations (dashed lines).

TE-PC 1 and the PNA correlate best at a zero day lag (Fig. 6.1a) with a peak correlation coefficient of r=0.59, explaining 35% of the variance of the TE-PC. The positive correlation between the two indicates that the positive phase of the PNA and jet extensions tend to occur simultaneously, as do the negative phase of the PNA and jet retractions. This agrees with a visual comparison of the composite height anomalies associated with each phase of TE-EOF 1 (Fig. 3.3b-d and Fig. 3.4b-d) and the canonical PNA pattern (e.g. Wallace and Gutzler 1981, their Fig. 5 and Fig. 7). A similar but weaker correlation is noted between TE-PC 2 and the PNA (Fig. 6.1b), with a peak correlation coefficient of r=0.44 which explains only 19% of the variance of the TE-PC. The downstream responses associated with TE-EOF 2 events (Figs. 3.5, 3.6) do not align with canonical PNA patterns nearly as well as the downstream responses associated with TE-EOF 1 (Figs. 3.3, 3.4), suggesting that the two modes of variability drive substantially different downstream responses.

Correlations with the PNA can also be examined for the traditional PC and a 10-day smoothed PC as each was presented in Chapter 3. The traditional EOF, on average, has a lower correlation with the PNA compared to the TE-EOF at all leads and lags for both EOF 1 (Fig. 6.1a; peak r=0.54, 29% variance explained) and EOF 2 (Fig. 6.1b; peak r=0.42, 18% variance explained). The smoothed EOF, which has a peak correlation coefficient equal to that of the traditional EOF, is similar to the TE-EOF correlation except within ±5 days of lag zero. This suggests that the 10-day temporal coherence of the TE-EOF improves the ability to identify a PNA-like response over the eastern Pacific and North America without smoothing out the correlation within ±5 days of D0.

The factors driving the interannual variability of the strength of the correlation between the TE-EOFs and the PNA is unclear. Some of this interannual variability may stem from large-scale phenomena that remain unaddressed in this analysis, such as ENSO, the Pacific Decadal Oscillation (PDO, Mantua and Hare 2002), or the AO (Thompson and Wallace 1998). An analysis of the synoptic- and planetary-scale differences between such years could provide key information for understanding the variability of the expected downstream impacts from notable TE-EOF 1 or 2 events in any given season.

6.3. Discussion of isentropic pressure depths

6.3.1. The transition from tropically- to extratropically-driven flow

In the case study of the events preceding the March 2012 warmth, the co-evolution of the east Asian jet stream with the support of a tropically-inflated positive pressure depth anomaly (Figs. 4.9c,d, 4.11b; events 2 and 3 in Fig. 4.17; Sections 4.5.2, 6.1) is comparable to the composite means presented for poleward-shifted jet events (Figs 3.5, 5.5, 5.6). In that composite, a region of positive pressure depth anomalies in the 340-355 K isentropic layer is already building over southeast Asia prior to D-15d (Fig. 5.6a), an anomaly likely supported by the anomalous composite negative OLR that extends back through at least D-5d in poleward shifted jet events (Fig. 3.8a). This positive pressure depth anomaly starts to slide off the Asian coast by D-5d (Fig. 5.6c), enhancing the zonal wind on its poleward flank and establishing a poleward shift of the jet exit region by D0 (Fig. 5.6d). The similarities between March 2012 case and the poleward shifted jet composite are greatest on 12 March, when the 340-355 K isentropic pressure depth anomalies (Fig. 4.11b) are most comparable to the composite 340-355 K pressure depth anomalies at D-5d (Fig. 5.6c). Beyond this time, the pressure depth anomalies associated with the March 2012 case move poleward as the cyclone near Kamchatka rapidly deepens, ending any further similarities with the poleward shifted jet composites.

Such a comparison can be extended to include the evolution of the western North Pacific jet stream prior to and during the ET of a TC (e.g. Jones et al. 2003, Archambault et al. 2013). In these cases, a source of deep convection (such as a TC) in the vicinity of a jet streak may be able to interact with the jet streak via its upper-level outflow. When this does occur, a downstream response is triggered, often in the form of a Rossby wave train (e.g. Simmons and Hoskins 1979, Riemer et al. 2008). This is comparable to the process observed in the March 2012 case, where deep convection (associated with the MJO) is able to interact with the jet stream to produce a downstream response. A notable difference, however, is the distance between the deep convection and the jet stream in these two processes. For a TC, the distance between its center and a jet streak is generally on the order of hundreds of kilometers before an interaction takes place (e.g. Harr et al. 2000, Archambault et al. 2013), while interactions via the inflation of the pressure depth in an isentropic layer can occur over thousands of kilometers. The persistence of isentropic pressure depth anomalies provides a means to diagnose the prolonged nature of some tropical-extratropical interactions.

6.3.2. Sources of positive pressure depth anomalies over the mid-latitudes of Asia

A number of the composite analyses in Chapter 5 contain pressure depth anomalies that originate in or near the entrance region of the climatological North Pacific jet stream, which includes much of China and the Tibetan Plateau. When positive, these isentropic pressure depth anomalies likely represent features related to elevated heating near the Tibetan Plateau (e.g. Ye and Wu 1998). In particular, the composite of 340-355 K pressure depths in jet extension cases (Fig. 5.2a-b) as well as the composite of 315-330 K pressure depths in jet retraction cases (Fig. 5.4a-c) and poleward shift cases (Fig. 5.5 b-c) show pressure depth anomalies centered over or intensifying downstream of the Tibetan Plateau.

A study by Christenson (2013) discusses the role that mesoscale convective systems (MCSs) play in producing elevated regions of “high θ_e, low PV outflow” over southeast Asia, specifically Vietnam. In his case from April 2011, the outflow is characterized by large isentropic pressure depths in the 330-340 K layer (his Fig. 5.6b) and traces this region of high θ_e, low PV air on the anticyclonic shear side of a subtropical jet streak as it moves across the North Pacific over a period of a week. Christenson’s description of the progression of the area of large pressure depths along and/or through the climatological jet core is similar to the progression of a positive 315-330 K pressure depth anomaly in jet retraction cases between D-10d and D0 (Fig. 5.3b-d).

To underscore the perspective gained by using the isentropic pressure depth composites in Chapter 5 to diagnose upstream precursors, note that the evolution of some isentropic pressure depth anomalies described in this section are not well represented in the corresponding composite analyses in Chapter 3. For example, in the poleward shifted jet composite, the large accumulation of positive 340-355 K pressure depth anomalies over southeast Asia is represented by a small yet statistically significant positive 250 hPa height anomaly. This composite height anomaly does not move appreciably throughout the 20-day composite period (Fig. 3.5a-e), while the composite positive pressure depth anomaly in the same region at D-10d propagates eastward to support the poleward shift of the zonal wind in the climatological jet exit region at D0 and D+5d(Fig. 5.6b-f).

6.4. Potential forecast applications of downstream impacts of TE-EOF modes

Understanding the typical downstream impacts associated with each of the two TE-EOFs may have predictive use. A study focusing on such power may use a combination of gridded analyses and forecast data from numerical weather prediction (NWP) models to develop an analog-style forecast tool. Real time calculations of the TE-PC yield a TE-PC value from which historic dates with similar TE-PC values can be used to create composite analysis, or analog forecast. That analog forecast may provide insight into potential downstream impacts for the current event. It is not clear what skill current NWP has in predicting the downstream impacts associated with high-amplitude TE-EOF 1 and 2 events, but the predictive skill associated with NWP beyond the 7-10 day range is widely considered to be poor at the present time. Investigation into the utility of this type of analog forecasting at leads beyond 7 days may allow for an improved anticipation of high-impact weather over North America.

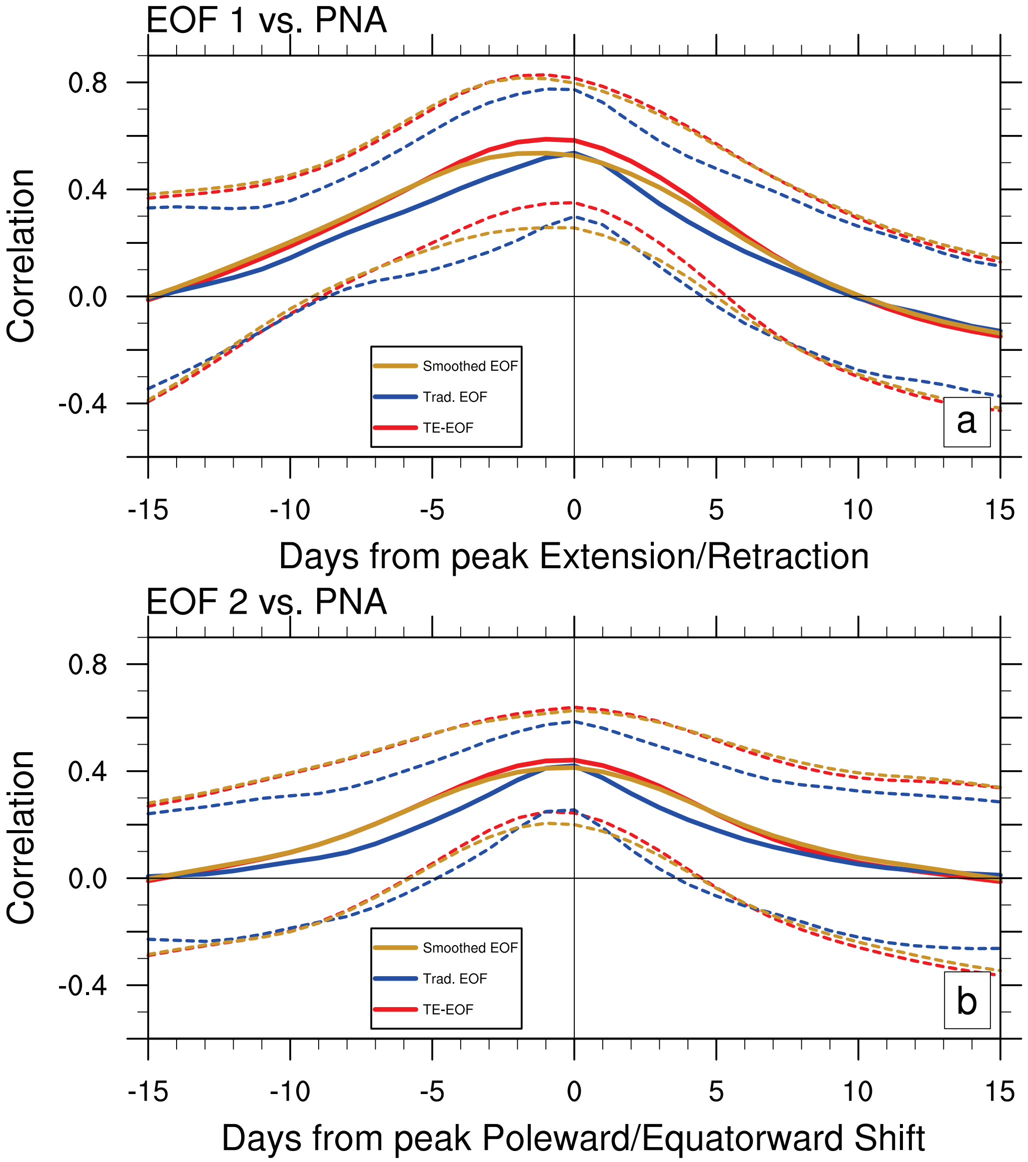

Figure 6.1. Daily time-lagged correlation between the PNA and (a) TE-PC 1, PC 1, and a 10-day smoothed PC 1. (b) As in (a) for the second leading modes of each EOF analysis. The bold middle line represents the mean of the correlation calculated for each season 1980-2010. Dashed lines above and below the bold line represent the ±1 standard deviation of the seasonal correlations. Lines colored per the legend.

7. References

Archambault, H. M., L. F. Bosart, D. Keyser, and J. M. Cordeira, 2013: A climatological analysis of the extratropical flow response to recurving western North Pacific tropical cyclones. *Mon. Wea. Rev.*, **141**, 2325–2346, doi:10.1175/ MWR-D-12-00257.1.

__________, D. Keyser, L. F. Bosart, C. A. Davis, and J. M. Cordeira, 2015: A composite perspective of the extratropical flow response to recurving western North Pacific tropical cyclones. *Mon. Wea. Rev.*, **143**, 1122–1141, doi:10.1175/MWR-D-14-00270.1.

Athanasiadis, P. J., J. M. Wallace, and J. J. Wettstein, 2010: Patterns of wintertime jet stream variability and their relation to the storm tracks. *J. Atmos. Sci.*, **67**, 1361–1381, doi:10.1175/ 2009JAS3270.1.

Chang, C. P., 1970: Westward propagating cloud patterns in the tropical Pacific as seen from time composite satellite photographs. *J. Atmos. Sci.*, **27**, 133–138.

__________, and K. M. W. Lau, 1980: Northeasterly Cold Surges and Near-Equatorial Disturbances over the Winter MONEX Area During December 1974. Part II: Planetary-Scale Aspects. *Mon. Wea. Rev.*, **108**, 298–312. doi: http://dx.doi.org/10.1175/1520-0493(1980)108<0298:NCSANE>2.0.CO;2

Christenson, C. E., 2013: A synoptic climatology of Northern Hemisphere jet superposition events. M.S. Thesis, Atmospheric and Oceanic Sciences, University of Wisconsin-Madison, 62pp.

Chu, P., A. J. Nash, and F. Porter, 1993: Diagnostic Studies of Two Contrasting Rainfall Episodes in Hawaii: Dry 1981 and Wet 1982. *J. Climate*, **6**, 1457–1462. doi: http://dx.doi.org/10.1175/1520-0442(1993)006<1457:DSOTCR>2.0.CO;2

Dickson, R. R., and J. Namias, 1976: North american influences on the circulation and climate of the North Atlantic sector. *Mon. Wea. Rev.*, **104**, 1255–1265. doi: http://dx.doi.org/10.1175/1520-0493(1976)104<1255:NAIOTC>2.0.CO;2

Dole, M. H., and Coauthors, 2014: The making of an extreme event: Putting the pieces together. *Bull. Amer. Meteor. Soc.*, **65**, 427-440, doi: 10.1175/BAMS-D-12-00069.1.

Eichelberger, S. J., and D. L. Hartmann, 2007: Zonal Jet Structure and the Leading Mode of Variability. *J. Climate*, **20**, 5149–5163. doi: http://dx.doi.org/10.1175/JCLI4279.1

Gill, A. E., 1980: Some simple solutions for heat-induced tropical circulation. *Quart. J. Roy. Meteor. Soc.*, **106**, 447–462.

Grams, C. M., and Coauthors, 2011: The key role of diabatic processes in modifying the upper-tropospheric wave guide: A North Atlantic case study. *Quart. J. Roy. Meteor. Soc.*, **137**, 2174–2193.

__________, S. C. Jones, C. A. Davis, P. A. Harr, and M. Weissmann, 2013: The impact of Typhoon Jangmi (2008) on the midlatitude flow. Part I: Upper-level ridge building and modification of the jet. *Quart. J. Roy. Meteor. Soc.*, **139**, 2146–2164. doi:10.1002/qj.2091

Griffin, K. S., and J. E. Martin, 2016: Synoptic features associated with temporally coherent modes of variability of the north Pacific jet stream *J. Climate*, in revision.

Gruber, A., 1974: The wavenumber-frequency spectra of satellite-measured brightness in the Tropics. *J. Atmos. Sci.*, **31**, 1675–1680.

Handlos, Z. J., and J. E. Martin, 2016: Composite analysis of large-scale environments conducive to west Pacific polar/subtropical jet superposition *J. Climate*, in revision.

Hannachi, A. 2004: A Primer for EOF Analysis of Climate Data. Accessed 10 August 2015. [Available online at http://www.met.rdg.ac.uk/~han/Monitor/eofprimer.pdf.]

Harr, P. A., R. L. Elsberry, and T. F. Hogan, 2000: Extratropical transition of tropical cyclones over the western North Pacific. Part II: The impact of midlatitude circulation characteristics. *Mon. Wea. Rev.*, **128,** 2634–2653.

Higgins, R. W., J-K. E. Schemm, W. Shi, and A. Leetmaa, 2000: Extreme Precipitation Events in the Western United States Related to Tropical Forcing. *J. Climate*, **13**, 793–820. doi: http://dx.doi.org/10.1175/1520-0442(2000)013<0793:EPEITW>2.0.CO;2

Horel, J. D., and J. M. Wallace, 1981: Planetary-scale atmospheric phenomena associated with the Southern Oscillation. *Mon. Wea. Rev.*, **109**, 813–829, doi:10.1175/1520-0493(1981)109,0813:PSAPAW.2.0.CO;2.

Hoskins, B. J., and D. J. Karoly, 1981: The steady linear response of a spherical atmosphere to thermal and orographic forcing. *J. Atmos. Sci.*, **38**, 1179–1196.

Jaffe, S. C., J. E. Martin, D. J. Vimont, and D. J. Lorenz, 2011: A Synoptic Climatology of Episodic, Subseasonal Retractions of the Pacific Jet. *J. Climate*, **24**, 2846–2860. doi: http://dx.doi.org/10.1175/2010JCLI3995.1

Jayawardena, I. M. S., Y.-L. Chen, A. J. Nash, and K. Kodama, 2012: A Comparison of Three Prolonged Periods of Heavy Rainfall over the Hawaiian Islands.*J. Appl. Meteor. Climatol.* **51**, 722–744.

Jones, S. C., and co-authors, 2003: The extratropical transition of tropical cyclones: forecast challenges, current understanding, and future directions. *Wea. Forecasting*, **18**, 1052–1092. doi: http://dx.doi.org/10.1175/1520-0434(2003)018<1052:TETOTC>2.0.CO;2

Kalnay, E., and Coauthors, 1996: The NCEP/NCAR 40-Year Reanalysis Project. *Bull. Amer. Meteor. Soc.*, **77**, 437–471.

Kiladis, G. N., and K. M. Weickmann, 1992: Circulation anomalies associated with tropical convection during northern winter. *Mon. Wea. Rev.*, **120**, 1900–1923. doi: http://dx.doi.org/10.1175/1520-0493(1992)120<1900:CAAWTC>2.0.CO;2

______, and _______, 1997: Horizontal structure and seasonality of large-scale circulations associated with submonthly tropical convection. *Mon. Wea. Rev.*, **125**, 1997–2013. doi: http://dx.doi.org/10.1175/1520-0493(1997)125<1997:HSASOL>2.0.CO;2

______, M. C. Wheeler, P. T. Haertel, K. H. Straub, and P. E. Roundy, 2009: Convectively coupled equatorial waves. *Rev. Geophys.*, **47**, RG2003, doi:10.1029/2008RG000266

Koteswaram, P., 1953: An analysis of the high tropospheric wind circulation over India in winter. *Indian J. Meteor. Geophys.*, **4**, 13–21.

Krishnamurti, T. N., 1961: The subtropical jet stream of winter. *J. Meteor.*, **18**, 172–191. doi: http://dx.doi.org/10.1175/1520-0469(1961)018<0172:TSJSOW>2.0.CO;2

Lewis, J. M., 2003: Ooishi's Observation: Viewed in the Context of Jet Stream Discovery. *Bull. Amer. Meteor. Soc.*, **84**, 357–369. doi: http://dx.doi.org/10.1175/BAMS-84-3-357

Liebmann, B., and D. L. Hartmann, 1984: An observational study of tropical–midlatitude interaction on intraseasonal time scales during winter. *J. Atmos. Sci.*, **41**, 3333–3350, doi:10.1175/ 1520-0469(1984)041,3333:AOSOTI.2.0.CO;2.

_________, and C. A. Smith, 1996: Description of a complete (interpolated) outgoing longwave radiation dataset. *Bull. Amer. Meteor. Soc*, **77,** 1275–1277

Loewe, F., and U. Radok, 1950: A meridional aerological cross section in the southwest Pacific. *J. Meteor.*, **7**, 58–65. doi: http://dx.doi.org/10.1175/1520-0469(1950)007<0058:AMACSI>2.0.CO;2

Madden, R. A., and P. R. Julian, 1971: Detection of a 40–50 day oscillation in the zonal wind in the tropical Pacific. *J. Atmos. Sci.*, **28,** 702–708.

_________, and _________, 1972: Description of Global-Scale Circulation Cells in the Tropics with a 40–50 Day Period. *J. Atmos. Sci.*, **29**, 1109–1123. doi: http://dx.doi.org/10.1175/1520-0469(1972)029<1109:DOGSCC>2.0.CO;2

_________, and _________, 1994: Observations of the 40–50-day tropical oscillation. *Mon. Wea. Rev.*, **122**, 814–837.

Magnusdottir, G., and W. H. Shubert, 1990: The generalization of semigeostrophic theory to the β plane. *J. Atmos. Sci.*, **47**, 1714–1720.

Mantua, N. J., S. R. Hare, 2002: Pacific Decadal Oscillation. *J. Oceanogr.*, **58,** 35-44.

Matsuno, T., 1966: Quasi-geostrophic motion in the equatorial area. *J. Meteor. Soc. Japan*, **44**, 25–43.

Mohri, K., 1953: On the fields of wind and temperature over Japan and adjacent waters during winter of 1950–1951. *Tellus*, **5**, 340–358.

_________, 1959: Jet streams and upper fronts in the general circulation and their characteristics over the Far East (Part II). *Geophys. Mag.*, **29**, 333–412.

Moncrieff, M. W., M. A. Shapiro, J. M. Slingo, and F. Molteni, 2007: Collaborative research at the intersection of weather and climate. *WMO Bull.*, **56**, 204–211.

Namias, J., and P. F. Clapp, 1944: Studies of the motion and development of long waves in the westerlies. *J. Meteor.*, **1**, 57–77, doi:10.1175/1520-0469(1944)001,0057:SOTMAD.2.0.CO;2.

_________, and _________, 1949: Confluence theory of the high tropospheric jet stream. *J. Meteor.*, **6**, 330–336. doi: http://dx.doi.org/10.1175/1520-0469(1949)006<0330:CTOTHT>2.0.CO;2

Newton, C. W., 1954: Frontogenesis and frontolysis as a three-dimensional process. *J. Meteor.*, **11**, 449–461, doi:10.1175/1520-0469(1954)011,0449:FAFAAT.2.0.CO;2.

Orlanski, I., and J. P. Sheldon, 1993: A case of downstream baroclinic development over western North America. *Mon. Wea. Rev.,***121,** 2929–2950.

Otkin, J. A., and J. E. Martin, 2004: The Large-Scale Modulation of Subtropical Cyclogenesis in the Central and Eastern Pacific Ocean. *Mon. Wea. Rev.*, **132**, 1813–1828. doi: http://dx.doi.org/10.1175/1520-0493(2004)132<1813:TLMOSC>2.0.CO;2

Palmén, E., 1951: The role of atmospheric disturbances in the general circulation. *Quart. J. Royal Meteor. Soc.*, **77**, 337–354. doi: http://dx.doi.org/10.1002/qj.49707733302

Reiter, E. R., 1983: Teleconnections with Tropical Precipitation Surges. *J. Atmos. Sci.*, **40**, 1631–1647.

_________ and L. F. Whitney, 1969: Interaction between subtropical and polar-front jet stream. *Mon. Wea. Rev*., **97**, 432–438. doi: http://dx.doi.org/10.1175/1520-0493(1969)097<0432:IBSAPJ>2.3.CO;2

Rex, D. F., 1950: Blocking action in the middle troposphere and its effect upon regional climate. I. An aerological study of blocking action. *Tellus*, **2,** 196–211.

Riemer, M., S. C. Jones, and C. A. Davis, 2008: The impact of extratropical transition on the downstream flow: An idealized modeling study with a straight jet. *Quart. J. Roy. Meteor. Soc.*, **134**, 69–91, doi: http://dx.doi.org/10.1002/qj.189.

_________, and _________, 2010: The downstream impact of tropical cyclones on a developing baroclinic wave in idealized scenarios of extratropical transition. *Quart. J. Roy. Meteor. Soc.*, **136**, 617–637.

Rodwell, M. J., and B. J. Hoskins, 2001: Subtropical anticyclones and summer monsoons. *J. Climate*, **14,** 3192–3211.

Roundy, P. E., 2015: On the Interpretation of EOF Analysis of ENSO, Atmospheric Kelvin Waves, and the MJO. *J. Climate*, **28**, 1148–1165. doi: http://dx.doi.org/10.1175/JCLI-D-14-00398.1

_________, and C. J. Schreck, 2009: A combined wave-number–frequency and time-extended EOF approach for tracking the progress of modes of large-scale organized tropical convection. *Quart. J. Roy. Meteor. Soc.*, **135**, 161–173, doi:10.1002/qj.356.

Saha, S., and Coauthors, 2010: The NCEP Climate Forecast System Reanalysis. *Bull. Amer. Meteor. Soc.*, **91**, 1015–1057.

Schubert, S. D., and C. Park, 1991: Low-Frequency Intraseasonal Tropical-Extratropical Interactions. *J. Atmos. Sci.*, **48**, 629–650. doi: http://dx.doi.org/10.1175/1520-0469(1991)048<0629:LFITEI>2.0.CO;2

Simmons, A. J., and B. J. Hoskins, 1979: Downstream and upstream development of unstable baroclinic waves. *J. Atmos. Sci.*, **36,** 1239–1254.

Thompson, D. W. J., and J. M. Wallace, 1998: The Arctic Oscillation signature in the wintertime geopotential height and temperature fields. *Geophys. Res. Lett.,* **25,** 1297–1300.

Thorncroft, C. D., and S. C. Jones, 2000: The extratropical transitions of Hurricanes Felix and Iris in 1995. *Mon. Wea. Rev.*, **128,** 947–972.

University of Chicago, 1947: On the General Circulation of the Atmosphere in the Middle Atmosphere. *Bull. Amer. Meteor. Soc.* **28,** 255–280.

Wallace, J. M., and D. S. Gutzler, 1981: Teleconnections in the geopotential height field during the Northern Hemisphere winter. *Mon. Wea. Rev.*, **109**, 784–812. doi: http://dx.doi.org/10.1175/1520-0493(1981)109<0784:TITGHF>2.0.CO;2

Weare, B. C., and J. S. Nasstrom, 1982: Examples of extended empirical orthogonal function analyses. *Mon. Wea. Rev.*, **110**, 481–485.

Weickmann, K. M., 1983: Intraseasonal circulation and outgoing longwave radiation modes during Northern Hemisphere winter. *Mon. Wea. Rev.*, **111**, 1838–1858.

Wheeler, M., and H. H. Hendon, 2004: An all-season real-time multivariate MJO index: Development of an index for monitoring and prediction. *Mon. Wea. Rev.*, **132,** 1917–1932.

Wilks, D. S., 2011: *Statistical Methods in the Atmospheric Sciences*. Academic Press, 676 pp.

Wunsch, C., and A. E. Gill, 1976: Observations of equatorially trapped waves in Pacific sea level variations. *Deep-Sea Res*., **23**, 371–390.

Yanai, M., and M. Murakami, 1970a: A further study of tropical wave disturbances of the use of spectrum analysis. *J. Meteor. Soc. Japan*, **48,** 185–197.

__________, and __________,1970b: Spectrum analysis of symmetric and antisymmetric equatorial waves. *J. Meteor. Soc. Japan*, **48**, 331–347.

Ye, D. Z., and G. X. Wu, 1998: The role of the heat source of the Tibetan Plateau in the general circulation. *Meteor. Atmos. Phys.*, **67,** 181–198.

Yeh, T. C., 1950: The circulation of high troposphere over China in winter of 1945–46. *Tellus*, **2,** 173–183.

Zhang, C., 1993: Large-scale variability of atmospheric deep convection in relation to sea surface temperature in the tropics. *J. Climate,* **6,** 1898–1913.

__________, 2005: Madden-Julian Oscillation. *Rev. Geophys.*, **43**. RG2003, doi:10.1029/2004RG000158